NOISE REDUCTION AND CLUTTER SUPPRESSION IN MICROWAVE IMAGING AND DETECTION

NOISE REDUCTION AND CLUTTER SUPPRESSION IN MICROWAVE IMAGING AND DETECTION

By

JUSTIN JOHN MCCOMBE, B.ENG.

A Thesis Submitted to the School of Graduate Studies in Partial Fulfillment of the Requirements for the Degree Master of Applied Science

McMaster University

MASTER OF APPLIED SCIENCE (2014) McMaster University
(Electrical and Computer Engineering) Hamilton, Ontario

TITLE: **Noise Reduction and Clutter Suppression in Microwave Imaging and Detection**

AUTHOR: Justin John M^{c}Combe
B.Eng. (Electrical Engineering)
McMaster University, Hamilton, Canada

SUPERVISOR: Natalia K. Nikolova, Professor,
Department of Electrical and Computer Engineering
McMaster University
Ph.D. (University of Electro-Communication)
Fellow, IEEE
P.Eng. (Ontario)
Canada Research Chair in High Frequency Electromagnetics

NUMBER OF PAGES: CLXI, 161

ABSTRACT

Commercial concealed weapon detection systems are large and expensive and are not suitable to be used as a portable system. Currently, new methods of concealed weapon detection are being developed to build small and compact systems. One such method is based upon the natural resonances of objects; however, no such system has made it to the market due to the low quality of the signals used in the detection algorithms.

In this thesis, a prototype concealed weapon detection system is developed and tested for operation in a cluttered environment. This system utilizes the late-time portion of a radar return to extract the resonance information of an unknown target. After proper signal processing and clutter suppression, the signals are classified to determine if the object is a threat. Multiple measurements with frequency-sweep and time-domain systems are used to verify the algorithm.

Microwave tissue imaging techniques aim to reconstruct the internal dielectric distribution of the tissue and rely on the dielectric contrast between healthy and malignant tissues. This contrast has been shown to be weak, and therefore, the signals are easily susceptible to noise.

This thesis proposes and validates a method for signal-to-noise ratio analysis of complex *S*-parameter data sets that are used for microwave imaging. A study of de-noising and artifact reduction techniques for microwave holographic imaging is also presented.

ACKNOWLEDGEMENTS

First and foremost, I would like to express my sincere gratitude to my supervisor, Dr. Natalia K. Nikolova, for her guidance, encouragement and patience throughout my work. I am grateful for her continued support as both a mentor and friend who has contributed greatly to my personal and professional growth. It has been a great honour and pleasure to work with her over the course of my M.A.Sc. study.

I also want to express my gratitude to Tyler Ackland who has always been eager to offer advice and assistance with the construction of the microwave imaging and concealed weapon detection systems. My sincere thanks also go to Dr. Mohamed Bakr, Dr. James Reilly, and Dr. Tim Davidson from whose lectures I benefited greatly.

I would like to acknowledge the contributions of Dr. Reza K. Amineh and Dr. Maryam Ravan who developed the holographic imaging approach that is used in Chapter 6. Without the assistance of Dr. Amineh, I would never have been able to develop techniques and methodologies to improve the quality of the images produced by the holographic technique. I would also like to acknowledge the contributions of Mihail Georgiev who started work on the concealed weapon detection project and performed the initial measurements and signal processing that steered the project in the right direction. Without these developments the project would never have developed to its current state.

I also want to thank all the colleagues and friends from the Computational Electromagnetics Laboratory for all the interesting discussions, constructive comments, and for making our laboratory a pleasant place to work. My many thanks to all of the members from our research group including: Reza Amineh, Sheng Tu, Yifan Zhang, Kaveh Moussakhani, Sadegh Dadash, Denys Shumakov, Alex Beaverstone, and Jeff Thompson.

I would like to thank my family for their love and encouragement in this endeavor. Last, but not least, I would like to thank my dearest Dori for her endless encouragement and support. Without her, I would never have made it this far.

CONTENTS

LIST OF FIGURES

LIST OF TABLES

CHAPTER 1

INTRODUCTION

1.1. BACKGROUND: CONCEALED WEAPON DETECTION

There are three main approaches to the detection of concealed weapons using radar technology: 1) identification of resonant signature of weapons, 2) active microwave and millimeter-wave imaging, and 3) passive millimeter-wave radiometry. The first approach is a detection approach where a yes/no decision is made by the algorithm. The second two are imaging methods and rely on trained people to determine if an object is a threat or not. There are also many other detection approaches that operate using infrared, acoustic and ultrasonic, and magnetic field distortion technologies. A full review of current detection technologies is described in [1] – [3].

Concealed weapon detection using microwave radars to excite the natural resonances of weapons was first performed by Hunt *et al.* [4][5][6]. Hausner and West [7][8] have also reported a practical system. The system developed by Hunt suffers from low probability of detection (64%) and a high level of false positives(36%). They also recognize that there results are improved when a single individual is used for all measurements. This suggests that the human body has a large impact on the detection capabilities of the system. Hausner and West improved on Hunt's system achieving a probability of detection of 95% and a low level of false positives (<10%). However, the system requires and individual to be compliant and stand facing the system with their arms outstretched. This is a drawback for systems that are covert and can lead to a high throughput. A major

drawback to this resonance approach is in the noise due to the signatures of the person and the environment which can mask the signature of a weapon.

Active imaging systems have gained popularity in airport screening due to their resolution that is bellow $1/10^{th}$ of the size of a typical weapon. These millimeter wave systems also operate in a band where the contrast between the body and a metallic weapon is very high. Such systems were proposed by Sheen *et al.* in [9] – [12]. The drawback to the active imaging systems is the need for compliance as people must assume a specified position. This causes the throughput of the security checkpoint to be fairly low. Additionally, due to the high cost of millimeter wave components, the systems are very expensive. This makes the system impractical for widespread use.

Passive imaging systems respond to the thermal energy emitted by the target to form an image. The principals are similar to those of infrared imaging, however with poorer resolution. The advantage lies in the penetration, where millimeter waves can penetrate through clothing, rain, and fog, infrared wave cannot. Millimeter wave radiometric systems are capable of detecting metallic and non-metallic objects because it senses the temperature difference between the concealed object and the human body. A review of millimeter wave radiometry can be found in [13]. Promising systems have been reported in [14] – [18]. The challenge with such systems lies in the scan time, which is currently approximately one second.

1.2. MOTIVATION: RESONANCE BASED CONCEALED WEAPON DETECTION

Current commercial systems for concealed weapon detection (CWD) face many drawbacks. Portable systems, such as handheld wands, require the operator to be close to the individual and make a possibly erroneous decision. Walkthrough systems, such as metal detectors and full body scanners, require users to funnel through a checkpoint which causes delays. Many detectors also have a high rate of false positive outcomes due to their sensitivity to innocuous objects, such as belts, keys and cell phones. On the other hand, imagers require an operator to view a fairly detailed image which causes privacy concerns among the public.

There is a great need for a compact and portable system that is affordable and can be used without a trained operator. A microwave detection system fulfills these needs because it does not produce an image but simply issues a *threat/non-threat* outcome. A *threat* decision can be used to trigger a protection response such as security personnel intervention, locking a doorway, triggering a sound alarm, taking a photograph of the inspected person, etc. Additionally, a major advantage of such a system is that screening can be performed while the inspected person is moving, e.g., walking through a hallway. This enables high throughput as well as covert screening, if desired.

Such a system is based upon the principles of resonant modes. Every structure has intrinsic resonant modes that depend on its size, shape, and constitutive parameters. In the case of small weapons, many of these resonances

occur at frequencies in the low GHz range. With proper algorithms for determining the resonant modes, detection can be facilitated by comparing the resonant modes of a test subject to a library of resonant modes of known objects. If the test subject has resonant modes that are similar to those of a known weapon, a *threat* outcome is issued.

1.3. CONTRIBUTIONS: CONCEALED WEAPON DETECTION

The author has contributed substantially to the following developments in the area of concealed weapon detection:

1) Developed a method of detecting concealed weapons in a cluttered environment based on late time resonance information. The method includes a novel technique for the suppression of environmental radar clutter and a method for robust target classification.
2) Performed extensive measurements investigating parameter effects in the developed concealed weapon detection algorithm published in [19] and reported in [20][21].
3) Developed prototype radar systems based on laboratory equipment published in [19] and reported in [20][21].

1.4. BACKGROUND: MICROWAVE IMAGING FOR BREAST CANCER DIAGNOSTICS

The work discussed on microwave imaging in this thesis is entirely built off of the microwave holographic imaging approach developed by Amineh *et al.* [22].

A background on microwave imaging techniques for breast cancer is provided by Nikolova in [23].

1.5. Motivation: Microwave Imaging for Breast Cancer Diagnostics

Currently, there is no agreed upon method to assess the signal-to-noise ratio (SNR) of data acquired for microwave imaging. The development of a standard approach to the evaluation of the SNR is of great use to the field in order to compare acquisition hardware, to discriminate between low- and high-quality data sets and to determine the appropriate image processing strategy based on the data quality. Additionally, by measuring the SNR of the system and evaluating the reconstruction algorithm performance based on this SNR, one can determine at which SNR levels a specific reconstruction algorithm can operate well.

A thorough study of microwave holography, as described in [22], is needed to determine the effects of spectral windowing, which is expected to provide means to de-noise the images when the scanning step size is smaller than the size of the object used to measure the system point-spread function. An investigation into the effects of interpolating the measured point spread functions is also considered to determine its effect on artifact suppression. Additionally, data discrimination is performed based on the SNR technique developed here, and its effect on the reconstructed images is studied. These studies give insight into the ways in which artifact reduction and noise reduction may be performed in order to improve the resulting images.

1.6. CONTRIBUTIONS: MICROWAVE IMAGING

The author has contributed substantially to the following developments in the area of microwave imaging:

4) Developed a method of evaluating the SNR of complex-valued *S*-parameter imaging data [24][25].
5) Investigated methods of de-noising and artifact reduction in microwave holography.
6) Contributed to the design and construction of antennas for microwave imaging [22][26].
7) Performed extensive measurements and performed holographic reconstruction that contributed to the journal publications [22]-[29] and the conference publications [30]-[32].

1.7. OUTLINE OF THESIS

This thesis is divided into two parts. Part 1 covers work on concealed weapons detection and spans Chapters 2 through 4. Part 2 covers work on microwave imaging discussed in Chapters 5 and 6.

Chapter 2 describes the theory of concealed weapon detection based upon resonance analysis. It first discusses the method of extracting resonance information, then discusses and provides a solution to the challenges associated with classification in a cluttered environment. Lastly, the classification methods for verifying the functionality of the method are described.

Chapter 3 covers the experimental work on frequency-sweep systems built using vector network analyzers. These initial systems are tested in uncontrolled environments to determine the feasibility of the detection method. Later chapter, an investigation of the effects of operating in an environment different in the from that of the training environment is conducted.

Chapter 4 describes a time domain system developed to provide fast acquisition of the data needed for the detection algorithm. First, the system design is discussed, along with some alteration of the algorithm to accommodate the time-domain data. A method for the separation of the early-time and late-time portions of the radar return is proposed and applied. Also, a method for the de-embedding of the effect of mutual coupling between the Tx and the Rx antenna is also proposed and applied. Finally, results are presented for training and testing in a single environment.

Chapter 5 proposes a method of evaluating the SNR of complex-valued *S*-parameter data that is used in image reconstruction. This chapter compares multiple methods for calculating the SNR and describes a graphical interface that has been developed for fast and simple SNR calculations.

Chapter 6 investigates the effects of noise on microwave holography. First, a method of de-noising the images is described that involves spectral windowing. Second, an investigation into the interpolation of calibration-object data along the range direction is investigated for reduction of artifacts. Finally, an

investigation into the effects of frequency discrimination based on raw data SNR analysis is conducted.

Chapter 7 concludes the thesis with a summary and recommendations for future work. A full bibliography is given at the end of the thesis.

REFERENCES

[1] N. G. Paulter, "Guide to the technologies of concealed weapon imaging and detection," NIJ Guide 602-00, 2001, on line: http://www.ncjrs.gov/pdffiles1/nij/184432.pdf.

[2] H.-M. Chen, S. Lee, R. M. Rao, M. A. Slamani, and P. K. Varshney, "Imaging for concealed weapon detection," *IEEE Signal Processing Mag*., Mar. 2005, pp. 52–61.

[3] A. Agurto, Y. Li, G. Y. Tian, N. Bowring, and S. Lockwood, "A review of concealed weapon detection and research in perspective," *Proc. of the 2007 IEEE Int. Conf. on Networking, Sensing and Control*, Apr. 2007, pp. 443–448.

[4] A. R. Hunt, R. D. Hogg, and W. Foreman, "Concealed weapons detection using electro-magnetic resonances*," SPIE Conference on Enforcement and Security Technologies*, Boston, MA, Nov. 1998, pp. 62–67.

[5] A. R. Hunt and R. D. Hogg, "A stepped-frequency CW radar for concealed weapon detection and through the wall surveillance," *in SPIE Proc. on Sensors and Command, Control, Communications and Intelligence (C3I) Technologies for Homeland Defense and Law Enforcement*, SPIE Proc. vol. 4708, 2002, pp. 99–105.

[6] AKELA, "Demonstration of a concealed weapons detection system using electromagnetic resonances, final report", US Dept. of Justice, 2001, on line: http://www.ncjrs.gov/pdffiles1/nij/grants/190134.pdf

[7] J. Hausner and N. West, "Radar based concealed threat detector," *IEEE MTT-S Int. Microwave Symp.*, June 2007, pp. 765–768.

[8] J. Hausner and N. West, "Radar based concealed threat detector*," IEEE Int. Conference on Microwaves, Communications, Antennas and Electronic Systems*, 2008 (COMCAS 2008), pp. 1–8.

[9] D. L. McMakin, D. M. Sheen, and H. D. Collins, "Remote concealed weapons and explosive detection on people using millimeter-wave holography," *30th Annual 1996 Int. Carnahan Conference on Security Technology*, Oct. 1996, pp. 19–25.

[10] P. E. Keller, D. L. McMakin, D. M. Sheen, A. D. McKinnon, and J. W. Summet, "Privacy algorithm for cylindrical holographic weapons surveillance system," *IEEE AES Systems Mag.*, Feb. 2000, pp. 17–23.

[11] D. M. Sheen, D. L. McMakin, and T. E. Hall, "Three-dimensional millimeter-wave imaging for concealed weapon detection," *IEEE Trans. Microw. Theory Tech*., vol. 49, no. 9, Sep. 2001, pp. 1581–1592.

[12] D. M. Sheen, D. L. McMakin, and T. E. Hall, "Near field imaging at microwave and millimeter wave frequencies," *IEEE MTT-S Int. Microwave Symp.*, June 2007, pp. 1693–1696.

[13] L. Yujiri, M. Shoucri, and P. Moffa, "Passive millimeter-wave imaging," *IEEE Microwave Mag*., Sep. 2003, pp. 39–50.

[14] K. St. J. Murphy, R. Appleby, G. Sinclair, A. McClumpha, K. Tatlock, R. Doney, and I. Hutcheson, "Millimetre wave aviation security scanner," *IEEE 36th Annual Int. Conf. on Security Technology*, 2002, pp. 162–166.

[15] G. Sinclair, R. N. Anderton, and R. Appleby, "Outdoor passive millimetre wave security screening," *IEEE 35th Carnahan Conf. on Security Technologies*, 2001, pp. 172–179.

[16] A. Pergande and L. Anderson, "Video rate millimetre-wave camera for concealed weapon detection," *Proc. SPIE*, vol. 4373, 2001, pp. 35–39.

[17] C. A. Martin, S. E. Clark, J. A. Lovberg, and J. A. Galliano, "Real-time wide-field-of-view passive millimetre-wave imaging," *Proc. SPIE*, vol. 4719, 2002, pp. 341–349.

[18] D. Notel, J. Huck, S. Neubert, S. Wirtz, and A. Tessman, "A compact mmW imaging radiometer for concealed weapon detection," in *Proc. Infrared Millimeter Waves Conf.*, Cardiff, U.K., 2007, pp. 269–270.

[19] **J.J. McCombe**, M.S. Georgiev, T. Thayaparan, and N.K. Nikolova, "Clutter removal in the automatic target detection with late time responses," *European Radar Conference 2013 (EuRAD 2013),* Oct. 2013.

[20] N.K. Nikolova, **J. McCombe**, and T. Thayaparan, "Signal processing algorithms for resonance based concealed weapons detection with microwave radar," Computational Electromagnetics Laboratory Technical Report CEM-R-64, Hamilton, ON, March 2013

[21] **J. McCombe**, "Signal processing algorithms for resonance based concealed weapons detection," Computational Electromagnetics Laboratory Technical Report CEM-R-63, Hamilton, ON, Nov. 2012

[22] R.K. Amineh, **J. McCombe**, A. Khalatpour, and N.K. Nikolova, "Microwave holography using measured point-spread functions," *IEEE Trans. Instrum. & Meas.*, accepted July 2014.

[23] N.K. Nikolova, "Microwave imaging for breast cancer," *IEEE Microw. Mag.,* vol. 12, no. 7, pp. 78 – 94, Dec. 2011.

[24] **J.J. McCombe**, and N.K. Nikolova, "SNR assessment of microwave imaging systems," *IEEE AP-S/URSI Int. Symp. Antennas and Propagation*, July 2014.

[25] **J. McCombe**, "Microwave imaging raw signal-to-noise ratio analysis," Computational Electromagnetics Laboratory Technical Report CEM-R-68, Hamilton, ON, Nov. 2013

[26] K. Moussakhani, **J.J. McCombe**, and N.K. Nikolova, "Sensitivity of microwave imaging systems employing scattering-parameter measurements," *IEEE Trans. Microwave Theory Tech.* accepted July 2014

[27] R.K. Amineh, M. Ravan, **J. McCombe**, and N.K. Nikolova, "Three-dimensional microwave holographic imaging employing forward-scattered waves only," *Int. J. of Antennas and Propagation*, special issue on Inverse Scattering and Microwave Tomography in Safety, Security, and Health, Vol. 2013, Article ID 897287, http://dx.doi.org/10.1155/2013/897287.

[28] R.K. Amineh, **J. McCombe**, and N.K. Nikolova, "Microwave holographic imaging using the antenna phaseless radiation pattern," *IEEE Antennas Wireless Propagat. Lett.,*vol. 11 pp.1529–1532, Dec. 2012.

[29] S. Tu, **J.J. McCombe**, N.K.Nikolova, "Fast quantitative microwave imaging with resolvent kernel extracted from measurements," *Inverse Problems* (submitted Jun. 26, 2014)

[30] S. Tu, **J.J. McCombe**, Y. Zhang, and N.K. Nikolova, "Sensitivity-based imaging of tissue using measurements of calibration objects," *European Microwave Conference (EuMC) 2014*, Oct. 2014, accepted.

[31] K. Moussakhani, **J.J. McCombe**, and N.K. Nikolova, "Sensitivity evaluation of microwave imaging systems employing scattering-parameter measurements," *IEEE AP-S/URSI Int. Symp. on Antennas and Propagation*, July 2014.

[32] R.K. Amineh, M. Ravan, **J.J. McCombe**, and N.K. Nikolova, "Range resolution in microwave imaging with forward-scattered waves only," *IEEE MTT-S Int. Microwave Symp.,* June 2013.

CHAPTER 2

CONCEALED WEAPON DETECTION: THEORY

Introduction

Currently, commercial systems for concealed weapon detection (CWD), such as handheld instruments and walk-through detectors, face many drawbacks. Portable systems require the operator to be close to the individual and make a decision which may be erroneous. Walkthrough detectors as well as portable systems require users to funnel through checkpoints one at a time which causes delays. These detectors have high rates of false positive outcomes and are often sensitive to innocuous metallic objects such as belt buckles and keys. More advanced systems such as full-body scanners produce images that require an operator to make a decision as to the presence of a weapon. The body images are fairly detailed which raises privacy concerns among the general public. Thus, there is need for efficient portable systems that can detect weapons without imaging the body.

2.1. PRINCIPLES OF DETECTION BASED ON TARGET'S LATE TIME RESPONSE

Every structure has intrinsic resonant modes that are dependent on its size, shape and constitutive parameters. This was first exploited in aircraft radar to attempt to determine the aircraft's make based on its unique resonant modes [1][2]. More recently, it has been shown that weapons also have distinctive resonant signatures (set of modes) that could be used to determine the weapon type [1][4]. This information is contained in the late time response (LTR) of a radar signal, which LTR can subsequently be used to detect and possibly identify a weapon [4]-[9] using various classifiers.

In [10], the early time response (specular reflection) is utilized instead of the LTR, to classify the radar return with an Artificial Neural Network Classifier (ANNC). This system, however, operates on millimeter-wave radar signals, where most body-worn weapons do not resonate.

In [9], a variation of an ANNC, called a Learning Vector Quantization (LVQ) network, is utilized to classify the LTR. This classifier distinguishes between measurements of people without weapons and measurements of people with weapons. The authors present successful results using simplified measurements where the weapon is modeled as a sphere (of similar size to a grenade) and a metallic reflecting sheet models the human. The real world, however, is much more complex, with people and weapons having an extremely complex resonance return that varies for each person and weapon. The work

presented in this chapter, partially presented in [11], works with data collected in a cluttered environment on humans, and makes no such simplifications.

A major advantage of a resonant radar return is that it is aspect independent, which means that its resonances do not change based on how the object is positioned in front of the antennas. However, the polarization of the incident wave plays an important role in its ability to excite the major resonances of the object [5] [10] [12]. For this reason, both co-polarized (the receiver and transmitter are of the same polarization) and cross-polarized (the receiver and transmitter are orthogonally polarized) returns must be acquired [5] [10] [13]. In this work, both co- and cross- polarized measurements are utilized. With reference to the polarizations of the transmitting (Tx) and receiving (Rx) antennas, these measurements are denoted V-V, H-H, V-H and H-V, where V and H stand for vertical and horizontal polarizations, respectively, and they are ordered as Tx-Rx.

It should be noted that the method of CWD using the LTR is not an image-based method. The technique aims at generating a positive/negative outcome from the classification and generating a warning when a weapon is suspected. Similar to a metaldetector, further investigation would be required when a warning is issued. The effectiveness of the LTR approach is critically dependent on its ability to identify the resonant signature of an object of interest (weapons) and distinguish it from the background clutter, i.e., reflections from the human body, walls and surrounding furniture or equipment, keys, cell phones, etc. [13]. In [14], it was shown through simulations that the human body can strongly affect the

detectability of a body worn weapon. This negative effect is due to a decrease in the resonance strength as well as shifts in the resonance frequencies of an object. The main goal of this work, initially presented in [11], is to demonstrate through experimental work that with proper clutter suppression, the LTR in co- and cross-polarized measurements can be utilized to detect concealed weapons on persons in an uncontrolled environment.

This work relies on the post-processing of the LTR of a radar return, which is an active area of research in signal processing. In the late 18th century, Prony's method [15] was proposed to estimate the parameters of a series of damped sinusoids. Since then, many algorithms have been developed to extract an object's resonant signature from a radar return. In [3] and [6], the Multiple Signal Classification algorithm is used. In [5], the resonant signature is extracted using the generalized pencil-of-function (PoF) method. In [7] and [9], the Hankel-Total Least Squares algorithm [16] is utilized. The SVD-Prony method or the Kumaresan-Tufts method [17][18] can be utilized to extract the resonances; however, the matrix pencil method, developed by Hua *et al.* [19] is shown to be more robust to noise and more computationally efficient. In [19] [20], the matrix pencil method, a modified version of Prony's method, is used to extract the resonances of a signal represented as the sum of complex exponentials. In this work, the total least squares matrix pencil method applied to electromagnetic scattering by Adve *et al.* [20] and implemented by Georgiev *et al.* [21], herein

referred to as MPM, is implemented to decompose the radar returns of all measurements.

The algorithm for concealed weapon detection can be broken down as follows (note: when stating *measure*, it refers to recording the V-V, V-H, H-V, and H-H returns):

Part 1: Building Classification Library

1. Measure the background (environment with target removed) multiple times
2. Measure each weapon that you wish to detect multiple times
3. Measure a number people with no weapons to serve as the negative class
4. Convert all measurements into the time domain (in the case of frequency-sweep measurements)
5. remove the early-time response from all measurements to obtain their LTR signals
6. Decompose all LTR signals into series of complex exponentials (resonances)
7. Remove all resonances appearing in the background measurements(1.) from target measurements (2. & 3.).
8. Reconstruct the time-domain signals from the reduced series in 7.
9. Convert to the frequency domain for classification and compile into a library
10. Apply a principal component analysis on the library
11. Train the classifier (ANNC, Naive Bayes Classifier, ect.)

Part 2: Operation

12. Measure the background (environment with target removed) multiple times
13. Measure the unknown target response
14. Repeat steps 4. through 8. Using the background from 12.
15. Transform signal into principal components found in 10.
16. Apply target signal to the classier to obtain *threat* or *non-threat* outcome

This algorithm aims to be general in terms of the choice of the resonance-decomposition method and the classification method. To facilitate the use of the MATLAB classification functions, the data is submitted in the frequency domain.

In theory, classification can be made directly using the resonance information, but this requires further work. Here, the goal is to prove that detection is possible with proper clutter removal, not to present an optimized algorithm for concealed weapon detection. For this reason, there is still further work possible on the classification stage of this approach. It should also be noted that in this work, the classification step is utilized in a "black-box" manner. To verify the effectiveness of the clutter suppression, the data are classified utilizing both ANNC as well as a Naive Bayes Classifier (NBC). Moreover, both the ANNC and NBC keep the same structure when classifying data with and without clutter suppression. Principal component analysis is utilized to reduce the number of features used in the classification step. Principal component analysis keeps only the defining features of a weapon so that a weapon that is not included in the training library can still be detected, as shown in [10].

2.2. BACKGROUND REMOVAL

The background removal step of the algorithm aims to find any resonances of objects (furniture, walls, equipment, etc.) in the background environment (with no targets) and remove them from all subsequent measurements taken in the same environment. Since all objects in the background are present when measuring the target, the resonances associated with background clutter are expected to appear in the target return.

2.2.1. Signal Representation

As Hua *et al.* [19] and Adve *et al.* state [20], and repeated here to give the reader full insight, an arbitrary signal *y* as a function of time *t* can be represented as an infinite series of damped sinusoids:

$$y(t) = \frac{a_0}{2} e^{c_0 t} + \sum_{i=1}^{\infty} [a_i \cos(t) e^{c_i t} + b_i \sin(t) e^{d_i t}], \;\; a_0, c_0, a_i, b_i, c_i, d_i \in \mathbb{R}. \quad (2.1)$$

The series in (2.1) can also be represented as a complex-valued exponential series:

$$y(t) = \sum_{i=1}^{\infty} R_i e^{s_i t} \;\; , \quad (2.2)$$

where $R_i, s_i \in \mathbb{C}$ must be chosen such that $y(t) \in \mathbb{R}$ as a time domain signal is purely real-valued. In this representation, R_i includes the initial amplitude of the *i*-th sinusoid as well as its phase. The complex constant $s_i = \alpha_i + j\omega_i$ contains the attenuation constant, $\alpha_i < 0,$ and the angular frequency, $\omega_i = 2\pi f_i$. As we are working with a discretely time sampled signal of length *N*, we must limit the number of sinusoids to *M,* where $M < N$. The infinite series (2.2) is then reduced to a finite series:

$$y(t = k\Delta t) \approx y_k = \sum_{i=1}^{M} R_i e^{s_i k \Delta t}, \;\; k = 0, \ldots, N-1, \quad (2.3)$$

where $y(k\Delta t)$ is the discretely sampled time-domain radar return. We assume that there are *N* equally spaced points in time, starting at $t = 0$ and ending at $t = (N-1)\Delta t$. In order to simplify the series further, we write (2.3) as:

$$y_k = \sum_{i=1}^{M} R_i z_i^k \,,\; z_i = e^{s_i \Delta t} \,, \tag{2.4}$$

where R_i , z_i , and M are the parameters that must be extracted. It should be noted that this formulation only applies to the late time portion of the signal as the signal is assumed to be attenuating.

2.2.2. Parameter Extraction

The parameter-extraction methods discussed here are based on signals represented in the form of (2.4). Other extraction techniques may have a different signal representation. Here, the matrix pencil method [19], in the form that Adve *et al.* [20] proposed, is utilized as it provides a computationally efficient and stable method for computing the parameters. It also provides a method of estimating the number of sinusoids, M, using the singular value decomposition. Other methods assume prior knowledge of the number of sinusoids or estimate them utilizing the minimum description length algorithm.

*A) **Matrix Pencil Method***

The matrix pencil method, proposed in [19] and [20], and implemented by Georgiev in [21], utilizes a matrix pencil to estimate z_i , while M and R_i remain unknown and are solved in the same manner using both the matrix pencil method and the total least squares matrix pencil method . The matrix pencil method works best on noise-free data. As shown by Hua *et al.* [19] and Adave *et al.* [20] and repeated here for completeness, two matrices are considered:

$$\boldsymbol{Y}_1 = \begin{bmatrix} y_1 & y_2 & \cdots & y_L \\ y_2 & y_3 & \cdots & y_{L+1} \\ \vdots & \vdots & \ddots & \vdots \\ y_{N-L} & y_{N-L+1} & \cdots & y_{N-1} \end{bmatrix}_{(N-L)\times L}, \tag{2.5}$$

$$\boldsymbol{Y}_2 = \begin{bmatrix} y_0 & y_1 & \cdots & y_{L-1} \\ y_1 & y_2 & \cdots & y_L \\ \vdots & \vdots & \ddots & \vdots \\ y_{N-L-1} & y_{N-L} & \cdots & y_{N-2} \end{bmatrix}_{(N-L)\times L}, \tag{2.6}$$

where L is the pencil parameter. The matrices in (2.5) and (2.6) are represented as:

$$\boldsymbol{Y}_1 = \boldsymbol{Z}_1 \boldsymbol{R} \boldsymbol{Z}_0 \boldsymbol{Z}_2, \tag{2.7}$$

$$\boldsymbol{Y}_2 = \boldsymbol{Z}_1 \boldsymbol{R} \boldsymbol{Z}_2, \tag{2.8}$$

where, with reference to (2.4),

$$\boldsymbol{Z}_1 = \begin{bmatrix} 1 & 1 & \cdots & 1 \\ z_1 & z_2 & \cdots & z_M \\ \vdots & \vdots & \ddots & \vdots \\ z_1^{(N-L-1)} & z_2^{(N-L-1)} & \cdots & z_M^{(N-L-1)} \end{bmatrix}_{(N-L)\times M}, \tag{2.9}$$

$$\boldsymbol{Z}_2 = \begin{bmatrix} 1 & z_1 & \cdots & z_1^{L-1} \\ 1 & z_2 & \cdots & z_2^{L-1} \\ \vdots & \vdots & \ddots & \vdots \\ 1 & z_M & \cdots & z_M^{L-1} \end{bmatrix}_{M\times L}, \tag{2.10}$$

$$\boldsymbol{Z}_0 = \begin{bmatrix} z_1 & 0 & \cdots & 0 \\ 0 & z_2 & \cdots & 0 \\ \vdots & \vdots & \ddots & \vdots \\ 0 & 0 & \cdots & z_M \end{bmatrix}_{M\times M}, \tag{2.11}$$

$$\boldsymbol{R} = \begin{bmatrix} R_1 & 0 & \cdots & 0 \\ 0 & R_2 & \cdots & 0 \\ \vdots & \vdots & \ddots & \vdots \\ 0 & 0 & \cdots & R_M \end{bmatrix}_{M \times M} . \tag{2.12}$$

Applying the matrix pencil, we obtain:

$$\boldsymbol{Y}_1 - \lambda \boldsymbol{Y}_2 = \boldsymbol{Z}_1 \boldsymbol{R} (\boldsymbol{Z}_0 - \lambda \boldsymbol{I}) \boldsymbol{Z}_2 , \tag{2.13}$$

where $\boldsymbol{I}$ is the M x M identity matrix. It can be shown that as long as $M \le L \le N - M$, the matrix $\boldsymbol{Y}_1 - \lambda \boldsymbol{Y}_2$ has rank M [22]. However, if $\lambda = z_i,\ i = 1, \ldots, M$, the ith row of $(\boldsymbol{Z}_0 - \lambda \boldsymbol{I})$ is zero and the rank of the matrix is $M - 1$. Therefore, the parameters z_i may be considered to be the generalized eigenvalues of the matrix pair $\{\boldsymbol{Y}_1; \boldsymbol{Y}_2\}$. Thus, the problem of estimating z_i can be written as an eigenvalue problem:

$$\boldsymbol{Y}_2^{\dagger} \boldsymbol{Y}_1 - \lambda \boldsymbol{I} = \boldsymbol{0} , \tag{2.14}$$

where $\boldsymbol{Y}_2^{\dagger}$ is the Moore-Penrose pseudo-inverse of $\boldsymbol{Y}_2$.

B) ***Total Least Squares Matrix Pencil Method***

In the presence of noise, the total least squares matrix pencil method is superior. The matrices $\boldsymbol{Y}_1$ and $\boldsymbol{Y}_2$ from (2.5) and (2.6), respectively, are combined into a single matrix:

$$\boldsymbol{Y} = \begin{bmatrix} y_0 & y_1 & \cdots & y_L \\ y_1 & y_2 & \cdots & y_{L+1} \\ \vdots & \vdots & \ddots & \vdots \\ y_{N-L-1} & y_{N-L} & \cdots & y_{N-1} \end{bmatrix}_{(N-L) \times (L+1)} , \tag{2.15}$$

where $L \leq N/2$ [20] is an integer and it is a parameter of the matrix pencil that must be pre-set by the user. A singular value decomposition (SVD) of (2.15) is taken,

$$\boldsymbol{Y} = \boldsymbol{U}\boldsymbol{\Sigma}\boldsymbol{V}^T. \tag{2.16}$$

At this stage, the parameter M in (2.4) is selected based on the singular values in (2.16). If the data were noise-free, there would only be M non-zero singular values in the decomposition. However, due to noise, the zero singular values are perturbed. If we consider the ratio of the ith singular value to the maximum singular value, $\sigma_i/\sigma_{\max} \approx 10^{-p}$, all singular values that have p larger than the number of significant digits in the original signal correspond to noise. Therefore, these singular values should not be used in the reconstruction. On the other hand, if all of the ratios are similar in value, the model of damped sinusoids is not valid; this provides an error check. We choose to define a tolerance fraction τ, which corresponds to the number of significant digits in the data. All singular values less than $\tau\sigma_{\max}$ are set to zero. The choice of τ is critical as choosing τ=0 does not remove any noise, while a large value of τ leads to an inaccurate signal representation. We find by trial and error that a value of $\tau = 10^{-3}$ with a pencil parameter $L = \lfloor N/4 \rfloor$ works best, where $\lfloor\ \rfloor$ denotes the floor operator.

Now, we discard the appropriate rows/columns from $\boldsymbol{U}$, $\boldsymbol{\Sigma}$ and $\boldsymbol{V}$ to create new matrices denoted $\boldsymbol{U}'$, $\boldsymbol{\Sigma}'$ and $\boldsymbol{V}'$. The filtered signal matrix is then reconstructed as:

$$\boldsymbol{Y}' = \boldsymbol{U}'\boldsymbol{\Sigma}'(\boldsymbol{V}')^T . \tag{2.17}$$

Comparing (2.15) to (2.5) and (2.6), we see that $\boldsymbol{Y}_1$ is formed by deleting the first column of $\boldsymbol{Y}$ while $\boldsymbol{Y}_2$ is formed by deleting the last column of $\boldsymbol{Y}$. Therefore, if we use $\boldsymbol{Y}'$ to obtain $\boldsymbol{Y}_1$ and $\boldsymbol{Y}_2$, we would eliminate some of the noise in the data. We can write $\boldsymbol{Y}_1$ and $\boldsymbol{Y}_2$ based on (2.17) as:

$$\boldsymbol{Y}_1 = \boldsymbol{U}'\boldsymbol{\Sigma}'(\boldsymbol{V}_1')^T , \tag{2.18}$$

$$\boldsymbol{Y}_2 = \boldsymbol{U}'\boldsymbol{\Sigma}'(\boldsymbol{V}_2')^T , \tag{2.19}$$

where $\boldsymbol{V}_1'$ and $\boldsymbol{V}_2'$ are the same as $\boldsymbol{V}'$ with the first and last row deleted, respectively. Then, the nonzero eigenvalues of $\boldsymbol{Y}_2^{\dagger}\boldsymbol{Y}_1$ are the poles z_i in (2.4).

Once M and the poles z_i are determined, $R_1 \ldots R_M$ are found by solving the least-squares problem:

$$\begin{bmatrix} y_0 \\ y_1 \\ \vdots \\ y_{N-1} \end{bmatrix} = \begin{bmatrix} 1 & 1 & \cdots & 1 \\ z_1 & z_2 & \cdots & z_M \\ \vdots & \vdots & \ddots & \vdots \\ z_1^{N-1} & z_2^{N-1} & \cdots & z_M^{N-1} \end{bmatrix} \begin{bmatrix} R_1 \\ R_2 \\ \vdots \\ R_M \end{bmatrix} . \tag{2.20}$$

The full source code for the method is found in [21] and [23]. It is important to note that choosing a large value of L can lead to a rank deficient matrix when computing R_i. A study of the effects of L and τ on the eigenmode extraction is presented in [20] and [21].

It is important to acknowledge the contributions of Hua *et al.* and Adave *et al.* who developed this method and have made this CWD technique possible.

2.2.3. Removal of Resonances

Utilizing the MPM to extract the complex resonance parameters of a radar return, we can determine the complex frequency and attenuation pair of any target. Since we can measure the return of our cluttered background environment, we can find its characteristic resonances, too. If we assume that the background environment has not changed between its measurement and the measurement of a target in said environment, its resonances should be present in the data acquired with the target. For this reason, when we decompose a target return, we can expect the resonance information from the target to be mixed with the resonances of the environment. With prior knowledge of the background resonances, we can remove them from the overall measured radar signature, leaving only the resonances of the target.

To remove the clutter resonances, we search through a target measurement and remove all resonances due to the environment. As the amplitude and phase of the sinusoid will change depending on the targets distance from the antenna, we only look at the frequency and attenuation pairs for removing the background. A feature radius ρ_b is utilized to define how close a pole (frequency/attenuation pair) in a target measurement must be to a pole in an environment measurement to be considered clutter. This is necessary due to the noise in the signals, which can cause slightly shifted poles from the MPM. We then search the target signal for any poles z_i that lie within the feature radii and remove them from the target signal.

Once the environment's poles are removed, the target signal is reconstructed from the remaining poles using (2.4). This gives a time-domain signal, which is converted to frequency-domain using the Fast Fourier Transform (FFT). This reconstructed frequency-domain signal is herein referred to as the frequency-domain target-only (FDTO) signal. In principle, the target classification could be performed directly using the parameters from the MPM; however this requires further investigation. For the purpose of this work i.e., removing clutter, the classification step is performed in the frequency domain to allow each discrete frequency to be utilized as a feature of the signal.

2.2.4. Background Removal Example

As an example of this method, consider a background environment signal containing three damped sinusoids:

$$y^{\mathrm{E}}(t) = 5e^{-2\times10^9 t}\cos(2\pi\cdot 3\times10^9 t+\pi) + 2e^{-0.1\times10^9 t}\cos(2\pi\cdot 4\times10^9 t+\pi) + 20e^{-10\times10^9 t}\cos(2\pi\cdot 5\times10^8 t). \tag{2.21}$$

Also consider a target signal (without background) as:

$$y^{\mathrm{T}}(t) = e^{-1\times10^9 t}\cos(2\pi\cdot 2\times10^9 t) + 0.1e^{-0.8\times10^9 t}\cos(2\pi\cdot 1.3\times10^9 t+0.5\cdot\pi). \tag{2.22}$$

The overall measured target signal will be:

$$y_{\mathrm{M}}^{\mathrm{T}}(t) = y^{\mathrm{T}}(t) + y^{\mathrm{E}}(t) + n(t), \tag{2.23}$$

and the measured background environment signal will be:

$$y_{\mathrm{M}}^{\mathrm{E}}(t) = y^{\mathrm{E}}(t) + n(t), \tag{2.24}$$

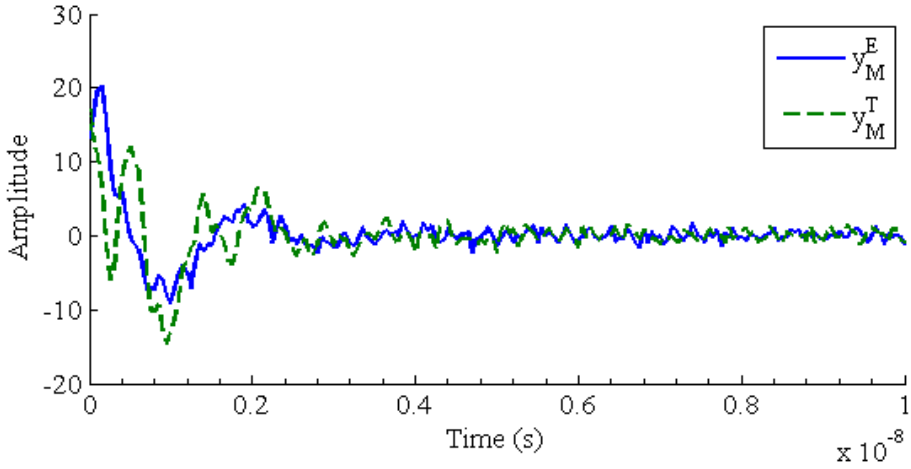

Fig. 2.1. Damped sinusoids corresponding to noisy signals of the background environment (2.24), solid line, and the measured target signal(2.23), dashed line.

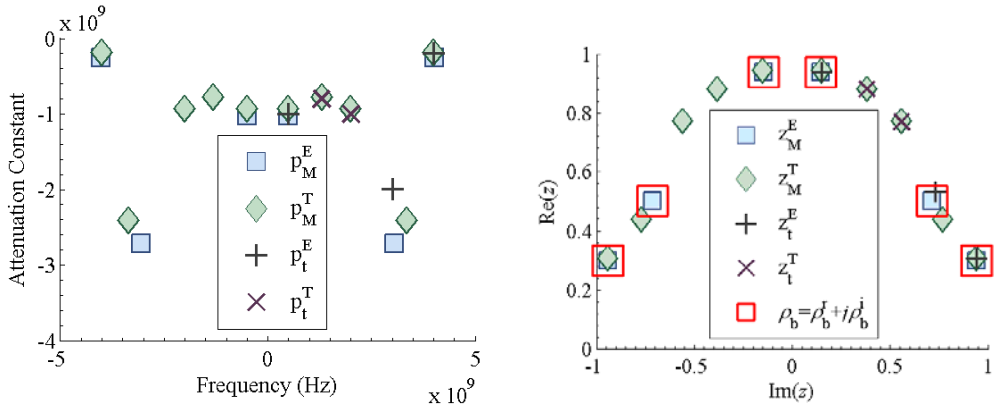

(a) (b)

Fig. 2.2. Scatter plot of: (a) the estimated frequency and attenuation of the measured environment (blue squares), measured target (green diamonds), true environment (plus signs), and true target (crosses); (b) the real and imaginary portion of the poles of the measured environment (blue box), measured target (green diamond), true environment (plus signs), and true target (crosses), along with the feature radius (red box), in true scale. The feature radius is shown in (b) because the background removal is done directly on the poles. Note that the plot in (a) compares well with the values in (2.21) and (2.22).

where $n(t)$ is noise. Decomposing both y_M^E and y_M^T, shown in Fig. 2.1, with the MPM yields the frequency/attenuation pairs shown in Fig. 2.2 (a). The

background removal is done directly on the poles, without extracting the attenuation and frequency values, as shown in Fig. 2.2 (b).

In this example, additive white Gaussian noise is added to the measured signals so that the signal-to-noise ratio is 15 dB. As Fig. 2.2 (a) shows, the extracted values from the noise data differ slightly from the true values, but are very close. It is also evident that the background poles are present in the target measurements. However, the target measurement poles due to the background do not fall in the same location as the target poles extracted from the background environment without targets. For this reason the feature radius must be defined. This radius is a complex value that denotes how much variation in attenuation and frequency is allowed while still considering the pole to be due to the environment. This feature radius is shown by the red boxes in Fig. 2.2 (b). The poles in the target measurement that fall within the feature radius are removed and the background free target signal is reconstructed via (2.4).

TABLE 2.1 shows the extracted parameters along with the true parameters for the measured target signal, (2.23), and measured environment (2.24). Note that, like the Fourier Transform, the MPM extracts negative frequencies that have half of the true amplitude. Also note that the target signal does contain the parameters of the environment (green rows) along with the true target parameters (blue rows). There is also one erroneous parameter (red row), however, since its amplitude is relatively small, it will contribute little to the reconstructed signal. This parameter also has a higher frequency and could be removed if a frequency

TABLE 2.1: EXTRACTED AND TRUE SIGNAL PARAMETERS FOR TARGET AND ENVIRONMENT MEASUREMENT

Measurement	Frequency (GHz)		Attenuation ($\cdot 10^9$)		Amplitude		Phase (rad)	
	Estimated	True	Estimated	True	Estimated	True	Estimated	True
Target	5.8601 -5.8601	~	-0.0987 -0.0987	~	0.1098 0.1098	~	1.5626 -1.5626	~
	3.9923 -3.9923	4	-0.1790 -0.1790	-0.1	0.9628 0.9628	2	-2.8041 2.8041	π
	3.3573 -3.3573	3	-2.4095 -2.4095	-2	3.0925 3.0925	5	2.5387 -2.5387	π
	-0.4988 0.4988	0.5	-0.9262 -0.9262	-1	9.8390 9.8390	20	-0.0019 0.0019	0
	1.3070 -1.3070	1.3	-0.7708 -0.7708	-0.8	7.3094 7.3094	15	1.5327 -1.5327	0.5π
	1.9968 -1.9968	2	-0.9332 -0.9332	-1	2.6515 2.6515	5	-0.1108 0.1108	0
Environment	4.0172 -4.0172	4	-0.2570 -0.2570	-0.1	0.9811 0.9811	2	3.0016 -3.0016	π
	3.0496 -3.0496	3	-2.7129 -2.7129	-2	2.7243 2.7243	5	2.9721 -2.9721	π
	0.4966 -0.4966	0.5	-1.0238 -1.0238	-1	10.3299 10.3299	20	0.0277 -0.0277	0

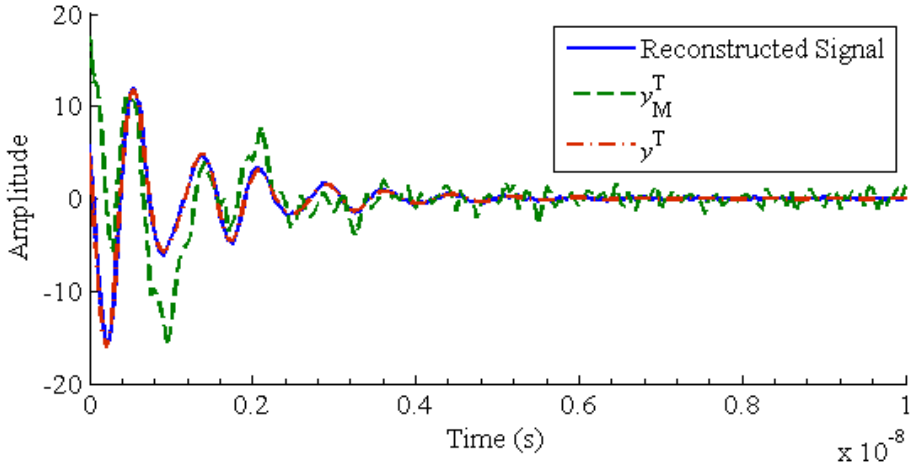

Fig. 2.3. Reconstructed target signal (solid blue line) after background removal according to (2.4), noisy target signal with background components (green dashed line), and true target signal (red dash-dot line).

band is imposed on the data. After removing all poles in the measured target signal that fall within the feature radius of the measured environment, the remaining poles are used to reconstruct the time domain signals of the target alone. Fig. 2.3 shows the reconstructed signal after background removal (solid blue line), along with the measured target signal (dashed green line) and the true target signal (dash-dot red line). Even though the erroneous pole was included in the reconstruction, the reconstructed signal matches the true signal almost perfectly, even though the measured signal is very different. It is also apparent that the MPM has eliminated most of the noise that was added to the measured signal and returned a noise-free signal. This demonstrates that with proper background removal, a true target response can be extracted from a cluttered noisy environment.

2.2.5. Choice of Feature Radius ρ_b

The feature radius should be chosen such that the majority of poles due to the background environment are removed without affecting the target response. The choice must also reflect the level of uncertainty in the extraction, which is related to the tolerance τ of the MPM. The feature radius must be greater than or equal to the tolerance in the MPM as the MPM tolerance dictates the expected level of noise. For example, if we set $\tau = 10^{-3}$ in the MPM, the extracted poles are only accurate to this degree, in the best case scenario. To verify the choice of feature radius, we can compare the number of background poles extracted from the MPM of the background measurement with the number of poles removed

TABLE 2.2: PERCENTAGE OF BACKGROUND POLES REMOVED

ρ_b	Man	Weapon	Man + Weapon
0.01	99.41%	99.61%	98.80%
0.005	91.63%	95.08%	91.26%
0.001	17.34%	28.74%	17.25%

from the target. In principle, the same number of background poles should be present in the target measurement, and ideally all should be removed. A larger choice of feature radius can yield a larger number of removed poles. However the more poles that are removed, the more likely it is that some of the poles from a complicated target are also removed. A study of this nature is presented in Chapter 3. For different system designs, the noise levels change, and τ and ρ_b should be adjusted accordingly.

TABLE 2.2 shows the ratio of the number of poles that were removed from a signal to the number of background poles. Average values for measurements of man, weapon, and man-with-weapon measurements are shown. Although ρ_b = 0.01 removes more background poles, the classification is poor because it is also removing some target information. We have empirically determined that ρ_b = 0.005 removes enough of the background clutter while maintaining enough target information to perform successful classification.

2.3. TARGET CLASSIFICATION METHODS

There are multitudes of classification algorithms currently in existence and new methods are developed continuously. As this work is focused on the

reduction of radar clutter, two target classification methods were chosen based on their well-developed software and ease of use. The Naïve Bayes Classifier (NBC) [24], available in MATLAB's Statistics Toolbox, and the Artificial Neural Network Classifier (NNC) [25], available in MATLAB's Neural Network Toolbox, can easily be applied to the problem of pattern recognition in concealed weapon detection. To make use of these algorithms, different features (or metrics) must be submitted to the classifier for training and classification. Based on these features, which must be the same for each signal, the algorithms generate probabilities of the classified signal belonging to each class of the training data. Because we must have the same features for each measurement, we use the magnitude of the FDTO signal at each frequency point as a feature. As this means having as many features as frequency points, a Principal Component Analysis (PCA)[26] is performed using MATLAB's Statistics Toolbox [24] on the training data to reduce the number of features that the classification is based on to only those that contribute the most information. This also allows for the detection of weapons that are not in the training database, but have a similar profile to those that are in the database [10].

Before classification, the magnitudes of the FDTO signal at all frequency points, for each polarization, are combined into one feature vector. All of the training data is the combined into one training set $\boldsymbol{R}$ as

$$\boldsymbol{R} = \begin{bmatrix} \boldsymbol{r}^1_{\text{V-V}} & \boldsymbol{r}^1_{\text{V-H}} & \boldsymbol{r}^1_{\text{H-V}} & \boldsymbol{r}^1_{\text{H-H}} \\ \boldsymbol{r}^2_{\text{V-V}} & \boldsymbol{r}^2_{\text{V-H}} & \boldsymbol{r}^2_{\text{H-V}} & \boldsymbol{r}^2_{\text{H-H}} \\ \vdots & \vdots & \vdots & \vdots \\ \boldsymbol{r}^m_{\text{V-V}} & \boldsymbol{r}^m_{\text{V-H}} & \boldsymbol{r}^m_{\text{H-V}} & \boldsymbol{r}^m_{\text{H-H}} \end{bmatrix}, \tag{2.25}$$

where ***r*** is a row vector containing the magnitude of the FDTO radar return and H & V denote the transmitting and receiving polarizations. The superscript denotes the target number and the subscript denotes the antenna configuration. A principle component analysis is carried out on ***R*** to reduce the dimensionality of the classification problem.

2.3.1. Naïve Bayes Classifier

A naïve Bayes classifier operates under the assumption that a value of a particular feature is unrelated to the value of any other feature for a given class, in other words, each feature is independent of all other features, hence the term naïve. Although the design of the classifier operates under oversimplified assumptions, they have been shown to work well on real data. The classification algorithm is described well in many pattern recognition and classification texts, such as Dougherty [27] and Bishop [28], but is briefly outlined here for completeness.

The naïve Bayes classifier utilizes Bayes theorem, which states that:

$$p(c_j|f_i) = \frac{p(f_i|c_j)p(c_j)}{p(f_i)}, \tag{2.26}$$

where $p(c_j|f_i)$ is the probability of the *i*-th feature f_i belonging to the *j*-th class c_j, $p(f_i|c_j)$ is the probability of generating the feature f_i given the class c_j, $p(c_j)$ is the probability of class c_j occurring, and $p(f_i)$ is the probability of the feature f_i occurring. In simpler terms, $p(c_j|f_i)$ is the classification outcome; $p(f_i|c_j)$ represents class cj causing feature fi to occur with some probability; $p(c_j)$

represents how frequent the class cj is in the training data; and, $p(f_i)$ is assumed equal for all classes and can be ignored. Extending to the case of classification with multiple features, under the assumption that each feature is independent (a naïve assumption), we write:

$$\begin{aligned} p(c_j|s) &= p(c_j|f_1) * p(c_j|f_2) * \ldots * p(c_j|f_n), \\ &= p(c_j) * p(f_1|c_j) * p(f_2|c_j) * \ldots * p(f_n|c_j), \\ &= p(c_j) \prod_{i=1}^{n} p(f_i|c_j), \end{aligned} \tag{2.27}$$

where $p(c_j|s)$ is the probability of signature *s* belonging to class c_j and f_i, $i = 1,\ldots,n$, is the *i*-th feature of the signature. The naïve Bayes classifier assigns a test signature to the class that has the maximum *a posterior* probability. As described in [27], as long as the correct class is the most probable, the classifier arrives at the correct decision. This implies that the class probabilities do not necessarily need to be estimated well, which means that the classifier is sufficiently robust to overcome the naïve probability model.

2.3.2. Artificial Neural Network Classifier

In contrast to the statistics-based classifiers, like the naïve Bayes classifier, artificial neural network classifiers mimic the central nervous systems of animals. Neural networks are well established and used in many classification and pattern recognition topics. Artificial neural networks are explained in simple terms by Dougherty in [29] and by Duda *et al.* [30]. Briefly, the neural networks consist of multiple layers of nodes. The nodes in adjacent layers are all interconnected with unidirectional links. Each link to a node is assigned a weight. At a node, the sum of the link values is passed through a threshold function and the output of this

node becomes an input to the next layer of nodes. The outputs typically fall between 0 and 1 but can exceeded these values. Typically, a threshold is set and values above it are determined to belong to that class and values below it do not.

Fig. 2.4 shows an example of a neural network that contains one input layer (L1), two hidden layers (L2 & L3) and an output layer (L4). The inputs to the network are the n features of the signature. There are N^{L2} nodes in the first hidden layer and N^{L3} nodes in the second hidden layer, with m output nodes, one for each class. Each layer has a bias node that helps to correct the value after summation so that it falls between 0 and 1. The weights are applied at the output of each node. For example, at the first node of the first hidden layer, all of the inputs are first summed, then passed through the threshold function and the output of the threshold has the weight W_1^{L2} applied to it. For NNC classification, the neural network toolbox of MATLAB is used to generate a neural network classifier with 100 input nodes, 100 nodes in the first hidden layer, 10 nodes in the second hidden layer and 5 nodes in the output layer, as shown in Fig. 2.5. This corresponds to utilizing 100 features and 5 classes and is adjusted for each dataset to obtain optimal results. Each node contains a 'tansig' transfer function and the conjugate gradient back-propagation method is used for training. The size and the structure of the training dataset and the test dataset vary for each measurement and are discussed later as appropriate.

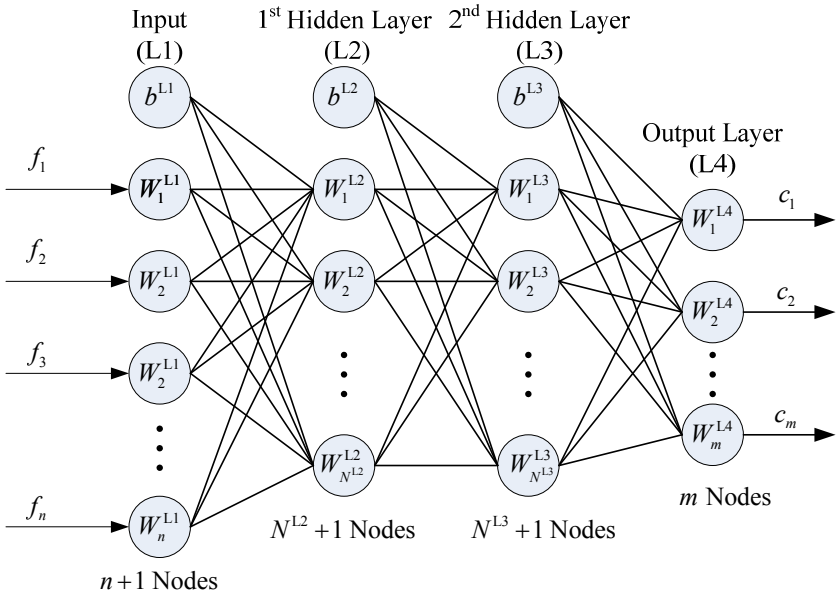

Fig. 2.4. General structure of a neural network with two hidden layers. f_i is the i-th feature of a signature with n features. b^{Lj} denotes the bias for the j-th layer, and W_k^{Lj} is the weight function for the k-th node of the j-th layer. m is the number of classes, n is the number of features, N^{L2} is the number of nodes in the first hidden layer, and N^{L3} is the number of nodes in the second hidden layer.

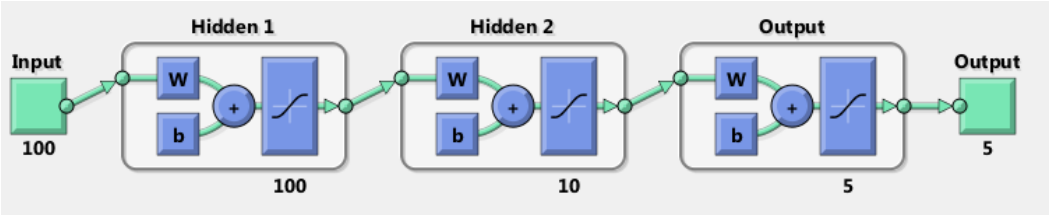

Fig. 2.5. Structure of the four-layer feed-forward Matlab NNC if 5 classes and 100 features are used. A 'tansig' transfer function is used at each node, with a conjugate gradient back-propagation method used for training.

2.3.3. Classifier Performance Metrics

A) Confusion Matrix

The confusion matrix is a common method of displaying the classifier's outcome in a compact manner. For a single class classifier, it breaks the output data into four categories, true positive, false negative, true negative, and false positive.

Actual Class	Predicted Class	
	Non-Threat	Threat
Non-Threat	TN	FP
Threat	FN	TP

Fig. 2.6. The 2x2 confusion matrix. The columns correspond to the predicted class (outcome of classifier) and the rows correspond to the actual class. TP, FN, FP, and TN correspond to true positive, false negative, false positive, and true negative, respectively. The cells shaded in green are correct predictions and the cells shaded in red correspond to incorrect prediction.

Actual Class	Predicted Class				
	No Weapon	Weapon 1	Weapon 2	Weapon 3	Weapon 4
No Weapon	20	0	1	1	0
Weapon 1	0	5	1	0	1
Weapon 2	2	1	3	3	1
Weapon 3	2	5	0	10	0
Weapon 4	0	0	1	0	2

Fig. 2.7. The 5x5 confusion matrix for a 5-class classifier. In this ficticious scenario, 22 measurements of a man without weapon, 7 measurements of a man with Weapon 1, 10 measurements of a man with Weapon 2, 17 measurements of a man with Weapon 3, and 3 measurements of a man with Weapon 4 are submitted.The cells shaded in green correspond to measurements that were correctly predicted. The cells shaded in red were incorrectly predicted.

True positive occurs when the input signal has a weapon and the classifier correctly identifies it as a threat. False negative occurs when the input signal has a weapon and the classifier incorrectly identifies it as non-threat. True negative occurs when there is no weapon and the classifier correctly identifies it as non-threat. False positive occurs when there is no weapon and the classifier incorrectly identifies it as a threat. In

Fig. 2.6, a sample 2x2 confusion matrix is shown for a final outcome of the classification stage, with only threat and non-threat classes possible. In a classifier with multiple classes, such as one designed to distinguish between weapon types,

a larger confusion matrix is needed. For example, Fig. 2.7 shows a 5x5 confusion matrix for a classifier that aims to detect between four possible weapon types. From the confusion matrix, the sensitivity, specificity, and accuracy of the classifier can be determined.

B) ***Receiver Operating Characteristic Curve***

A receiver operating characteristic (ROC) curve is a 2-dimensional plot of the false positive rate, $FP/(TN+FP)$, vs. the true positive rate (sensitivity) [31]. A classifier is operating perfectly if it operates at the point (0,1), corresponding to a false positive rate of zero and a true positive rate of 1. The point (0,0) corresponds to a classifier that always issues a negative result and the point (1,1) corresponds to a classifier that always issues a positive result. Classifiers operating in the upper left region of the plot have good performance. The closer a curve is to (0,1) the better the classifier's performance. A curve is created by adjusting the threshold level of a classification decision. Both the NNC and NBC yield scores or probabilities, and a threshold is used to produce a true/false or class decision, where all outputs above the threshold level are positive and all below are negative.

2.4. CONCLUSIONS

An algorithm for the detection of concealed weapons in a cluttered environment is proposed. The algorithm relies on the suppression of the environmental clutter through the analysis of the resonance information from the background. Once the effects of the background are removed, classification is

performed using prior measurements of weapons alone and people without weapons. Testing is performed using measurements of people with and without weapons on their body. This provides the framework for a functional concealed weapon detection system.

It should be emphasized that the classification and PCA are used here as "black box" tools to demonstrate the effectiveness of the background removal approach. In light of this, the classification and PCA parameters are kept constant and not adjusted for any examples. All conclusions should be considered with this in mind.

REFERENCES

[1] R. Carrier and R.L. Moses, "High resolution radar target modeling using a modified Prony estimator," *IEEE Trans. Antennas and Propagation*, vol. 40, no. 1, pp. 13–18, Jan 1992.

[2] E. Rothwell, D.P. Nyquist, K.M. Chen, and B. Drachman, "Radar target discrimination using the extinction-pulse technique," *IEEE Trans. Antennas Propag.*, vol. 33, no. 9, pp. 929–937, Sept. 1985.

[3] S. Ibrahim, K.R. Liu, D. Novak, and R.B. Waterhouse, "A subspace signal processing technique for concealed weapons detection," *IEEE International Conference on Acoustics, Speech and Signal Processing*, Honolulu, HI, 2007.

[4] S.W. Harmer, D.A. Andrews, N.D. Rezgui, and N.J. Bowring, "Detection of handguns by their complex natural resonant frequencies", *IET Microwave, Antennas & Propagation*, vol. 4, no. 9 , pp. 1182–1190, Sept. 2010.

[5] M. Gashinova, M. Cherniakov, and A. Vasalos, "UWB signature analysis for detection of body-worn weapons," *in International Conference on Radar*, Shanghai, 2006.

[6] A. Vasalos, I. Vasalos, H. Ryu, and S. Fotinea, "LTR analysis and signal processing for concealed explosive detection," *in German Microwave Conference*, Berlin, 2010.

[7] A. Vasalos, I. Vasalos, H. Ryu, and S. Fotinea, "Fast concealed weapon detection via LTR analysis," *in IEEE Radar Conference*, Kansas City, MO, 2011.

[8] A. Vasalos, I. Vasalos, H. Ryu, and S. Fotinea, "LTR analysis for fast concealed weapon detection," *in German Microwave Conference*, Darmstadt, 2011.

[9] A. Vasalos, N. Uzunoglu, H. Ryu, and I. Vasalos, "Neural network target classification for concealed weapon radar detection", *in International Conference on Digital Signal Processing*, Fira, Greece, 2013.

[10] D. O'Reilly, N. Bowring, and S. Harmer, "Signal processing techniques for concealed weapon detection by use of neural networks," *IEEE 27th Convention of Electrical & Electronics Engineers in Israel (IEEEI*), Eilat, Israel, 2012.

[11] J.J. McCombe, M.S. Georgiev, T. Thayaparan, and N.K. Nikolova, "Clutter removal in the automatic detection of concealed weapons with late time responses," *European Radar Conference (EuRAD),* Nuremberg, Germany, 2013.

[12] N. Shuley and D. Longstaff, "Role of polarization in automatic target recognition using resonance descriptions," *Electronic Lett.*, vol. 40, no. 4, Feb. 2004.

[13] N. K. Nikolova, "Ultrawideband (UWB) high-resolution noise radar for concealed weapon detection," Technical Report to DRDC–Ottawa, Hamilton, ON, June 30, 2009.

[14] N. K. Nikolova, "Ultrawideband (UWB) high-resolution noise radar for concealed weapon detection," Technical Report to DRDC–Ottawa, Hamilton, ON, July 23, 2010.

[15] R. Prony, "Essai experimental et analytique sur les lois de la dilatabilite de fluides elastiques et sur celles del la force expansive de la vapeur de l'alkool a differentes temperatures," *Paris J. I'Ecole Polytech*., vol. 1, pp. 24–76, 1795.

[16] S.E. Fotinea, I. Dologlou, and G. Carayannis, "On the use of decimation for efficient spectral estimation", *International Journal of Computer Mathematics and its Applications*, vol. 8, Oct. 2006

[17] R. Kumaresan and D.W. Tufts, "Estimating the parameters of exponentially damped sinusoids and pole-zero modeling in noise," *IEEE Trans. Acoustics, Speech, and Signal Processing*, vol. 30, no. 6, pp. 833–840, 1982.

[18] G.K. Allu, "Estimating the parameters of exponentially damped sinusoids in noise," Technical Report, University of Rhode Island, Kingston, Rhode Island, 02881, April 2003.

[19] Y. Hua and T.K. Sarkar, "Matrix pencil method for estimating parameters of exponentially damped/undamped sinusoids in noise," *IEEE Trans. Acoustics, Speech, and Signal Processing*, vol. 38, no. 5, pp. 814–824, May 1990.

[20] R.S. Adve, O.M. Pereira-Filho, T.K. Sarkar, and S.M. Rao, "Extrapolation of time domain responses from three dimensional objects utilizing the matrix pencil technique," *IEEE Trans. Antennas Propag.*, vol. 45, pp. 147–156, Jan. 1997.

[21] M. Georgiev and N.K. Nikolova, "Ultrawideband (UWB) high-resolution noise radar for concealed weapon detection," Technical Report to DRDC–Ottawa, Hamilton ON, April 2012.

[22] F. Hu, "The band-pass matrix pencil method for parameter estimation of exponentially damped/undamped sinusoidal signals in noise," Ph.D. Thesis, Syracuse Univ., 1990.

[23] N.K. Nikolova, J.J. McCombe, and T. Thayaparan, "Signal processing algorithms for resonance based concealed weapons detection with microwave radar," Computational Electromagnetics Laboratory Technical Report CEM-R-64, Hamilton ON, March 2013.

[24] MathWorks, "Statistics Toolbox R2012b," [Online]. Available: http://www.mathworks.com/products/datasheets/pdf/statistics-toolbox.pdf

[25] MathWorks, "Neural Network Toolbox R2012b," [Online]. Available: http://www.mathworks.com/help/nnet/index.html

[26] J.P. Reilly. ECE 712. Lecture 8, Topic: "The pseudo-inverse". Department of Electrical and Computer Engineering, McMaster University, Hamilton, ON, Nov. 2012, Available: http://www.ece.mcmaster.ca/~reilly/ece712/course_notes.htm

[27] G. Dougherty, "Statistical Pattern Recognition," in *Pattern Recognition and Classification: An Introduction*. New York, NY: Springer, 2013, ch.4, pp. 43–54.

[28] C.M. Bishop, *Pattern Recognition and Machine Learning*. New York, NY: Springer, 2006.

[29] G. Dougherty, "Nonparametric Learning," in *Pattern Recognition and Classification: An Introduction*. New York, NY: Springer, 2013, ch. 6, pp. 104–117.

[30] R.O. Duda, P.E. Hart, and D.G. Stork, "Multilayer Neural Networks," in *Pattern Classification*. *2*nd ed. New York, NY: Weily, 2001, ch. 6, pp. 282-333.

[31] T. Fawcett, "An introduction to ROC analysis," *Pattern Recognition Letters*, vol. 27, no. 8, pp. 861–874, June 2006.

CHAPTER 3

CONCEALED WEAPON DETECTION: FREQUENCY-SWEEP MEASUREMENTS

Introduction

Preliminary measurements have been performed where a frequency-sweep radar system is developed based on a vector network analyzer (VNA) which acts as both a transmitter and a receiver. The VNA measures complex the *S*-parameters of a two-port system, which represent the ratio of received power to transmitted power. Here, two systems are developed to: 1) perform a feasibility study of our proposed resonance-based concealed weapon system and 2) determine if the system can operate in an environment different from the environment where it was trained.

3.1. PRELIMINARY FREQUENCY-SWEEP MEASUREMENTS

The preliminary measurements designed, organized and carried out by M. Georgiev and N.K. Nikolova. Many thanks to their efforts which pushed this project forward.

3.1.1. System Configuration

In the preliminary frequency-sweep measurements, the system consists of a single two-port VNA [1]. Each port is connected to a custom designed Vivaldi antenna that is well matched in the band from 0.5 GHz to 5 GHz [2]. Three antenna arrangements were used: (a) H-H, (b) V-V and (c) H-V, where H denotes horizontal polarization and V denotes vertical polarization. In the H-H measurement, both the transmitting and the receiving antenna are oriented horizontally with respect to ground. In the V-V arrangement, both are oriented vertically. In the H-V measurement, the transmitting antenna is horizontal while the receiving antenna is vertical. The frequency is swept from 0.5 GHz to 5 GHz with 3201 frequency points, 3 kHz IF bandwidth, averaging set to 2, and a sweep time of 1.0518 s.

First, three measurements of the background environment with no targets are taken. Then, each weapon is measured alone in the same environment. The measurements of the weapons are taken in a single orientation as the resonances are aspect independent. However, measuring the weapon from different viewing angle may increase the strength of the specific resonance which could improve the classification.

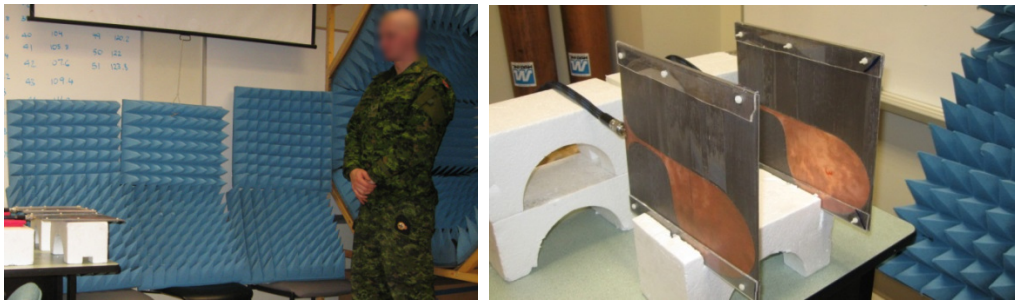

(a) (b)

(c)

Fig. 3.1. Photos of the initial frequency-sweep measurements showing: (a) H-H arrangement of the antennas with a measurement taken approximately 150 cm from the antennas; (b) transmitting and receiving antenna in a V-V arrangement; (c) H-V arrangement with a measurement of a weapon taken approximately 60 cm from the antennas.

Next, four different measurements are taken of a man:

1) man without any weapons,
2) man with a weapon located on his body's front,
3) man with a weapon located on his body's side,
4) man with a weapon located on his body's back.

Measurements 2 to 4 are repeated with three different weapons described in Section 3.1.2. All four measurements are repeated for a man wearing a thin jacket and a thick (winter) jacket. All measurements are also repeated at two distances, 60 cm (near) from the radiating edge of the antenna and 150 cm (far) from the radiating edge of the antenna. Photos of the setup are shown in Fig. 3.1.

(a)

(b) (c)

Fig. 3.2. Photos of: (a) the knife (weapon 1), (b) the small gun, *Sig Sauer P225* (weapon 2), and (c) the large gun, *Browning 9mm* (weapon 3).

3.1.2. Targets

For the preliminary measurements, the Military Police division in Toronto provided two guns and a knife. Weapon 1 (W1) is a knife, shown in Fig. 3.2 (a), approximately 30 cm long. Weapon 2 (W2) is a small handgun, *Sig Sauer P225*, shown in Fig. 3.2 (b) with an approximately 16 cm long barrel and a 12 cm long handle. Weapon 3 (W3, Fig. 3.2 (c)) was a large handgun, *Browning 9 mm*, with an approximately 18 cm long barrel and a 12 cm long handle.

3.2. Preliminary Frequency-Sweep Results

In the presented results, the background has been removed from all target measurements using the MPM described in Section 2.2.2. We consider two

classes, Class 0 and Class 1, representing *non-threat* outcome and *threat* outcome, respectively. In the training matrix, we use the measurements of both men without weapons near the antennas as non-threat targets while the measurements of the weapons alone are used as threat targets. This dataset contains 36 measurements of people with weapons, 4 measurements of people without weapons and 2 measurements of each weapon alone. For training purposes, all measurements of weapons were used and 2 measurements of people without weapons were used. Both a BNC and a NNC are used for classification and their results are compared.

3.2.1. Classification Schemes

In the preliminary measurements two classification schemes are performed. The first classification scheme utilizes training data partitioned into two classes; *threat* and *non-threat*, where any weapon is given the *threat* class and people without weapons are given a *non-threat* class. The two outcomes of the classifier are combined with equal weight to determine the final outcome. This scheme is herein referred to as the single classifier scheme.

The second classification scheme partitions the training data into individual weapon classes. In this scenario each weapon is given its own class, i.e., *non-threat, W1, W2, W3*. The maximum probability returned from the three weapon classifiers is used as the *threat* probability. This is then combined with the *non-threat* outcome with equal weight to determine the final outcome. This scheme is herein referred to as the individual classifier scheme.

3.2.2. Naïve Bayes Classifier

A) ***Confusion Matrix***

Fig. 3.3 shows the confusion matrix for the single classifier scheme. For this scenario, one measurement of a man without a weapon was classified as *threat* and five measurements of man with a weapon were classified as *non-threat*.

Fig. 3.4 (a) shows the confusion matrix from the individual classifier scheme. Note that weapon 1 is the knife and weapons 2 and 3 are the guns. This classifier did not correctly identify the knife and instead, 8 of the measurements were classified as gun and 2 were classified as *non-threat*. When combining all weapon results into a single threat class, we obtain the confusion matrix in Fig. 3.4 (b), where we have improved the number of false negatives by 1.

B) ***Sensitivity, Specificity, and Accuracy***

The confusion matrix in Fig. 3.3 gives a sensitivity of 86%, a specificity of 75% and an accuracy of 85%. The confusion matrix in Fig. 3.4 (b) yields a sensitivity of 88.9%, a specificity of 75%, and an accuracy of 87.5%. There are good results, although not all weapons were correctly classified by type (most weapon measurements were classified as a different type of weapon).

C) ***ROC Curves***

For both classification schemes, we are able to detect the weapons at an acceptable rate, considering the low amount of training data used. Fig. 3.5 shows the ROC curve for the single classifier scheme and the classifier operates at a reasonable level.

Actual Class	Predicted Class	
	Non-Threat	Threat
Non-Threat	3	1
Threat	5	31

Fig. 3.3. 2x2 confusion matrix for the NBC with a single classifier scheme.

Actual Class	Predicted Class			
	No Weapon	Weapon 1	Weapon 2	Weapon 3
No Weapon	3	0	1	0
Weapon 1	2	0	8	2
Weapon 2	2	0	8	2
Weapon 3	0	0	8	4

(a)

Actual Class	Predicted Class	
	Non-Threat	Threat
Non-Threat	3	1
Threat	4	32

(b)

Fig. 3.4. (a) 4x4 confusion matrix for the NBC with the individual classifier scheme. (b) Resulting 2x2 confusion matrix where any positive output from (a) is considered a threat.

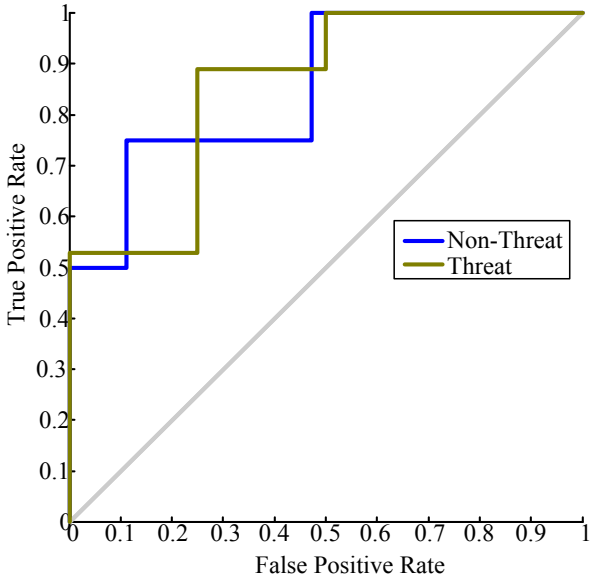

Fig. 3.5. ROC curve for the single classifier scheme using the NBC.

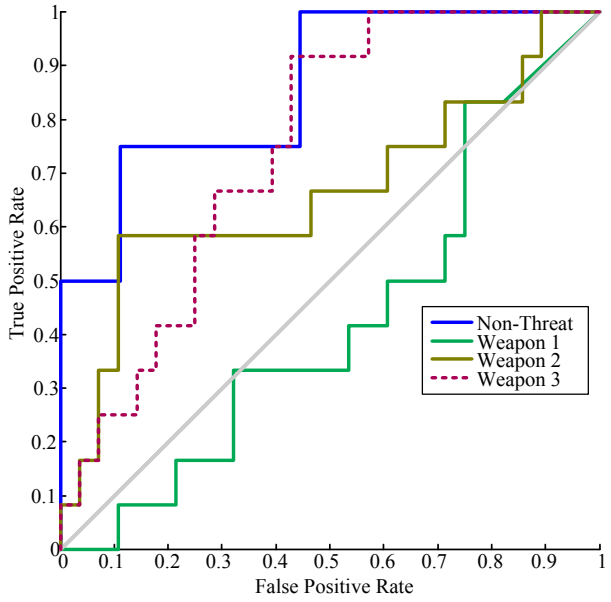

Fig. 3.6. ROC curve for the individual classifier scheme using the NBC.

Fig. 3.6 shows the ROC curve for the individual classifier scheme. It shows that the *non-threat* classification is fairly successful while the *Weapon 1* classification does not perform well.

Fig. 3.7 shows the classifier output vs. measurement index for the single classifier scheme. The detection is good for the *near* measurements with only one incorrect classification. For the *far* measurements, the classification is worse, with five wrong classifications. The sensitivity with *near* measurements is 94%; the specificity is 100% and the accuracy is 95%. For the *far* measurements, the sensitivity is 77%; the specificity of 50% and the accuracy is 75%. This suggests that the performance is better at distances closer to the antennas where the weak resonances are more easily detected. We can also see that at farther distances, the classification does not perform well with the thick jacket data. This may suggest that thick clothing may impact the classification, especially if it is thermal and

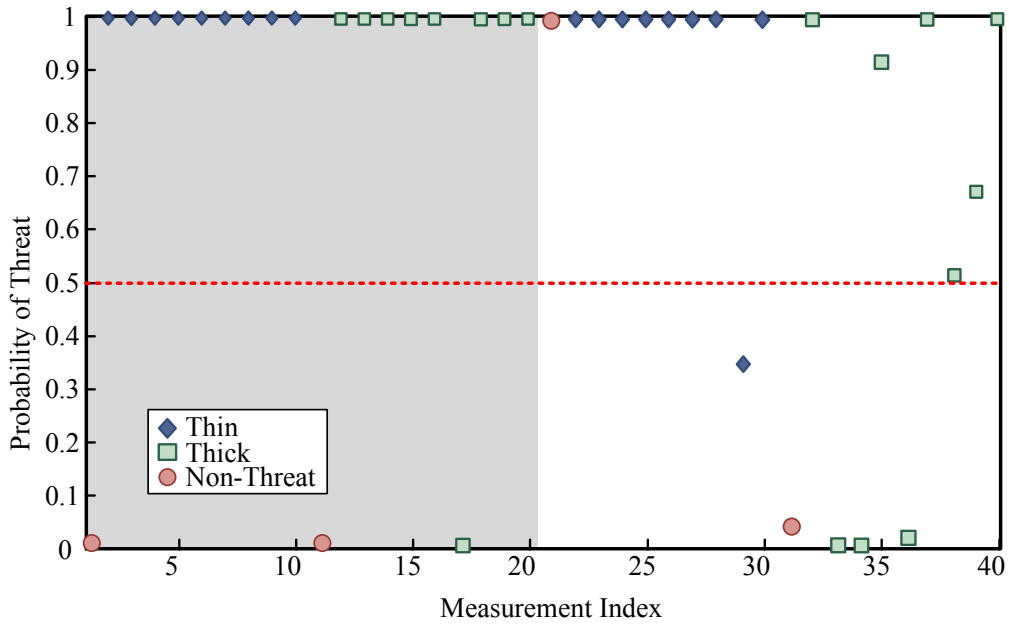

Fig. 3.7. Classifier outputs for the NBC when using the single classifier scheme. Blue diamonds correspond to *threat* measurements with a thin jacket. Green squares correspond to *threat* measurements with a thick jacket. Red circles correspond to *non-threat* measurements. Data in the grey and white areas correspond to near and far measurements, respectively. A background removal tolerance of 0.005 is used. Note that in the *far* measurements, four *threat* targets are assigned a probability of threat below 50%, i.e., they are incorrectly classified.

may include some heat reflective liners that can also reflect electromagnetic waves.Fig. 3.8 shows the confusion matrices when no background removal is performed and when background removal is performed with tolerances of 0.001 and 0.01. In all three cases, the number of correct *threat* classifications is high; however, two of the four *non-threat* targets are classified incorrectly, moreover, they have a high probability of *threat* (> 0.9). This shows that we are unable to distinguish between *threat* and *non-threat* in these cases. However when we use a tolerance of 0.005 as shown in the previous results, the classification is good.

Actual Class	Predicted Class	
	Non-Threat	Threat
Non-Threat	2	2
Threat	1	35

(a)

Actual Class	Predicted Class	
	Non-Threat	Threat
Non-Threat	2	2
Threat	4	32

(b)

Actual Class	Predicted Class	
	Non-Threat	Threat
Non-Threat	2	2
Threat	5	31

(c)

Fig. 3.8. 2x2 confusion matrix for the NBC when using a single classifier scheme for: (a) background removal tolerance of 0 (no removal), (b) background removal tolerance of 0.001, and (c) background removal tolerance of 0.01.

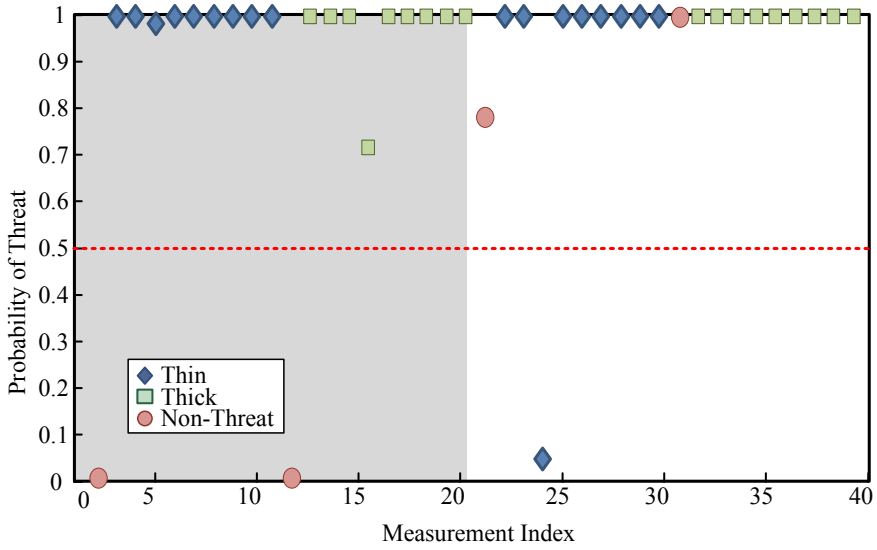

Fig. 3.9. Classifier outputs for the NBC when using a single classifier scheme. Blue diamonds correspond to *threat* measurements with a thin jacket. Green squares correspond to *threat* measurements with a thick jacket. Red circles correspond to *non-threat* measurements. Data in the grey and white areas correspond to near and far measurements, respectively. No background removal is performed.

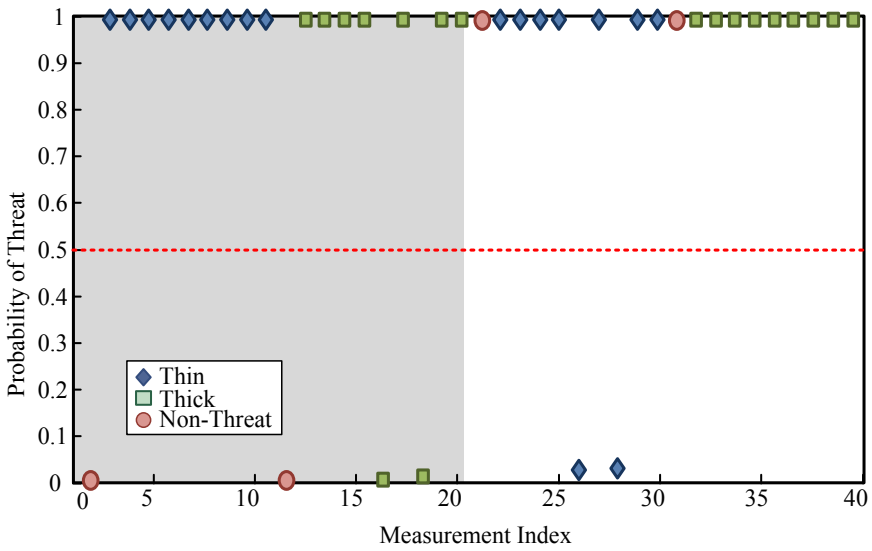

Fig. 3.10. Classifier outputs for the NBC when using a single classifier scheme. Blue diamonds correspond to *threat* measurements with a thin jacket. Green squares correspond to *threat* measurements with a thick jacket. Red circles correspond to *non-threat* measurements. Data in the grey and white areas correspond to near and far measurements, respectively. Background removal with a tolerance of 0.001 is performed.

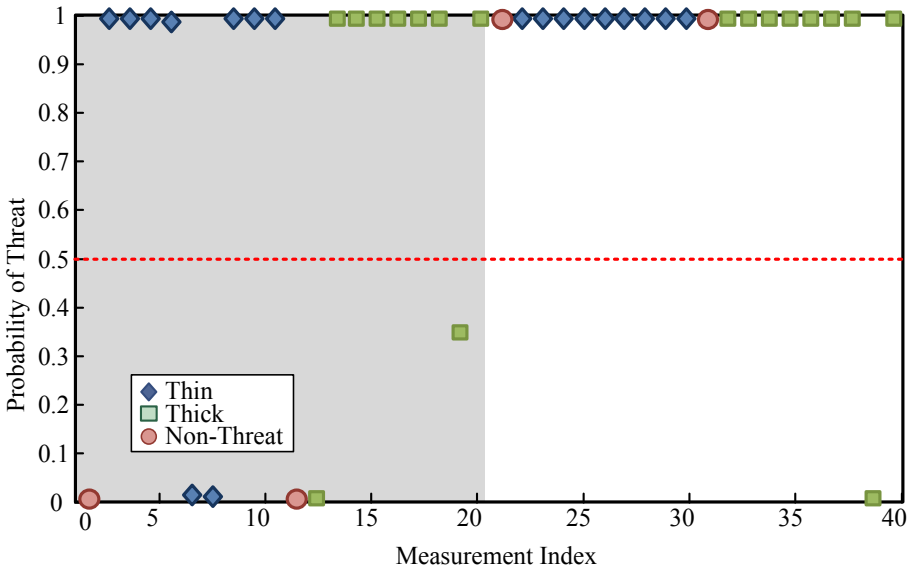

Fig. 3.11. Classifier outputs for the NBC when using a single classifier scheme. Blue diamonds correspond to *threat* measurements with a thin jacket. Green squares correspond to *threat* measurements with a thick jacket. Red circles correspond to *non-threat* measurements. Data in the grey and white areas correspond to near and far measurements, respectively. Background removal with a tolerance of 0.01 is performed.

Actual Class	Predicted Class	
	Non-Threat	Threat
Non-Threat	4	0
Threat	3	33

Fig. 3.12. 2x2 confusion matrix for the NNC using the single classifier scheme.

Fig. 3.9 shows the classifier outputs when no removal is performed. The first two *non-threat* points were in the training set so they are classified well, however the other two points are not. Fig. 3.10 shows the output when a removal tolerance of 0.001 is utilized, still the *non-threat* targets are not classified well. Fig. 3.11 shows the output when a removal tolerance of 0.01 is utilized and again, the *non-threat* measurements are not classified well. For these reasons, a removal tolerance of 0.005 is chosen, however the lack of test data does not allow for a rigorous study of these effects in this prelimiary study.

3.2.3. Neural Network Classifier

*A) **Confusion Matrix***

Fig. 3.12 shows the confusion matrix for the single classifier scheme using the NNC. All men without weapons were classified correctly and three men with weapons were classified as *non-threat*. This is an improvement over the NBC, however, due to the small training set, these are not definitive results, especially due to the low number of measurements of men without weapons. However, these results are promising enough to warrant further work.

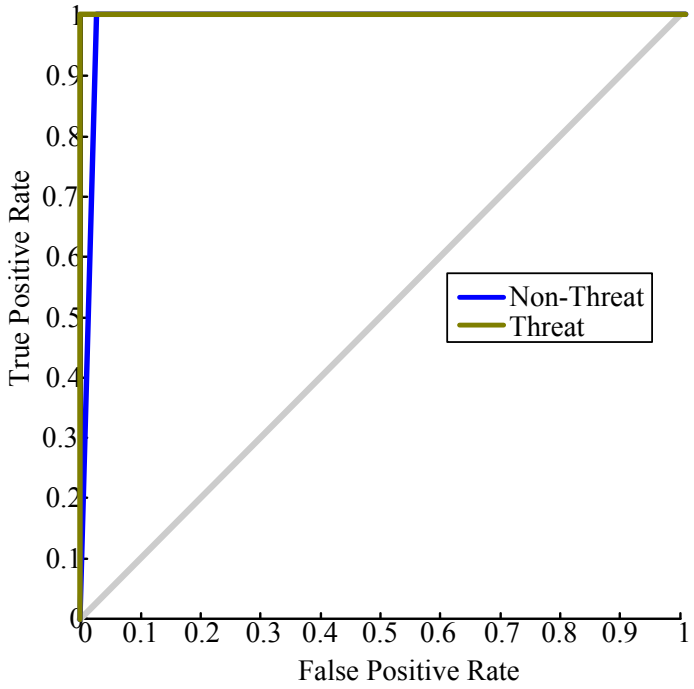

Fig. 3.13. ROC curve for the NNC using a single classifier scheme.

B) ***Sensitivity, Specificity, and Accuracy***

The confusion matrix in Fig. 3.12 gives a sensitivity of 91.7%, a specificity of 100% and an accuracy of 92.5%. These results are better than those obtained with the NBC.

C) ***ROC Curve***

With the NNC and the use of single classifier scheme, the outcome has shown some improvement with respect to the NBC. This is shown by the ROC curve in Fig. 3.13. Although there are less misses with the NNC, the probabilities of threat are not as strongly separated as those from the NBC. With the NNC, we see a slightly lower probability of threat for the *near* measurements

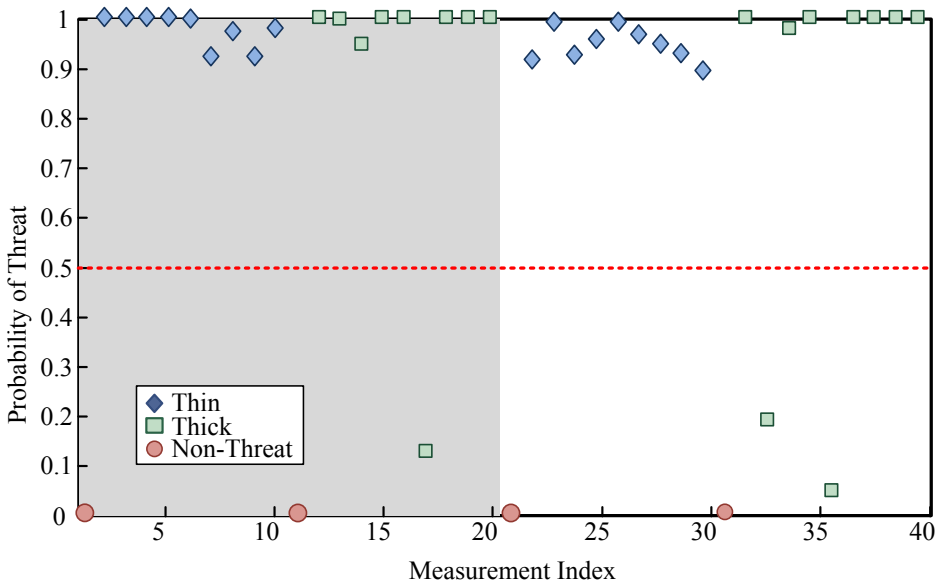

Fig. 3.14. Classifier outputs for the NNC when using a single classifier scheme. Blue diamonds correspond to *threat* measurements with a thin jacket. Green squares correspond to *threat* measurements with a thick jacket. Red circles correspond to *non-threat* measurements. Data in the grey and white areas correspond to near and far measurements, respectively. A background removal tolerance of 0.005 is used.

compared to the NBC. Overall, both classifiers perform well. Yet more measurements of people without weapons are needed to truly demonstrate the detection ability.

3.3. Measurements with Frequency-Sweep Laboratory Prototype

One problem that arises in classification is the ability to classify signals that come from measurements taken in an environment that is different from that of the training data.

3.3.1. Detection in Two Environments

A) Classification in a Single Environment

In the case of classification in a single environment, all measurements are taken in the same environment, i.e., training and test data are acquired with the same background. This means that the training data (measurements of weapons only and measurements of people only) are taken in the same environment that the system is deployed in. In a commercial system, this would mean building a new database for each deployment site, which is not feasible.

B) Full Training in One Environment and Classification in Another

Full training in one environment and classification in another is the ideal situation. The training data is acquired at a development site before deployment (could be in an anechoic chamber). The system is then deployed to a second environment and should be able to operate. This may cause issues as the background removal process may not be ideal and the background can still affect the data. However, a loss of sensitivity or specificity may be made up for by having a larger training database as many measurements of multiple weapons and people are possible in an anechoic environment. Also, further limited training at the site of deployment is also possible, especially for the *non-threat* classifier. This is described next.

C) Partial Training in One Environment and Classification in Another

Partial training in one environment and classification in another is a hybridisation between the two previous cases. In this scenario, the training data is partially acquired in one environment, then some additional measurements are taken in the deployment site and added to the training data. The classifier would

then be trained, verified and continuously improved at the deployment site. In this scenario, all of the measurements of weapons and some measurements of people could be done in a remote, possibly anechoic site, and the additional measurements of people in the deployment site can be added to the training data to improve the outcome. This allows for the continuous improvement of the classifiers leading to improved results in the particular environment.

3.3.2. System Configuration

The system used in the frequency-domain laboratory prototype consists of two dual-polarized, ridge-horn antennas [4] (see Fig. 3.15) that are connected to a four-port VNA [3]. These antennas are well impedance matched between 300 MHz to 6 GHz and allow for fast co- and cross-polarized measurements. As before, the frequency is swept from 0.5 GHz to 5 GHz with 3201 frequency points, 3 kHz resolution bandwidth, and averaging set to 2.

Measurements were taken in two environments as follows:

1) 10 repeated measurements of the background,
2) 5 repeated measurements of each weapon alone,
3) 3 repeated measurements of a person without a weapon,
4) 3 repeated measurements of a person with a weapon concealed on the front or side of their body, in an arbitrary orientation.

Measurements 2 to 4 were repeated for the targets positioned at 60 cm (near) from the antenna aperture and 120 cm (far) from the antenna aperture.

*A) **Description of Environment 1***

Environment 1 was the same environment used in the measurements described in 3.1. This environment has a relatively small amount of clutter that is

present in all measurements. Microwave absorbers are placed to partially cover adjacent metallic surfaces and to reduce some of the reflections. Fig. 3.15 shows a sample photo of a weapon-only measurement in environment 1.

B) ***Description of Environment 2***

Environment 2 is a cluttered environment shown in Fig. 3.16. This environment has many sources of clutter (furniture, equipment, etc.) at many distances from the antennas that affect all measurements. As shown in Fig. 3.16 (a), measurements of the background only are taken without people. As shown in Fig. 3.16 (b), measurements of people with and without weapons are taken in the same environment where people are free to move. This adds additional clutter and makes the environment more realistic.

3.3.3. Targets

For these measurements, we utilized four different weapons. Weapon 1 (W1), Fig. 3.17 (a), is an approximately 33 cm kitchen knife. Weapon 2 (W2), Fig. 3.17 (b), is a plastic pellet gun that has been wrapped in aluminum foil to make it conductive; the gun has an approximately 20 cm barrel length with a 12 cm long handle. Weapon 3 (W3), Fig. 3.17 (c), is a small knife that is approximately 21 cm long. Weapon 4 (W4) is an extendable baton that is approximately 20 cm long, Fig. 3.17 (d), and approximately 50 cm long when extended, Fig. 3.17 (e).

Fig. 3.15. Photo of weapon only measurement of a baton in environment 1.

(a) (b)

Fig. 3.16. Photo of radar system in environment 2 recording: (a) background only measurements (b) measurements of people with/without weapons in cluttered background.

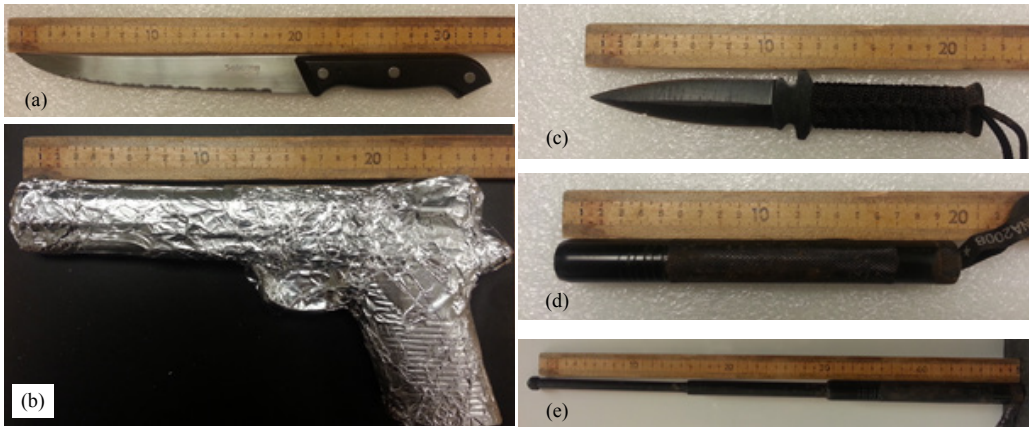

Fig. 3.17 Photos of the weapons used in the laboratory prototype measurements: (a) kitchen knife (Weapon 1), approximately 33 cm long, (b) foil-wrapped pellet gun (Weapon 2) approximately 20 cm barrel length with 12 cm long handle, (c) small knife (Weapon 3) approximately 21 cm long, (d) baton (Weapon 4) approximately 20 cm long, and (e) extended baton, approximately 50 cm long.

3.4. RESULTS FROM THE FREQUENCY-SWEEP LABORATORY PROTOTYPE

3.4.1. Classification Schemes

For the following results, three classification schemes are used. The first two schemes are the same as those presented in Section 3.2.1, namely the single classifier scheme and the individual classifier scheme.

The third classification scheme partitions the training data into weapon group classes. In this scenario, each broad weapon type category is given its own class, i.e., *non-threat, gun, knife, baton.* The maximum probability return from the weapon classifiers is used as the *threat* probability, which is then combined with the *non-threat* outcome to determine the final outcome. This scheme is herein referred to as the group classifiers scheme.

When classifying the data with multiple classes, each class is in effect a classifier that operates independently. Thus, several classifiers may return an output above the threshold. For example, the class probability for one of our test vectors is 0.6 for Weapon 1 and 0.8 for Weapon 2. Both are above the threshold of 0.5. For the confusion matrices in this section, the class with the larger probability is the predicted class. A NNC, as described in Section 2.3.2, is utilized for detection in these experiments.

3.4.2. Classification in a Single Environment

First, we test the effectiveness of a classifier that is trained and operating in one environment as a benchmark for the performance of a classifier that is deployed in an environment different from that in which it is trained.

A) ***Confusion Matrices***

For training and classifying in a single environment with a single classifier scheme, the results are poor, with 14 people with weapons being classified as *non-threat*, out of 36 total, as seen in Fig. 3.18.

When using the individual classifier scheme, the results per weapon are still weak, with only two correct classifications, as seen in Fig. 3.19 (a); however, only 3 measurements of people with weapons were classified as *non-threat*. When combining the outcomes of all weapon classifiers so that any positive weapon outcome leads to an overall *threat*, the results improve significantly, as can be seen in Fig. 3.19 (b).

When classifying using the group classifiers scheme, the results are improved over the *threat/non-threat* scheme, but not as good as the individual weapon scheme, which can be seen in Fig. 3.20. This demonstrates that the algorithm performs best under the individual classifier scheme.

Actual Class	Predicted Class	
	Non-Threat	Threat
Non-Threat	29	7
Threat	14	22

Fig. 3.18. 2x2 confusion matrix for the NNC using the single classifier scheme. Training and testing are done in environment 1.

Actual Class	Predicted Class				
	No Weapon	Weapon 1	Weapon 2	Weapon 3	Weapon 4
No Weapon	34	0	1	0	1
Weapon 1	1	0	3	0	2
Weapon 2	0	1	0	9	2
Weapon 3	2	0	0	0	4
Weapon 4	0	0	6	4	2

(a)

Actual Class	Predicted Class	
	Non-Threat	Threat
Non-Threat	34	2
Threat	3	33

(b)

Fig. 3.19. (a) 5x5 confusion matrix for the NNC using the individual classifier scheme. (b) 2x2 confusion matrix where any positive output from (a) results in a *threat* outcome. Training and testing are done in environment 1.

Actual Class	Predicted Class			
	No Weapon	Knife	Gun	Baton
No Weapon	33	0	3	0
Knife	10	0	1	1
Gun	2	0	0	10
Baton	2	0	3	7

(a)

Actual Class	Predicted Class	
	Non-Threat	Threat
Non-Threat	33	3
Threat	14	22

(b)

Fig. 3.20. (a) 4x4 confusion matrix for the NNC using the group classifiers scheme. (b) 2x2 confusion matrix where any positive output from (a) results in a *threat* outcome. Training and testing are done in environment 1.

*B) **Sensitivity, Specificity, & Accuracy***

Based on the confusion matrix in Fig. 3.18 using the single classifier scheme, the sensitivity is 61%, the specificity is 80.5%, and the accuracy is 70.8%. When using the individual classifier scheme and setting any positive outcome for a weapon as a final *threat* outcome the sensitivity becomes 91.6%, the specificity is 94.4%, and the accuracy is 93%, see Fig. 3.19. It is clear that although the weapon classification is not correct, the individual classifier scheme outperforms the single classifier scheme. When using the group classifiers scheme, the sensitivity is 61.1%, the specificity is 91.6%, and the accuracy is 76.4%.

*C) **ROC Curves***

Fig. 3.21 shows the ROC curve when using the single classifier scheme from Fig. 3.18. This curve shows that the classifier is better at correctly determining the *non-threat* data.

Fig. 3.22 (a) shows the ROC curves when using the individual classifier scheme from Fig. 3.19. This figure shows that the *non-threat* classifier performs adequately, however the weapon classifiers do not perform well. When combining the outcomes, the results improve significantly, as shown in Fig. 3.22 (b). The final result is obtained by averaging the outcome of the *threat* and 1–*non-threat* probabilities with equal weight.

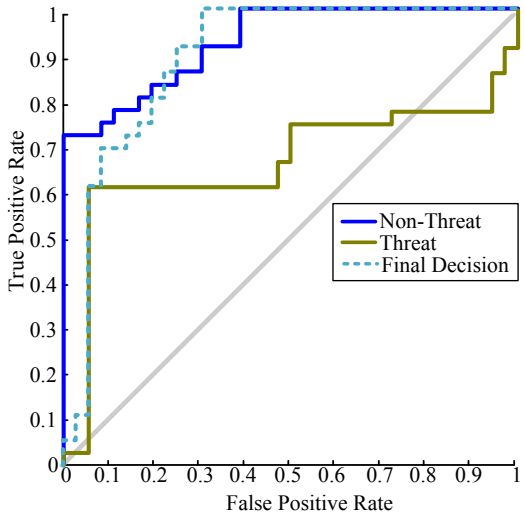

Fig. 3.21. ROC curve for the NNC when using the single classifier scheme. Training and testing are done in environment 1.

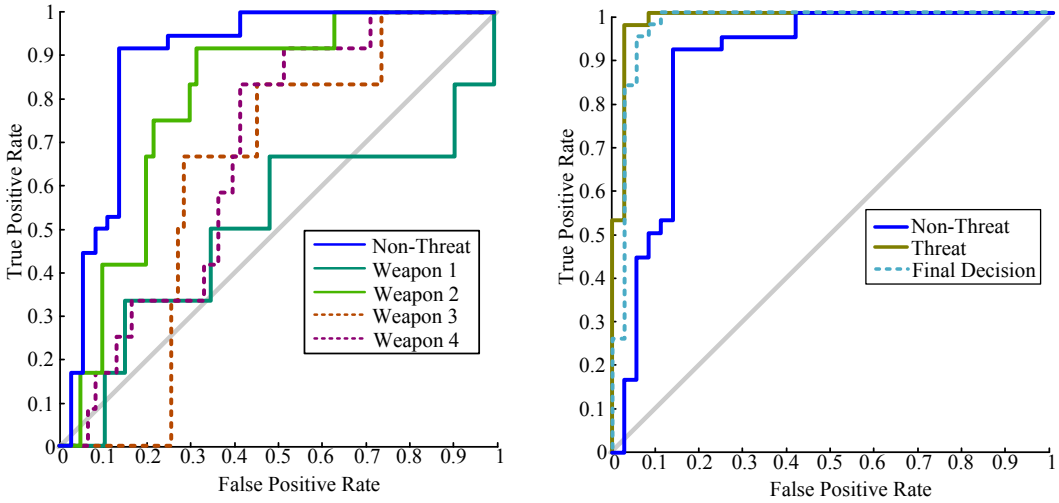

(a) (b)

Fig. 3.22. ROC curves for the NNC when using the individual classifier scheme: (a) individual weapon classifiers; (b) *threat* and *non-threat* outcome where any positive result is set to *threat* along with the final decision which is an average between the two classes. Training and testing are done in environment 1.

When using the group classifiers scheme, from Fig. 3.20, the weapon group classifiers perform better than the individual weapon classifiers, but the final decision is not as good as the individual classifier scheme, as shown in Fig. 3.23.

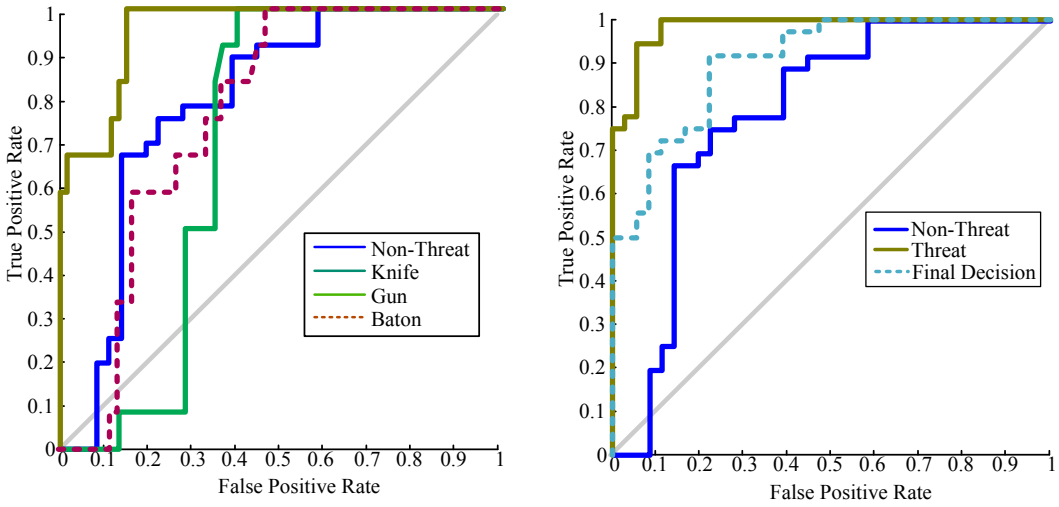

(a) (b)

Fig. 3.23. ROC curves for the NNC when using the group classifiers scheme: (a) weapon group classifiers; (b) *threat* and *non-threat* outcome where any positive result is set to *threat* along with the final decision which is an average between the two classes. Training and testing are done in environment 1.

3.4.3. Full Training in One Environment and Classification in Another

A) Confusion Matrices

When acquiring training data in one background and classifying in a second, the results are not acceptable. As shown in Fig. 3.24, when using the single classifier scheme, only 4 people with weapons are classified correctly. When using the individual classifier scheme, Fig. 3.25, only 2 people without weapons and 26 people with weapons are correctly classified.

When using the group classifiers scheme, Fig. 3.26, the results are still poor with only one person without weapons and 26 people with weapons are correctly classified. This is a poor result and would not be acceptable for a concealed weapon detection system.

Actual Class	Predicted Class	
	Non-Threat	Threat
Non-Threat	27	9
Threat	32	4

Fig. 3.24. 2x2 confusion matrix for the NNC using the single classifier scheme when training data is acquired in environment 1 and test data is acquired in environment 2.

Actual Class	Predicted Class				
	No Weapon	Weapon 1	Weapon 2	Weapon 3	Weapon 4
No Weapon	2	7	0	10	17
Weapon 1	0	0	0	3	3
Weapon 2	4	4	0	2	2
Weapon 3	3	2	0	0	1
Weapon 4	3	2	0	0	7

(a)

Actual Class	Predicted Class	
	Non-Threat	Threat
Non-Threat	2	34
Threat	10	26

(b)

Fig. 3.25. Results for the NNC using the individual classifier scheme: (a) 5x5 confusion matrix for each individual weapon class; (b) 2x2 confusion matrix where any positive output from (a) results in a *threat* outcome. Training is done in environment 1 with testing in environment 2.

Actual Class	Predicted Class			
	No Weapon	Knife	Gun	Baton
No Weapon	1	8	0	27
Knife	3	1	0	8
Gun	3	0	0	9
Baton	4	2	0	6

(a)

Actual Class	Predicted Class	
	Non-Threat	Threat
Non-Threat	1	35
Threat	10	26

(b)

Fig. 3.26. Results for the NNC using the individual classifier scheme: (a) 4x4 confusion matrix for each weapon group; (b) 2x2 confusion matrix where any positive output from (a) results in a *threat* outcome. Training is done in environment 1 with testing in environment 2.

B) ***Sensitivity, Specificity, & Accuracy***

Based on the confusion matrix in Fig. 3.24 when using the single classifier scheme, the sensitivity is 11%, the specificity is 75%, and the accuracy is 43%. When using the individual classifier scheme from Fig. 3.25, the sensitivity becomes 27%, the specificity is 5.5%, and the accuracy is 38.8%. When using the group classifiers scheme from Fig. 3.26, the sensitivity becomes 72%, the specificity is 2.7%, and the accuracy is 37.5%. It is clear that training in one environment and deploying in a second environment is not successful.

C) ***ROC Curves***

Fig. 3.27 shows the ROC curve when using the single classifier scheme from Fig. 3.24, and the performance is unacceptably poor.

When using the individual classifier scheme from Fig. 3.25, the ROC curves in Fig. 3.28 show no improvement over the single classifier scheme.

When using the group classifiers scheme from Fig. 3.26, the results are still poor, as shown by the ROC curves in Fig. 3.29. This level of performance is unacceptably low and must be improved. This can be accomplished by updating the training data set with *non-threat* data acquired in environment 2. This result also shows that the background removal is not ideal and there is still some influence of the background on the data submitted for classification.

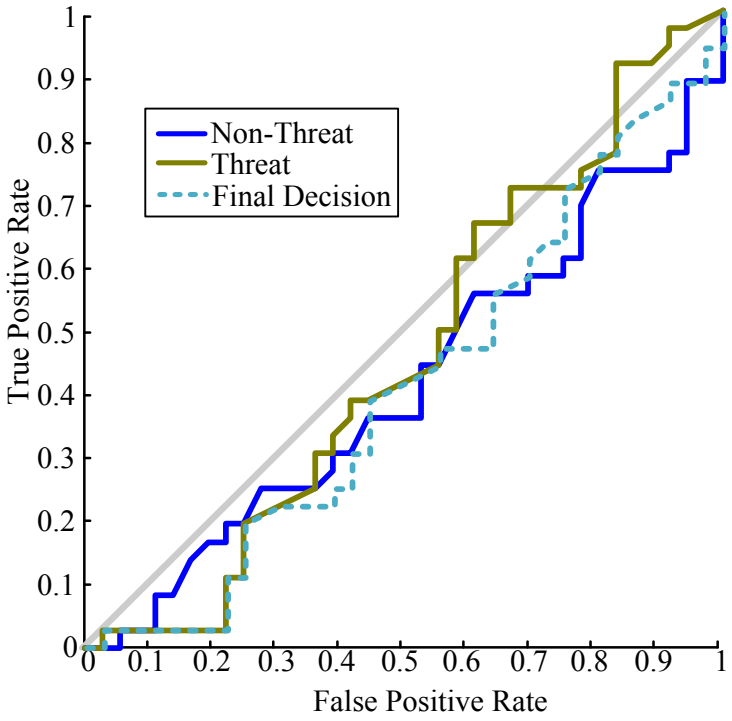

Fig. 3.27. ROC curve for the NNC when using the single classifier scheme. Training is done in environment 1 with testing in environment 2.

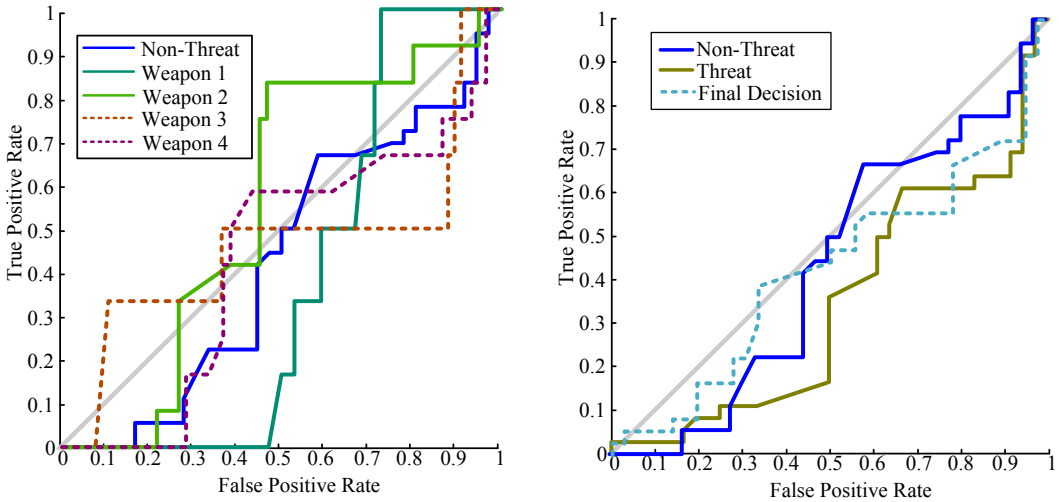

(a) (b)

Fig. 3.28. ROC curves for the NNC when using the individual classifier scheme: (a) individual weapon classifiers; (b) *threat* and *non-threat* outcome where any positive result is set to *threat* along with the final decision which is an average between the two classes. Training is done in environment 1 with testing in environment 2.

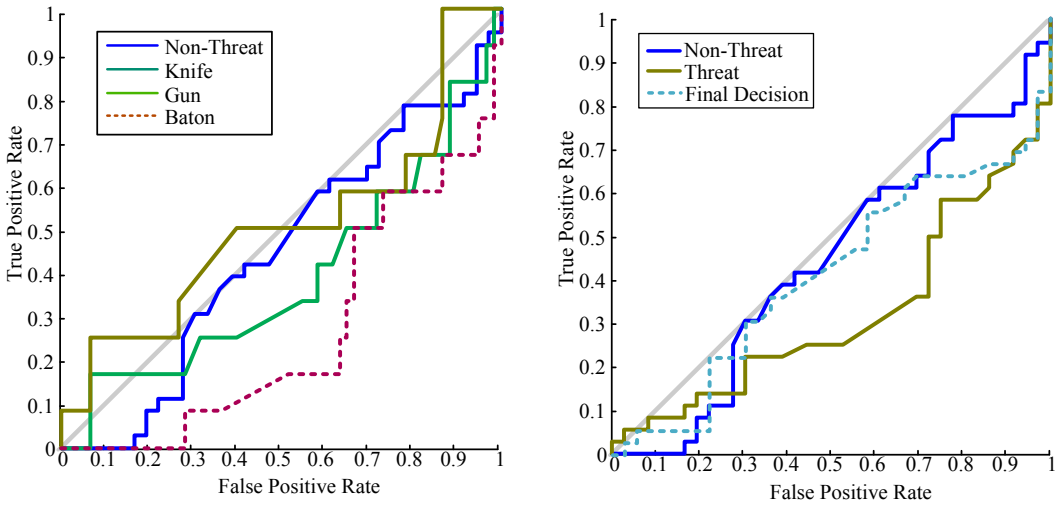

(a) (b)

Fig. 3.29. ROC curves for the NNC when using the group classifiers scheme: (a) weapon group classifiers; (b) *threat* and *non-threat* outcome where any positive result is set to *threat* along with the final decision which is an average between the two classes. Training is done in environment 1 with testing in environment 2.

3.4.4. Partial Training in One Environment and Classification in Another

The next best option for a practical system is to acquire a training set of different weapons in one environment and acquire training data of people without weapons in the deployment site. Then training of the classifier would be done on site. This is practical because most people going through the system will not have weapons and the classifier can learn on site.

A) Confusion Matrices

When using the single classifier scheme shown in the confusion matrix in Fig. 3.30, all measurement of people without weapons are classified correctly and 14 out of 36 measurements of people with weapons are classified correctly.

Using the individual classifier scheme, shown in the confusion matrix in Fig. 3.31, 1 person without a weapon is classified as *threat* and 1 person with a weapon was classified as *non-threat*.

Using the group classifiers scheme, shown in the confusion matrix in Fig. 3.32, the results are still good with only 5 incorrect classifications. This shows that by allowing the NNC to re-train in the deployment environment, the classification can again be successful. This also demonstrates that the background environment is still incorporated in the measurements. However, the clutter suppression method works well and, provided the classifier can re-train, concealed weapon detection can be carried out without measuring weapons in the deployment environment.

B) ***Sensitivity, Specificity, & Accuracy***

Based on the confusion matrix in Fig. 3.24, when using the single classifier scheme, the sensitivity is 38.8%, the specificity is 100%, and the accuracy is 69.4%. When using the individual classifier scheme, shown in the confusion matrix in Fig. 3.25, the sensitivity is 97.2%, the specificity is 97.2%, and the accuracy is 97.2%. This shows considerable improvement over the single classifier scheme. Using the group classifiers scheme from Fig. 3.32, the sensitivity is 91.6%, the specificity is 94.4%, and the accuracy is 93%. The individual classifier scheme works better than the group classifiers scheme, however, this may not be the case when a person is carrying a weapon that is not in the training data set.

Actual Class	Predicted Class	
	Non-Threat	Threat
Non-Threat	36	0
Threat	22	14

Fig. 3.30. 2x2 confusion matrix for the NNC using the single classifier scheme when *threat* data is acquired in environment 1 with *non-threat* and test data acquired in environment 2.

Actual Class	Predicted Class				
	No Weapon	Weapon 1	Weapon 2	Weapon 3	Weapon 4
No Weapon	35	0	1	0	0
Weapon 1	0	0	0	0	6
Weapon 2	0	0	3	3	6
Weapon 3	1	0	0	0	5
Weapon 4	0	1	1	0	10

(a)

Actual Class	Predicted Class	
	Non-Threat	Threat
Non-Threat	35	1
Threat	1	35

(b)

Fig. 3.31. Results for the NNC using the individual classifier scheme: (a) 5x5 confusion matrix for each individual weapon class; (b) 2x2 confusion matrix where any positive output from (a) results in a *threat* outcome. Training is done with *threat* targets from environment 1 and *non-threat* targets from environment 2. Testing is done in environment 2.

Actual Class	Predicted Class			
	No Weapon	Knife	Gun	Baton
No Weapon	34	1	1	0
Knife	1	6	3	2
Gun	2	7	2	1
Baton	0	6	0	6

(a)

Actual Class	Predicted Class	
	Non-Threat	Threat
Non-Threat	34	2
Threat	3	33

(b)

Fig. 3.32. Results for the NNC using the group classifiers scheme: (a) 5x5 confusion matrix for each weapon group class; (b) 2x2 confusion matrix where any positive output from (a) results in a *threat* outcome. Training is done with *threat* targets from environment 1 and *non-threat* targets from environment 2. Testing is done in environment 2.

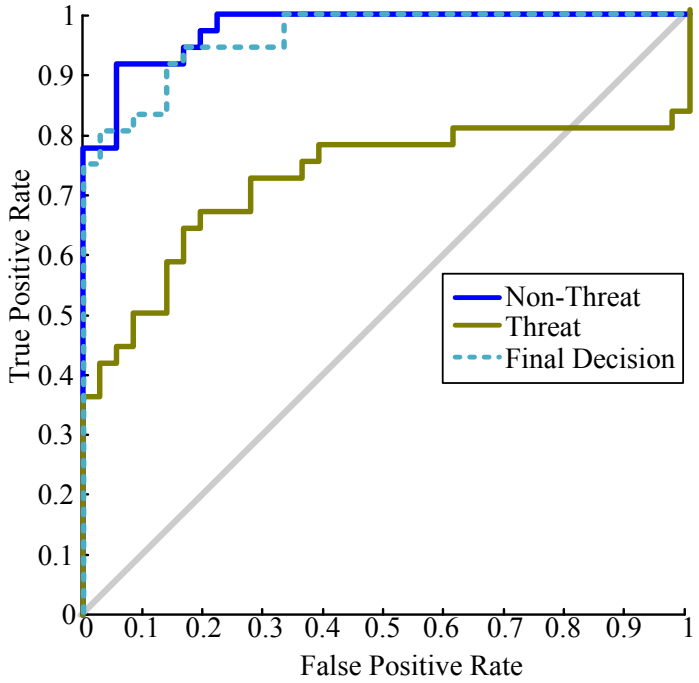

Fig. 3.33. ROC curve for the NNC when using the single classifier scheme. Training is done with *threat* targets from environment 1 and *non-threat* targets from environment 2. Testing is done in environment 2.

C) ***ROC Curves***

Fig. 3.33 shows the ROC curve when using the single classifier scheme from Fig. 3.30. There is successful classification for the *non-threat* class but the *threat* class does not perform well. However, the final decision is still good.

Using the individual classifier scheme from Fig. 3.31, the ROC curves shown in Fig. 3.34 (a) are improved compared to those in Fig. 3.28. When combining the weapon classes the ROC curves (shown in Fig. 3.34 (b)) indicate good performance for the classifier.

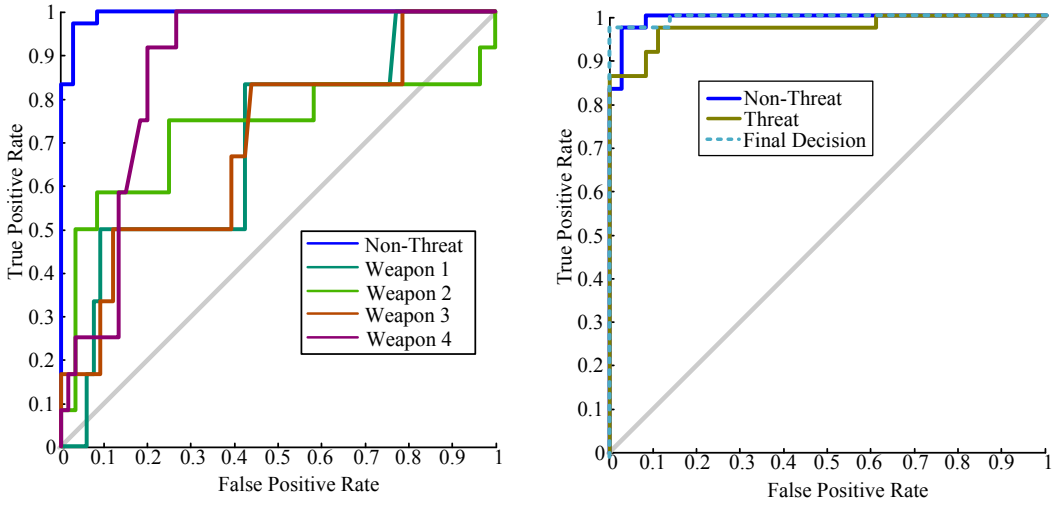

(a) (b)

Fig. 3.34. ROC curves for the NNC when using the individual classifier scheme: (a) individual weapon classifiers; (b) *threat* and *non-threat* outcome where any positive result is set to *threat* along with the final decision which is an average between the two classes. Training is done with *threat* targets from environment 1 and *non-threat* targets from environment 2. Testing is done in environment 2.

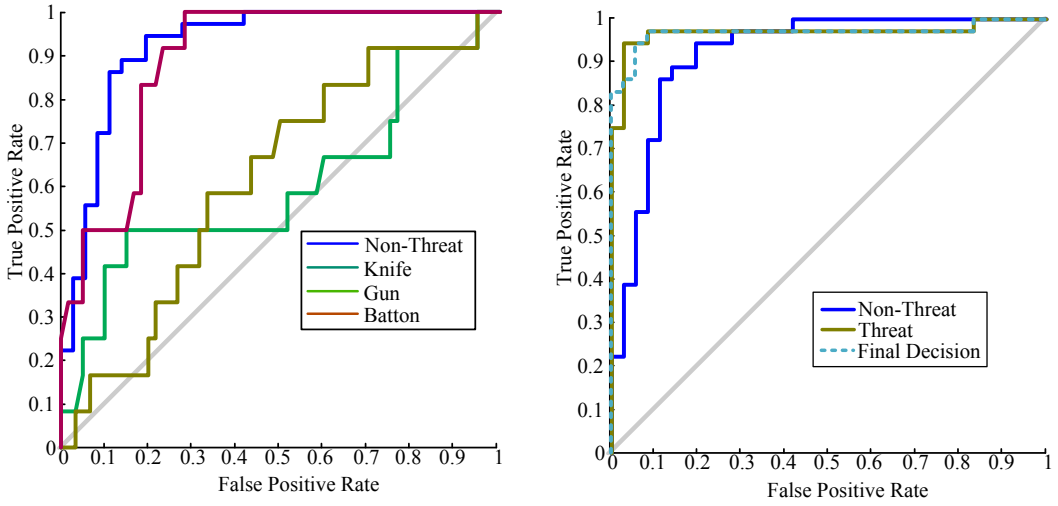

(a) (b)

Fig. 3.35. ROC curves for the NNC when using the group classifiers scheme: (a) weapon group classifiers; (b) *threat* and *non-threat* outcome where any positive result is set to *threat* along with the final decision which is an average between the two classes. Training is done with *threat* targets from environment 1 and *non-threat* targets from environment 2. Testing is done in environment 2.

Fig. 3.35 shows the ROC curves when using the group classifiers scheme from Fig. 3.32. The weapon group classes do not perform well (see Fig. 3.32 (a)), but when combined output does perform at an acceptable level (see Fig. 3.32 (b)). Note that the individual classifier scheme still outperforms the group classifiers scheme. This demonstrates that as many weapons as possible should be used in the training data.

3.5. CONCLUSIONS

An algorithm for the detection of concealed weapons in a cluttered environment has been validated through measurements with a frequency-sweep measurement setup. The algorithm relies on proper suppression of the environmental clutter through the analysis of the resonance information from the background. Once the effects of the background are removed, classification is can be performed to determine if an object is a threat or not.

The ideal classification scheme works with each individual weapon having its own class (or classifier). The outputs of these independent classifiers can then be combined to issue a *threat*/*non-threat* outcome. Although each individual weapon classifier did not perform well, the combination of the individual classifiers provided excellent results. This demonstrates that the algorithm can issue a threat/*non-threat* outcome with high performance, but cannot identify the potential weapon accurately. Improving the classification scheme give some indication of the type of threat should be the subject of future work. Additionally, the group classifiers scheme may prove to be more successful when testing with

weapons that are not in the training data set. This is a more practical scenario than having every possible weapon in the training data set.

These conclusions should be considered with the "black box" approach to classification in mind. The effects of the classification parameters have not been studied and are only used to demonstrate the effectiveness of the clutter suppression. By keeping the classification parameters the same, the improvement in the sensitivity and specificities do demonstrate that the clutter suppression technique does indeed improve the results. However, it is possible that with a different classification technique, good results may be obtained without the suppression; however this is outside the expertise of the author.

Although the training data is different from the test data, results with sensitivities and specificities of 97.2% are achieved. These results should be improved when larger training sets are utilized. This provides the framework for a functional concealed weapon detection system, However to ensure fast classification, a time domain system should be developed.

REFERENCES

[1] *Agilent E83638 PNA network analyzer (10 MHz – 40 GHz)*

[2] J.Y. Siddiqui, Y.M.M. Antar, A.P. Freundorfer, E.C. Smith, G.A. Morin, and T. Thayaparan, "Design of an ultrawideband antipodal tapered slot antenna using elliptical strip conductors," *IEEE Antennas and Wireless Propagation Letters*, vol. 10, pp. 251–254, March 2011.

[3] *Advantest R3770 Network Analyzer (300 kHz – 20 GHz)*

[4] *FT-RF Quad Ridge Horn Antenna HR-03M06G08-NF* http://www.taiwan-antenna.com/front/bin/ptdetail.phtml?Part=400MHz-6GHz-Dual-Polarization-Broadband-Horn-Antenna-N-Female-type008&Category=368755

CHAPTER 4

CONCEALED WEAPON DETECTION: TIME-DOMAIN MEASUREMENTS

Introduction

In order to move towards a concealed weapon detection system that can be used in real time, a time-domain pulse radar system must be developed. Frequency-sweep systems are simply too slow for real-time use. On the other hand, a wideband pulse is short, only a few nanoseconds, and the whole measurement can be completed on the order of a few milliseconds. A preliminary time domain system is developed and tested using an arbitrary waveform generator along with a high speed sampling oscilloscope.

4.1. MEASUREMENTS WITH TIME-DOMAIN LABORATORY PROTOTYPE

4.1.1. System Configuration

The system used in the time domain laboratory prototype consists of two dual-polarized ridge-horn antennas (see Fig. 4.1). The transmitting antenna is connected to an arbitrary waveform generator (AWG) [1] through a broadband power amplifier [2] and a broadband RF two-pole single-throw switch [3] to control the polarization of the transmitted waveform. An impulse radar system is utilized with a sine-modulated Gaussian pulse (similar to a monocycle pulse or a differentiated Gaussian pulse). The pulse generated by the AWG is shown in Fig. 4.2 and its spectrum is shown in Fig. 4.3. The pulse is created through the following formula

$$g(n) = e^{-A(n-n_0)^2} \sin(2\pi f_c T_s (n - n_0)),$$
$$A = \left(\frac{\pi (f_h - f_c) T_s}{\sqrt{\ln(10/3)}} \right)^2, \tag{2.1}$$

where f_h is the upper frequency limit (5 GHz), f_c is the center frequency (2.5 GHz), T_s is the sampling period, set by the limit of the generator to 0.05 ns, n is the sample number and n_0 is an offset.

Each port of the receiving antenna is connected to a channel on a high speed oscilloscope [4]. The arbitrary waveform generator has a differential pair output; the positive output is fed into the antenna and the negative output is fed into a channel on the oscilloscope for triggering. The oscilloscope is triggered to begin

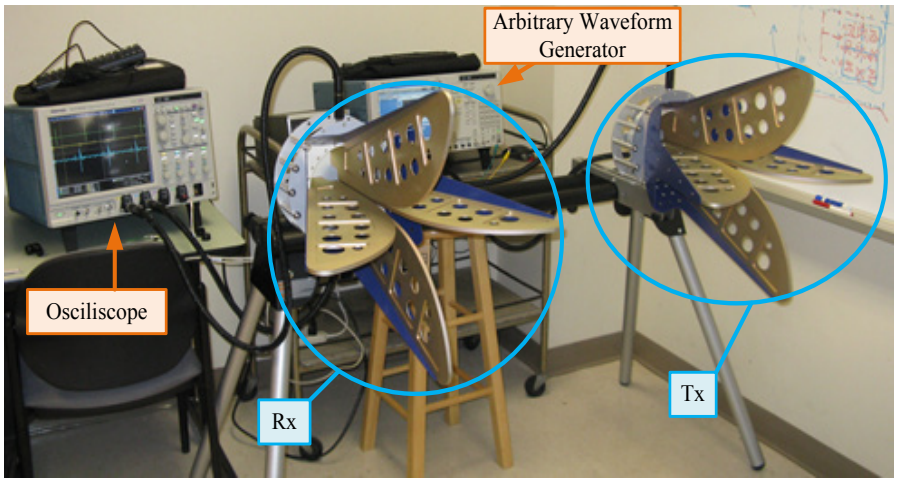

Fig. 4.1. Photo of the time domain radar setup with an arbitrary waveform generator, transmitting antenna (Tx), receiving antenna (Rx), and a high speed oscilloscope.

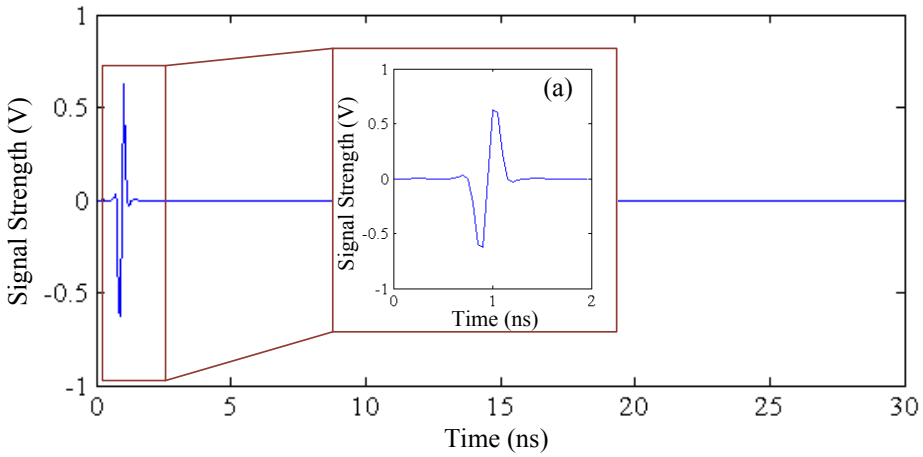

Fig. 4.2. Gaussian pulse modulated with a sine wave in the time domain. The pulse that is generated by the arbitrary waveform generator is approximately 1 ns wide. (a) Enlarged version of the pulse.

recording by the falling edge of the pulse. For each measurement, 100 averages are taken with a pulse repetition time of 50 ns to allow sufficient time for resonances to arrive at the receiver before the next pulse arrives. For a given transmitter (Tx) polarization, both co- and cross-polarized received signals are recorded simultaneously.

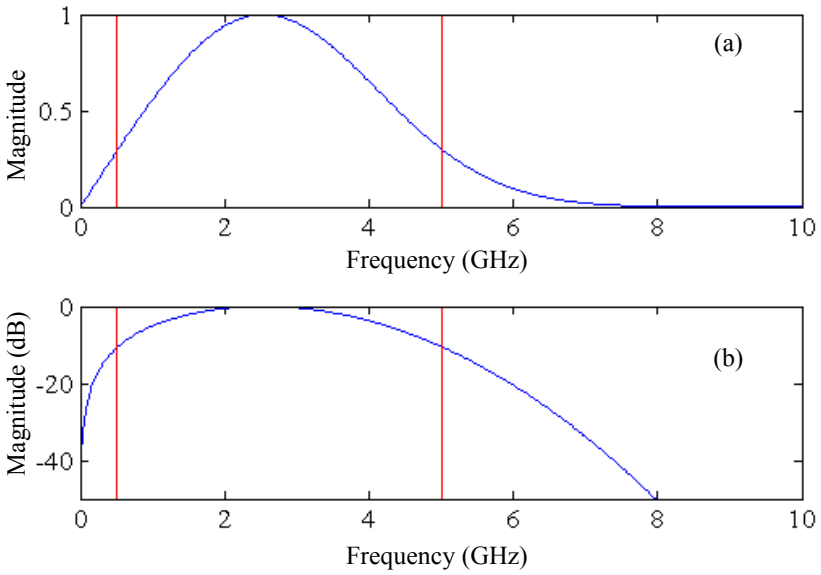

Fig. 4.3. Normalized magnitude spectrum of the Gaussian pulse modulated with a sine wave in: (a) linear scale and (b) in dB. The vertical red line denotes the pulse bandwidth. The pulse was designed to have a normalized magnitude greater than 0.3 (10 dB) over the band from 0.5 GHz to 5 GHz.

Measurements are taken in one environments as follows:

1) 10 repeated measurements of the background,
2) 5 repeated measurements of each weapon,
3) 3 repeated measurements of a person without a weapon,
4) 3 repeated measurements of a person with a weapon concealed on the front or side of their body, in an arbitrary orientation.

Measurements 2 to 4 were repeated for the targets positioned at 60 cm (near) from the antenna aperture and 120 cm (far) from the antenna aperture.

4.1.2. Targets

The targets for this measurement are the same as those in Section 3.3.3.

4.2. RESULTS WITH TIME-DOMAIN LABORATORY PROTOTYPE

With the time-domain system, a slightly different pre-processing method is used than with the frequency-sweep system. First, a fixed time window is used to exclude the mutual coupling between the antennas, shown in Fig. 4.4. Then, a dynamic time window is used to remove the initial specular reflection (early time response) from the object, shown in Fig. 4.6. This is accomplished by using a matched filter to determine where the specular reflection occurs. The waveform used in the matched filter is obtained by using a large metallic sheet to reflect the transmitted waveform back to the receiver, shown in Fig. 4.5. This waveform contains the mutual coupling along with the specular reflection with all distortions that the antennas and the equipment may cause. Note that the waveform portion due to the mutual coupling between the Tx and Rx antennas is located in a time window, which is independent of the target location. On the other hand, the specular reflection from a target (the metallic sheet included) is in a time window which depends on the distance from the antennas. In order to remove any dependence on the distance to the target, the received pulse from the metallic sheet (without mutual-coupling) is utilized in the matched filter. The mutual coupling is removed from all waveforms using the same fixed window in Fig. 4.4. The output of the matched filter shows the locations where the correlation between the response from the metallic sheet and the response from the target is high. The location (in time) where the correlation is maximum is the location of

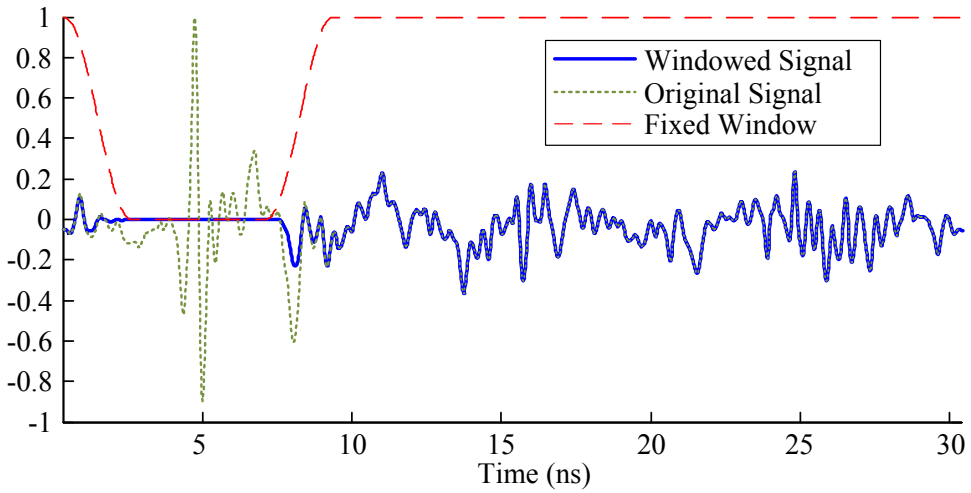

Fig. 4.4. Averaged signal from all measurements showing the signal after removing mutual coupling (blue solid line), the original signal (green dotted line) and the fixed window (red dashed line).

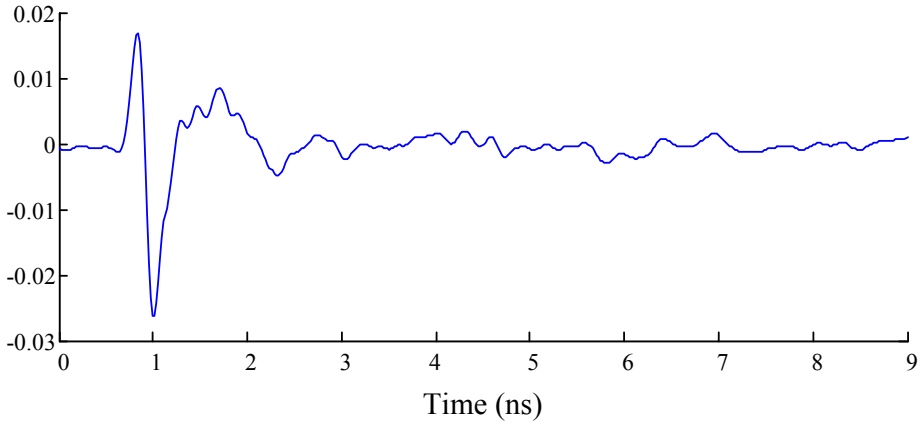

Fig. 4.5. Waveform used in the matched filter that is reflected from a large metallic sheet.

the specular reflection. To the right of this point and 3 dB down from it, the cut-off level for the window is set. The signal to the left of the maximum is the early time response (ETR) and it is removed by a window. A Tukey window [5] is used to ensure the smooth right edge of the filter (there is no left edge as it has already been removed by the fixed window). An example signal, with the dynamic window, is shown in Fig. 4.6.

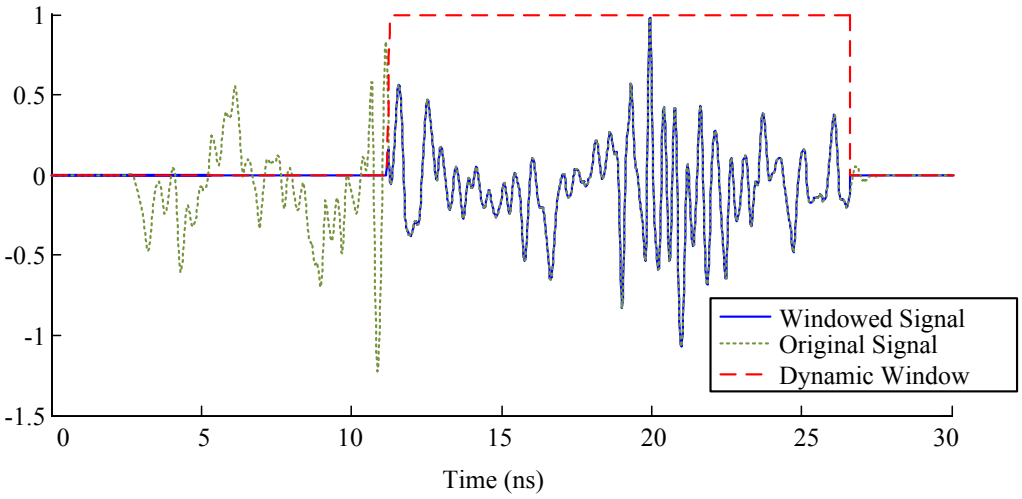

Fig. 4.6. Late time signal after removal of the specular reflection using a dynamic window. The windowed signal is in blue (solid line), the original signal is in green (dotted line) and the dynamic window is in red (dashed line).

4.2.1. Classification Schemes

The three classification schemes investigated with the time-domain system are the same as those in Section 3.2.1 and Section 3.4.1, namely the single classifier scheme, individual classifier scheme, and the group classifiers scheme.

4.2.2. Confusion Matrices

When performing classification using the single classifier scheme, the results are unsatisfactory as shown in Fig. 4.7. In this case 31 people with weapons are classified as *non-threat* with only 29 being classified correctly.

When performing classification using the individual classifier scheme, the results improve, especially when combining the data into *threat* and *non-threat* outcomes. As shown in Fig. 4.8, only 5 measurements of people with weapons (out of 60) are classified as *non-threat*. However, 8 out of 16 people without weapons are classified as *threat*, which is worse than the single classifier scheme.

In concealed weapon detection, it is more critical to reduce the number of false negatives than that of the false positives.

When using the group classifiers scheme, shown in Fig. 4.9, the number of false positives has increased, but the number of false negatives is improved over the *threat*/*non-threat* case. However, the individual classifier scheme still performs best, as expected from the frequency-sweep results.

4.2.3. Sensitivity, Specificity, & Accuracy

The confusion matrix for the single classifier scheme (Fig. 4.7) yields a sensitivity of 48.3%, a specificity of 83.3%, and an overall accuracy of 58.3%. However, when using the individual classifier scheme, from Fig. 4.8, the sensitivity has improved to 91.6%, with a specificity of 66.7% and an overall accuracy of 84.5%. When using the group classifiers scheme, from Fig. 4.9, the sensitivity is 70%, the specificity is 62.5%, and the accuracy is 67.8%. These are acceptable levels, and can be improved by having larger training datasets.

4.2.4. ROC Curves

When using the single classifier scheme, from Fig. 4.7, neither classifier performs well, as shown by the ROC curves in Fig. 4.10.

When using the individual classifier scheme, from Fig. 4.8, the ROC curve for the *non-threat* class are acceptable, as shown in Fig. 4.11(a). However, like frequency-sweep measurements, each individual weapon class alone does not perform well. Fig. 4.11 (b) shows the ROC curves with the combined *threat* class and indicated acceptable performance for the classifier.

Actual Class	Predicted Class	
	Non-Threat	Threat
Non-Threat	20	4
Threat	31	29

Fig. 4.7. 2x2 confusion matrix for the NNC using the single classifier scheme

Actual Class	Predicted Class				
	No Weapon	Weapon 1	Weapon 2	Weapon 3	Weapon 4
No Weapon	16	0	3	2	3
Weapon 1	0	0	5	5	8
Weapon 2	2	1	4	3	8
Weapon 3	0	1	6	3	2
Weapon 4	3	0	2	0	7

(a)

Actual Class	Predicted Class	
	Non-Threat	Threat
Non-Threat	16	8
Threat	5	55

(b)

Fig. 4.8. Results for the NNC using the individual classifier scheme: (a) 5x5 confusion matrix for each individual weapon class; (b) 2x2 confusion matrix where any positive output from (a) results in a *threat* outcome.

Actual Class	Predicted Class			
	No Weapon	Knife	Gun	Baton
No Weapon	15	3	5	1
Knife	8	9	1	12
Gun	6	5	2	5
Baton	4	1	0	7

(a)

Actual Class	Predicted Class	
	Non-Threat	Threat
Non-Threat	15	9
Threat	18	42

(b)

Fig. 4.9. Results for the NNC using the individual classifier scheme: (a) 4x4 confusion matrix for each weapon group; (b) 2x2 confusion matrix where any positive output from (a) results in a *threat* outcome.

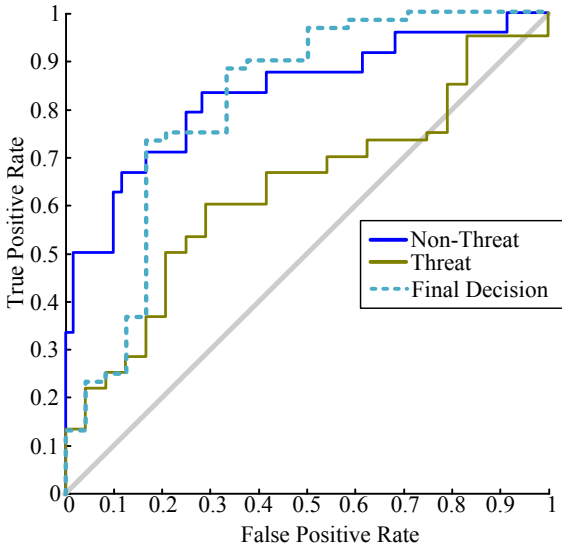

Fig. 4.10. ROC curve for the NNC when using the single classifier scheme.

When using the group classifiers scheme from Fig. 4.9, each individual classifier performs at an adequate, but not exceptional level, which can be seen by the ROC curves in Fig. 4.12 (a). When combining the outcomes into *threat* and *non-threat* classes (Fig. 4.12 (b)), the results are good, but not as good as when using the individual classifier scheme from Fig. 4.11. Overall, the time domain system performs well with a fast acquisition time, although the separation of the ETR and LTR may be improved through future work.

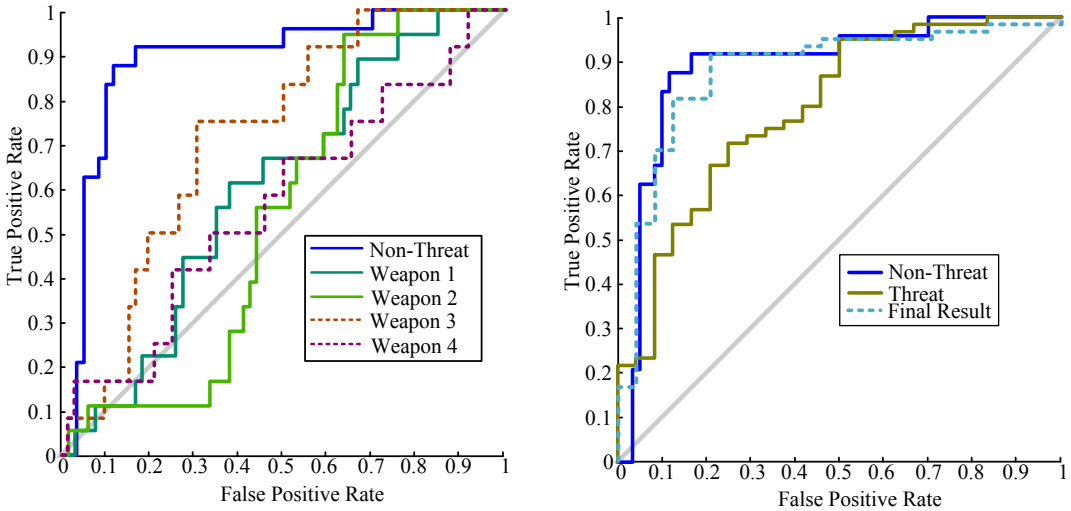

(a) (b)

Fig. 4.11. ROC curves for the NNC when using the individual classifier scheme: (a) individual weapon classifiers; (b) *threat* and *non-threat* outcome where any positive result is set to *threat* along with the final decision which is an average between the two classes.

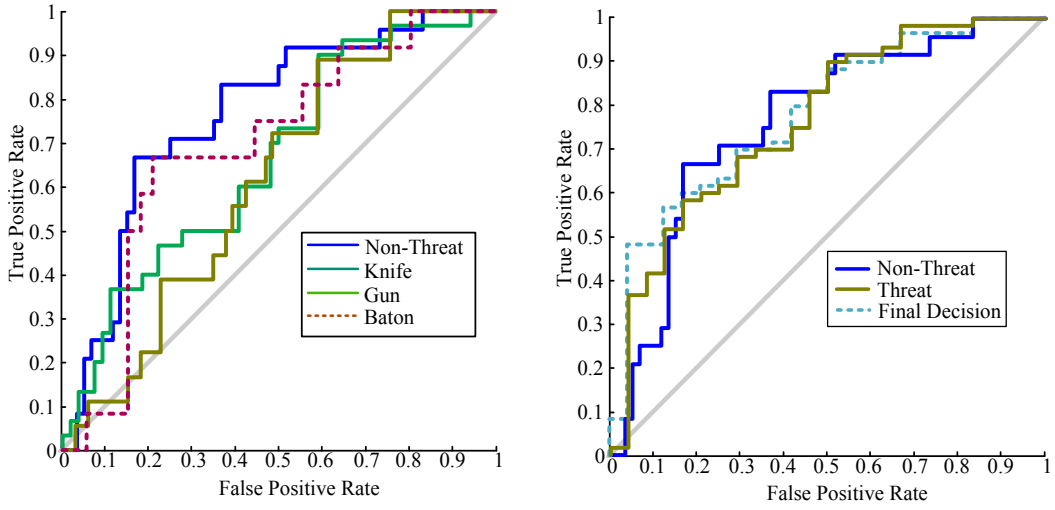

(a) (b)

Fig. 4.12. ROC curves for the NNC when using the group classifiers scheme: (a) weapon group classifiers; (b) *threat* and *non-threat* outcome where any positive result is set to *threat* along with the final decision which is an average between the two classes.

4.3. CONCLUSIONS

The algorithm for the detection of concealed weapons based on late time responses developed in Chapter 3 is extended to work with a time domain system. This system is developed using laboratory equipment, but the fundamentals of the algorithm can be extended to a custom radar system to enable fast detection. Measurements are performed in a single background to evaluate the algorithms performance on direct time-domain data. Sensitivities up to 91% and specificities up to 66% percent were achieved using a limited amount of data. With a larger training and test sets, these values are expected to improve. A larger training set coupled with the ability to perform fast detection will enable multiple measurements on a single individual which will also improve the likelihood that a concealed weapon is detected. The development of an in-house fast radar system is one of the areas of future work.

Again, these conclusions should be considered with the "black box" approach to classification in mind. It is entirely possible that different results could be obtained by modifying the classification method.

REFERENCES

[1] *Tektronix AWG7102 10GS/s,* http://www.tek.com/datasheet/awg7000-series

[2] *SHF 100BP 30kHz-25GHz,* https://www.shf.de/fileadmin/download/100bp.pdf

[3] *General Microwave model 1699 0.1-20 GHz*

[4] *Tektronix DSA72004B 50GS/s,* http://www.tek.com/oscilloscope/dpo70000-mso70000

[5] F.J. Harris, "On the use of windows for harmonic analysis with the discrete Fourier transform," *Proc. IEEE*, vol. 66, no. 1, pp. 51–83, Jan. 1978

CHAPTER 5

SIGNAL-TO-NOISE RATIO ASSESSMENT OF *S*-PARAMETER ACQUISITION FOR MICROWAVE IMAGING

Introduction

Currently, there is no agreed upon metrics and methods to assess and quantify the signal-to-noise ratio (SNR) of the data acquired for the purposes of microwave imaging in applications such as near-field tissue imaging, concealed weapon detection, and non-destructive testing of materials. Here, we are concerned with the so-called raw data, such as the scattering parameters, before the stage of signal processing for image reconstruction. The method is not intended to evaluate the performance of reconstruction algorithms but to assess the system SNR at the hardware level. This would be useful to compare acquisition hardware, discriminate between low- and high-quality data sets, and choose the appropriate image processing algorithms depending on the data quality.

5.1. Sources of Noise and Uncertainty in *S*-Parameter Acquisition

Noise and uncertainty are unavoidable in any measurement. This section provides an overview of the sources of errors in *S*-parameter acquisition systems used in imaging. It is important to understand the sources of error in order to improve the noise level of an acquisition system.

5.1.1. Systematic Errors

Systematic errors occur when the mean value of many successive measurements differ from the actual value that should be obtained. All measurements are prone to systematic errors, which can be due to various sources. For example, in a vector network analyzer (VNA), systematic errors may be caused by imperfect switching, cross-coupling between channels, non-ideal directional couplers, etc. Systematic errors are errors which can be relatively easily modeled and corrected. In a VNA, this correction is done through calibration, with a known error model. In this case, measurements are made of known devices, i.e., standard loads, of which the actual response is known. Then these measurements are used to fit an error model, which compensates for the difference between the actual response and the measured response.

In *S*-parameter acquisition systems, the VNA is typically calibrated to the end of the cables, which, ideally, compensates for all errors associated with the VNA, the cables, and the connectors. The remaining systematic errors are caused by the acquisition hardware, namely, the antennas and the scanning system (if

using mechanical scanning). Losses and reflections internal to the antenna, or between the antenna and the scanning system, cross-coupling between antenna array elements, and leakage between the transmitter and receiver are all examples of systematic errors that can occur in a *S*-parameter acquisition system. Correcting these errors remains a topic of interest in the microwave imaging community. Many systematic errors internal to the antennas are very hard to model, often requiring full-wave electromagnetic simulations.

For example, in [1], a method of compensating the mutual-coupling and poor isolation between array elements in a microwave image camera is proposed. This method makes use of a correlation canceller [2] to fit their model,

$$\boldsymbol{x} = \boldsymbol{SCy} + \boldsymbol{b}, \tag{5.1}$$

where $\boldsymbol{x}$ is the measured signal, $\boldsymbol{S}$ and $\boldsymbol{C}$ are a scaling and coupling matrix, respectively, $\boldsymbol{y}$ is the ideal signal, and $\boldsymbol{b}$ is a static offset. This approach requires knowledge of what the 'ideal' signal is, which in many cases is hard to determine as it must include systematic errors not due to the cross-coupling.

5.1.2. Random Errors

Random errors are impossible to compensate for and are unavoidable in any measurement. For example, in a VNA, random errors can be caused by jitter in the generator and receiver. Typically, these errors are compensated by averaging and lowering the resolution bandwidth of the receiver. However, in real systems, a low resolution bandwidth and a high number of averages is impossible as they often lead to an unacceptably long acquisition time.

In *S*-parameter acquisition systems, the random errors can be divided into two categories, internal and external errors. Internal errors are intrinsic to the acquisition system. For example, these errors can be caused by electronic noise internal to the VNA, noise introduced by the antennas, amplifiers, switches, and uncertainty errors due to positioning mechanism, wire connections, etc. External errors are caused by factors external to the acquisition system, for example, errors caused by temperature variations (electrical properties are known to be temperature dependent) or electromagnetic interference from other radiation sources, such as communication networks, motors, etc. We can have some control over the amount of error, or noise, introduced by the internal errors, by carefully selecting the components that we use. For example, if we find that an amplifier is introducing significant noise, we can replace it with an amplifier with a lower noise figure.

A method of evaluating the SNR of an *S*-parameter acquisition system is needed in order to evaluate how much noise is present in a given system. To compare the effect of the VNA parameters and other hardware, such as amplifiers, on the noise level of the system. As with all systems, the noise level is important, however, the most critical parameter is the ratio between the signal strength and the noise. Mainly, a higher noise level can be compensated by having stronger signals. In near-field tissue imaging, for example, the 'signals' arise from scatterers (inhomogeneities) in the medium being imaged. These scatterers cause changes in the signal strength and phase that can be used to generate images. The

larger this difference is, the better the SNR id, however, these scatterers are typically weak, which means that the change in signal strength is not very high. This in turn leads to the errors and noise having a large impact on the quality of the data. For this reason, the SNR is advantageous in discriminating between low- and high-quality data sets, and choosing the appropriate image processing method. In this definition, the SNR is frequency dependent as it is evaluated in a raw data 'image' at a particular frequency point.

5.2. SNR EVALUATION METHODS

There are two main quality assurance metrics known from the analysis of the raw images in magnetic resonance imaging (MRI). These are the signal-to-noise ratio (SNR) [3]–[6] and the contrast-to-noise ratio (CNR) [7]. These metrics are designed for use with real-valued data and are not directly applicable with the complex *S*-parameter data used in microwave imaging. The delimitations of the image SNR and CNR are:

$$\text{SNR}=\frac{\text{average(ROI)}}{\text{std dev(B)}}, \tag{5.2}$$

$$\text{CNR}=\frac{\text{average(ROI)-average(B)}}{\text{std dev(B)}}. \tag{5.3}$$

In both (5.2) and (5.3), a region of interest, ROI, and a background region, B, are defined. The region of interest is taken as the area in which the signal strength is evaluated. The background region is an area where no signals are expected (the feature-free region).

Depending on how ROI and B are defined in (5.2) and (5.3), there are two formulations: one that requires only one data set to evaluate the background noise and the signal strength (single image formulation) and one that uses two datasets, from which the background noise and signal strength are evaluated separately (dual image formulation).

Both the dual and single image formulations will work with the data used in microwave imaging where a calibration step is not performed. However, it is common practice to subtract a measurement of a reference object (RO), which has no scatterers, from a measurement of an object under test (OUT), which may contain scatterers. This is due to the fact that most imaging algorithms need the scattered field, $\mathbf{E}^s$, which is the field due to the scatterers. The measurement of the RO should ideally provide the incident field, $\mathbf{E}^i$, and the measurement of the OUT provides the total field, $\mathbf{E}^t$, which is the superposition of the incident field and the scattered field (i.e. $\mathbf{E}^t = \mathbf{E}^i + \mathbf{E}^s$). Because we perform this calibration step on the raw data, it is best if the SNR is evaluated on this calibrated image as that is the raw data submitted to the reconstruction algorithms. Since we subtract the RO from the measurements, the dual image formulation will require an additional RO measurement so that the noise may be evaluated from the difference between the two RO measurements. This is not practical because we would like to evaluate the SNR without introducing more measurements. Additionally, because we are subtracting the RO measurement, the mean value of

the background region should be zero. In this case, the SNR and CNR are equivalent. Therefore, we will work with only the SNR.

Further, in order to better quantify the SNR result, it is best to work with a known test object, referred to as a calibration object (CO) instead of any OUT because the contrast distribution is known. Moreover, a number of recent imaging techniques use CO measurements to calibrate the system and improve the images [8][9]. Thus, the data necessary to perform the system SNR assessment is readily available.

5.2.1. Single Image Formulation

The single image formulation can be written as

$$\text{SNR}=\frac{\text{average}(\Delta S(\vec{\mathbf{r}}_{\text{ROI}}))}{\text{std dev}(\Delta S(\vec{\mathbf{r}}_{\text{B}}))}, \tag{5.4}$$

where $\Delta S = S^{\text{OUT}} - S^{\text{RO}}$ and $\vec{\mathbf{r}}_{\text{ROI}}$ corresponds to the area where the target is present and $\vec{\mathbf{r}}_{\text{B}}$ is the largest region in ΔS where the target is not 'seen' by the antenna aperture.

Fig. 5.1 shows the ROI (cross-hatched) and B (hatched) regions overlaid with a sample raw data image from a CO measurement. The unhatched region is an exclusion zone, where the antenna aperture contains the scatterer's lateral position while performing the scan. This image was obtained using a frequency-sweep planar raster scanning setup described in [10].

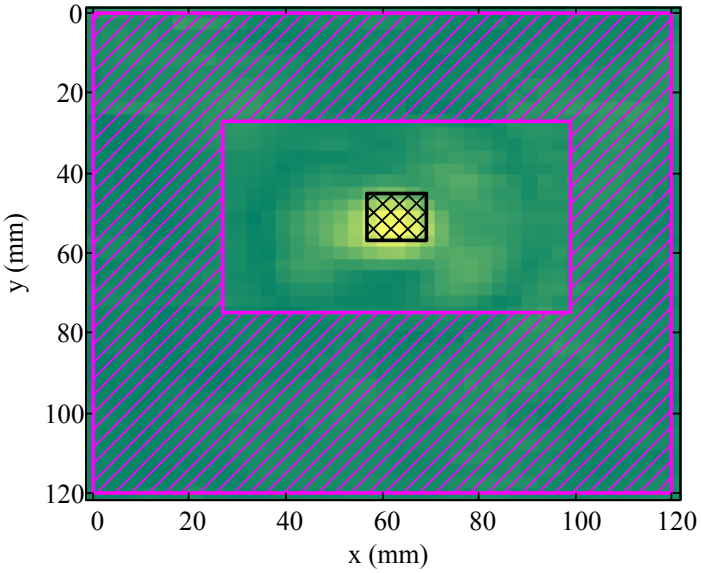

Fig. 5.1. A sample magnitude image of ΔS at 5.59 GHz showing the ROI (black cross-hatched region) as well as the exclusion area (unhatched) and the background region B (magenta hatched region).

5.2.2. Complex-Valued Formulation

One way to calculate the SNR for complex-valued data is to compute the SNR of the real and imaginary parts separately, resulting in a complex SNR. However, it is preferable to have a real-valued SNR that represents the complex-valued datasets. To do this, we define a complex-average magnitude as

$$\text{average}(\boldsymbol{D}) = \left| \frac{1}{N} \sum_{i=1}^{N} d_i \right|, \tag{5.5}$$

and the standard deviation as

$$\text{std dev}\,(\boldsymbol{D}) = \left(\frac{1}{N-1} \sum_{i=1}^{N} \left| d_i - \bar{d} \right|^2 \right)^{\frac{1}{2}}, \; \bar{d} = \frac{1}{N} \sum_{i=1}^{N} d_i, \tag{5.6}$$

where $\boldsymbol{D}$ is any vectorized complex data set. The SNR is then defined as:

$$\text{SNR} = \frac{\text{average}(\boldsymbol{D}_{\text{ROI}})}{\text{std dev}(\boldsymbol{D}_{\text{B}})}, \tag{5.7}$$

where B denotes the feature-free region (background) and ROI is the region where a known scattering object truly exists.

5.2.3. Peak Signal-to-Noise Ratio

Based on our observations, some slight modifications to the SNR formulation may yield a more accurate description of the measurement. To illustrate these differences we work with the complex-valued formulation. First, we observe that the signal from the target may shift slightly in space as the frequency changes. This is mainly due to changes in the antennas near-field pattern. In order to establish the signal level when the target shifts with frequency, the maximum signal level in the ROI can be used rather than taking the average to define the peak signal-to-noise ratio (PSNR):

$$\text{PSNR} = \frac{\left|\max\left(\boldsymbol{D}_{\text{ROI}}\right)\right|}{\text{std dev}(\boldsymbol{D}_{\text{B}})}. \tag{5.8}$$

5.3. VERIFICATION EXAMPLE

To verify the algorithm we analyze the SNR of a CO measurement used in [9]. This measurement was taken using a planar raster scanning setup developed in [10].

5.3.1. Data Acquisition System

In planar raster scanning, two antennas co-located in x and y and separated in z by a distance D, are scanned in a raster manner in the XY plane, as shown in

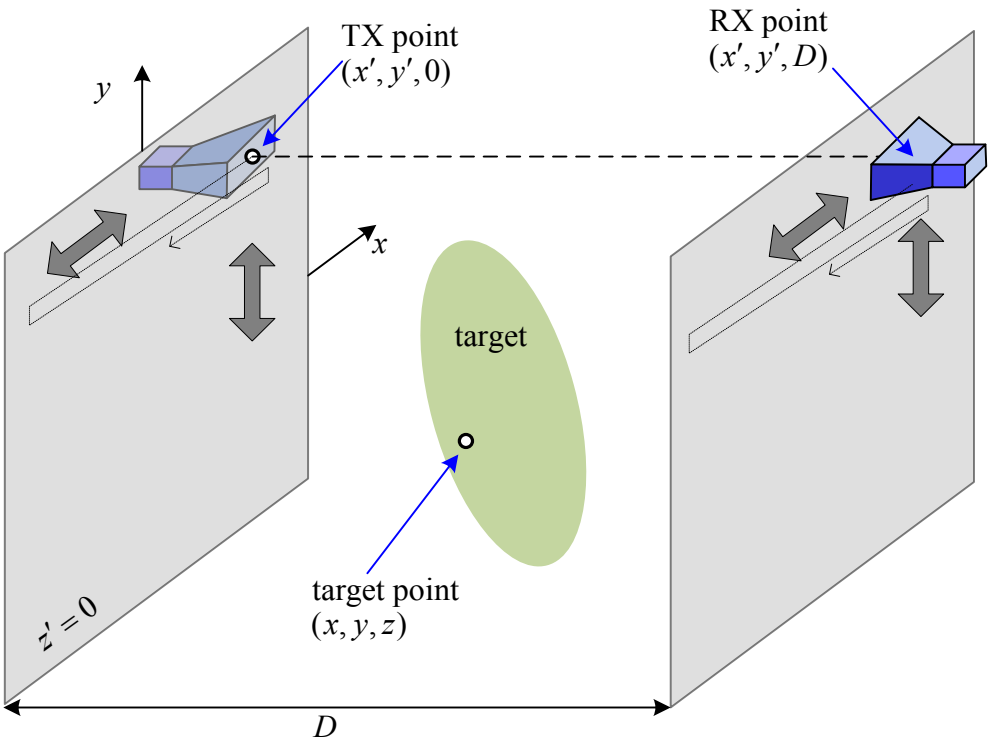

Fig. 5.2. Planar scanning acquisition setup with two-antennas.

Fig. 5.2. The *S*-parameters, acquired with a VNA, are recorded at discrete (x,y) locations and stored to create the raw-data image. The scanning system and the VNA are controlled both controlled through a computer [10].

5.3.2. Measurement Description

In this measurement, the receiver (Rx) antenna array consists of a 9 bowtie elements (Fig. 5.3 [9], Fig. 5.4 [9],). The transmitting (Tx) antenna is a horn antenna proposed in [11] (Fig. 5.5 [11]). The antennas are scanned over a 120 mm x 120 mm aperture with a spatial sampling step of 3 mm. The data is acquired from 3 GHz to 10 GHz with 101 frequency samples. A RF switch and

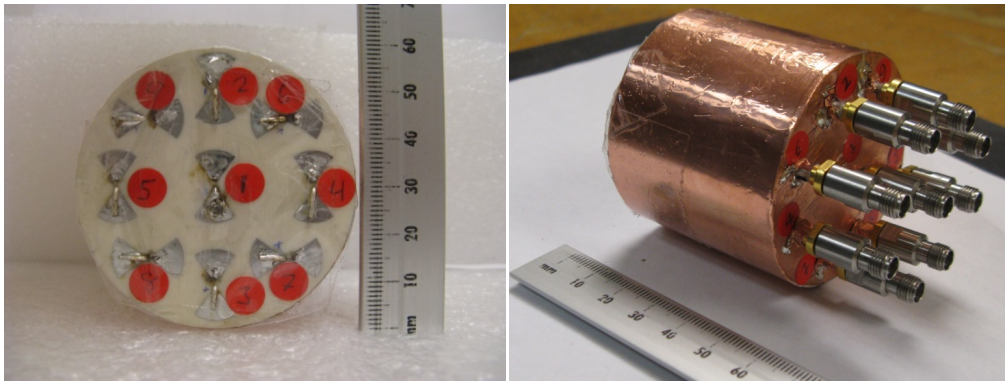

(a) (b)

Fig. 5.3. Fabricated bow-tie array: (a) front surface (facing the tissue phantom), and (b) back view showing the coaxial connectors. Reproduced from [9].

VNA are used to measure the five transmission *S*-parameters at each sampling position corresponding to the 5 co-polarized Rx bowtie elements. A 5 cm thick custom made tissue phantom with $\varepsilon_r \approx 10$ and $\tan\delta \approx 0.5$ is measured. To support the phantom for scanning, it is placed on a 5 mm thick PCB substrate (Taconic CER 10 , $\varepsilon_r = 10$ and $\tan\delta = 0.0035$). There is also an air gap of approximately 1 mm between each antenna and the phantom surface to prevent friction. The dielectric properties of the tissue phantom as well as those of the substrate are practically frequency independent in the band of the measurement. The imaging system with the VNA and the antennas is shown in Fig. 5.6.

The CO is a cylindrical dielectric resonator ($\varepsilon_r = 50$, $\tan\delta \approx 0.001$), with a diameter of 10 mm and height of 10 mm that is embedded in the centre of the tissue phantom, as shown in Fig. 5.7 [9]. The image of the CO when it is at a *z* location of 20 mm will be used to verify the SNR evaluation approach.

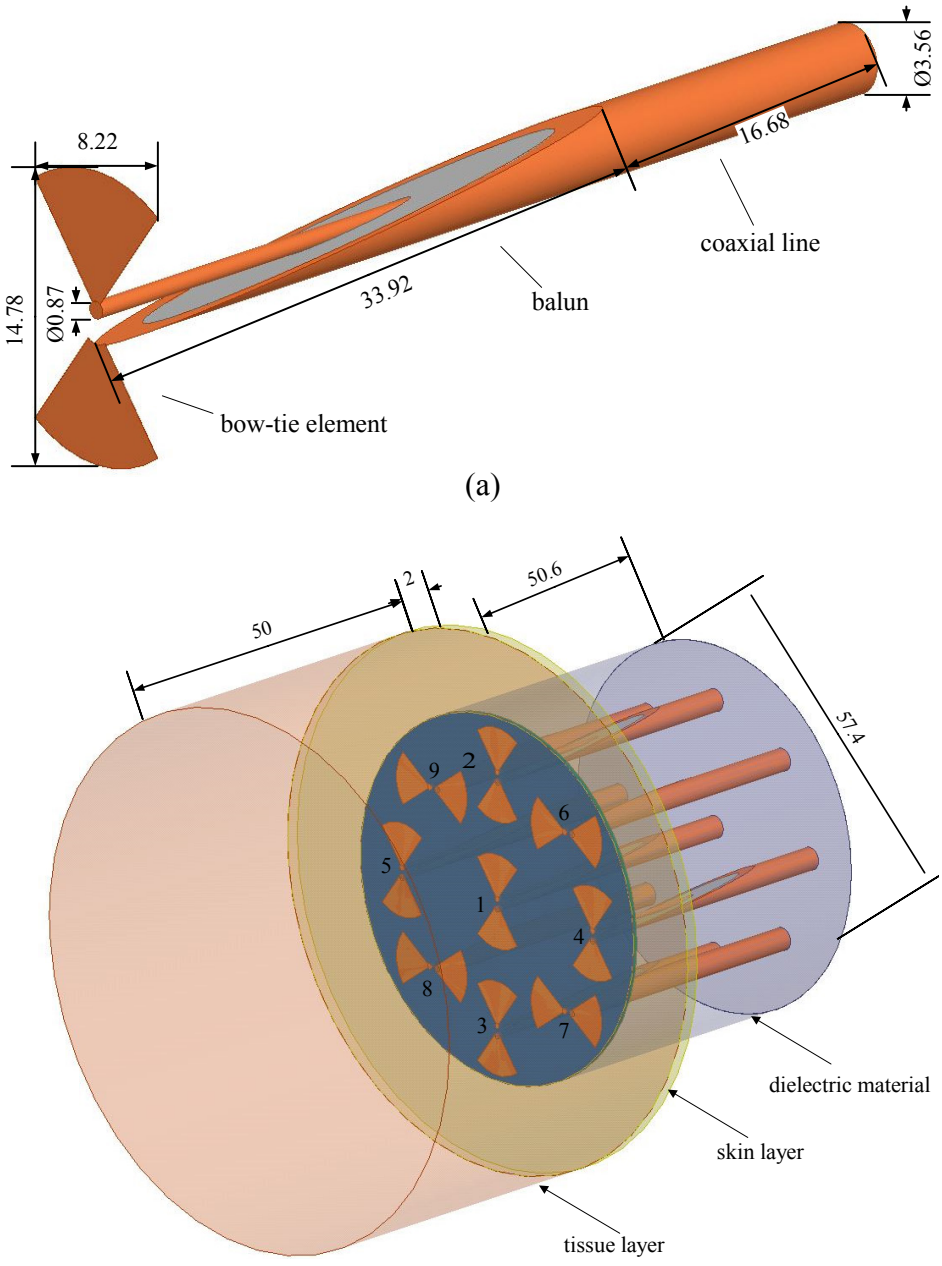

Fig. 5.4. Simulation setup in HFSS for the array of bow-tie antennas: (a) a single bow-tie element fed by a coaxial line via a balun, and (b) complete simulation setup consisting of nine bow-tie elements in co- and cross-polarized configurations, a skin layer, and a tissue layer. All dimensions are in mm. Reproduced from [9].

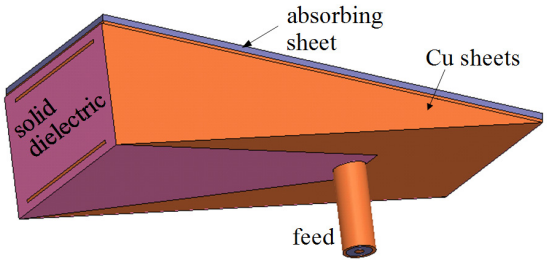

Fig. 5.5. Simulation model of the TEM horn antenna used as a transmitter. Reproduced from [11].

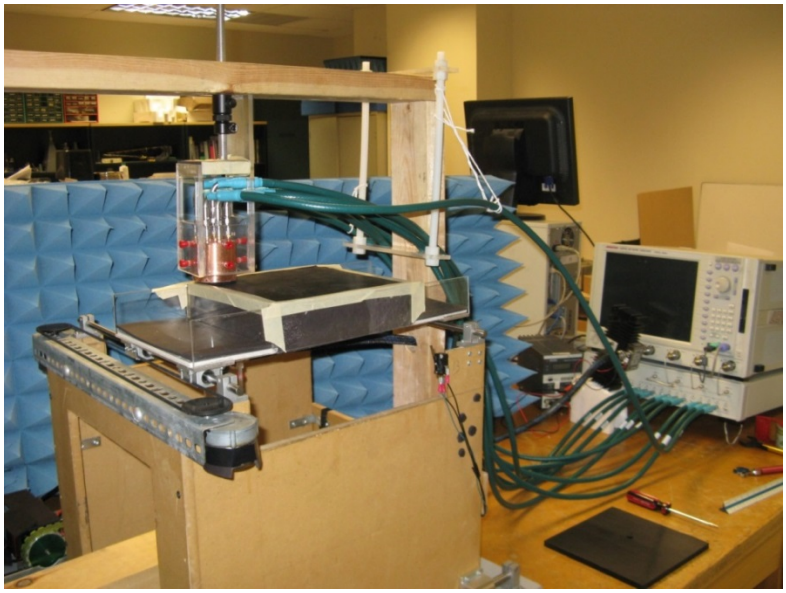

Fig. 5.6. A photo of the raster-scanning setup with the 9-element bowtie array. The transmitting TEM horn faces the bowtie array along boresight.

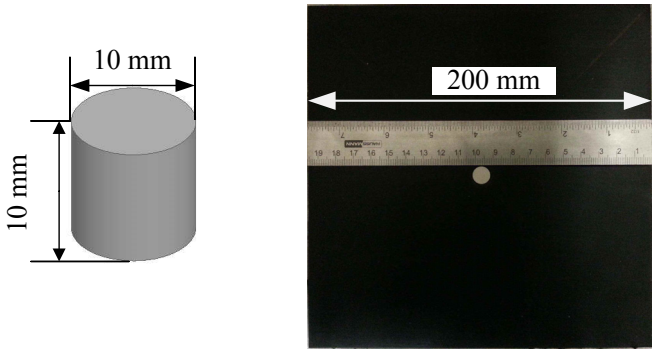

Fig. 5.7. Diagram of the cylindrical dielectric resonator used as CO in the experiments with tissue phantoms and photo of the resonator embedded in a 200 mm x 200 mm layer of phantom material. Reproduced from [9].

A power amplifier is used on the transmitting side to increase the signal strength. This amplifier has a bandwidth of 2 GHz to 8 GHz with 30 dB gain. Beyond 8 GHz, the gain decreases significantly and the signal strength from the transmitter is much weaker. Therefore, the measured signals from 8 GHz to 10 GHz should exhibit a low SNR. This is used as a reference when observing the frequency trend of the evaluated SNR.

5.3.3. Real-Valued Single Image Formulation

When processing the data using the real-valued SNR formulation, we can break up the complex data into two real parts: magnitude and phase or real and imaginary. This will give two SNR values, the SNR in the magnitude image & the SNR in the phase image; or the SNR in the real image & the SNR in the imaginary image. Both approaches are be applied to the measurement described above with the single image formulation in (5.4).

A) ***Processing by Magnitude and Phase***

When processing by magnitude and phase the two SNR's become

$$\mathrm{SNR}^{\mathrm{Mag}} = \frac{\mathrm{average}\left(\left|\Delta S(\vec{\mathbf{r}}_{\mathrm{ROI}})\right|\right)}{\mathrm{std\ dev}\left(\left|\Delta S(\vec{\mathbf{r}}_{\mathrm{B}})\right|\right)}, \tag{5.9}$$

$$\mathrm{SNR}^{\mathrm{Phase}} = \frac{\mathrm{average}\left(\angle\Delta S(\vec{\mathbf{r}}_{\mathrm{ROI}})\right)}{\mathrm{std\ dev}\left(\angle\Delta S(\vec{\mathbf{r}}_{\mathrm{B}})\right)}. \tag{5.10}$$

Fig. 5.8 (a) and (b) show the expected trend of low SNR above 8 GHz. The noise in the magnitude is much lower than that of the phase. Fig. 5.9 (a) shows the

image of $|\Delta S|$ associated with maximum SNR^{Mag} and Fig. 5.9 (b) shows the image of $|\Delta S|$ associated with minimum SNR^{Mag}. The image with the highest SNR shows a clear peak with relatively little noise. The image of the lowest SNR shows no peak and almost pure noise.

Fig. 5.9 (c) shows the image of $\angle \Delta S$ associated with the maximum $\text{SNR}^{\text{Phase}}$ and Fig. 5.9 (d) shows the image of $\angle \Delta S$ associated with the minimum $\text{SNR}^{\text{Phase}}$. We again see a peak in the image associated with the maximum SNR; however, this peak is not very sharp and there is some noise towards the left side. The minimum SNR image shows high amount of noise as well some of the target signature. The images match the trends shown in Fig. 5.8 and show that the magnitude has a higher SNR than the phase. The magnitude images exhibit the trend of having lower SNR values above 8 GHz. The phase images also show a decrease in SNR above 8 GHz but have some frequency points that have much lower SNR than those above 8 GHz. This would suggest that this method is accurate for evaluating the SNR in the magnitude of the complex *S*-parameter data but not in the phase.

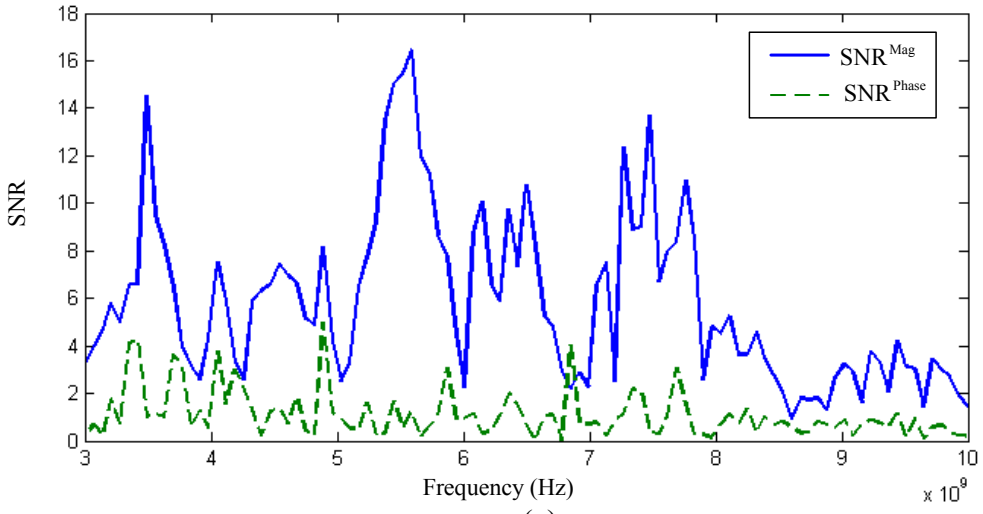

(a)

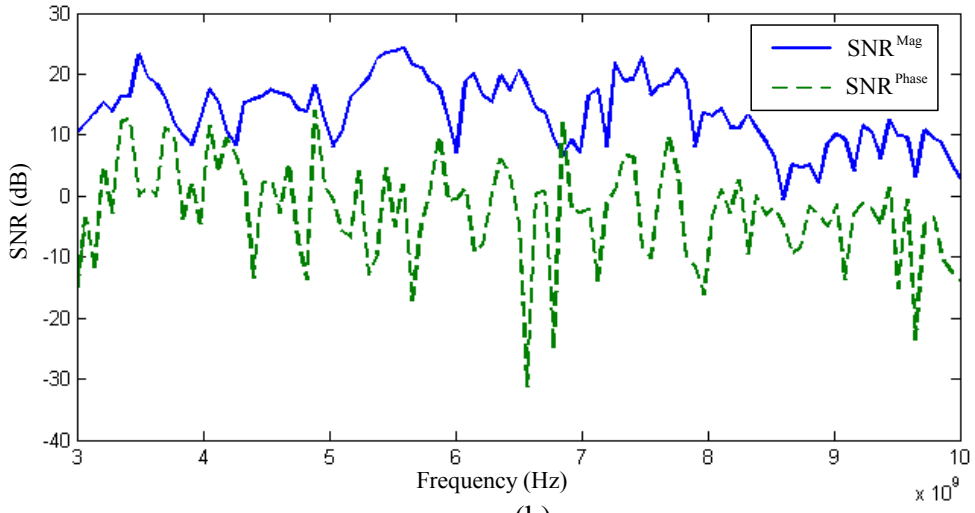

(b)

Fig. 5.8. Magnitude SNR and phase SNR processed using (5.9) and (5.10), respectively, in: (a) a linear scale, and (b) dB.

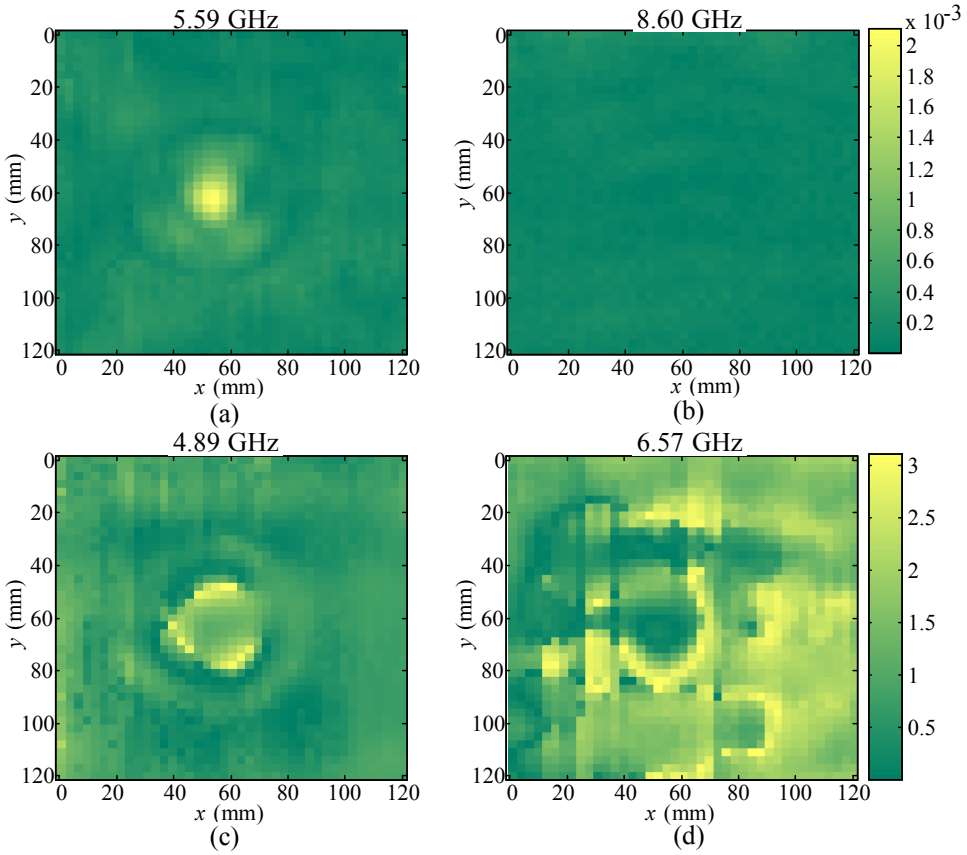

Fig. 5.9. Magnitude *S*-parameter image at the frequency associated with: (a) maximum $\mathrm{SNR}^{\mathrm{Mag}}$ and (b) minimum $\mathrm{SNR}^{\mathrm{Mag}}$. Phase image in radians at the frequency associated with: (c) maximum $\mathrm{SNR}^{\mathrm{Phase}}$ and (d) minimum $\mathrm{SNR}^{\mathrm{Phase}}$. The standard deviation of the feature free region in the magnitude at 8.6 GHz is $5.3\text{x}10^{-5}$ and in the phase at 6.57 GHz is 1.42 radians.

*B) **Processing by Real & Imaginary Parts***

When processing by real and imaginary parts, the two SNRs become

$$\mathrm{SNR}^{\Re} = \frac{\text{average}\left(\Re\left(\Delta S(\vec{\mathbf{r}}_{\mathrm{ROI}})\right)\right)}{\text{std dev}\left(\Re\left(\Delta S(\vec{\mathbf{r}}_{\mathrm{B}})\right)\right)}, \tag{5.11}$$

$$\mathrm{SNR}^{\Im} = \frac{\text{average}\left(\Im\left(\Delta S(\vec{\mathbf{r}}_{\mathrm{ROI}})\right)\right)}{\text{std dev}\left(\Im\left(\Delta S(\vec{\mathbf{r}}_{\mathrm{B}})\right)\right)}. \tag{5.12}$$

Fig. 5.10 (a) and (b) shows the expected trend in SNR which is lower at frequencies above 8 GHz. It also shows that the noise level in the real and imaginary parts of the data is similar.

Fig. 5.11 (a) shows the image of the real part of the data associated with maximum $SNR_{\Re}$. This image shows a distinct peak with only a small amount of noise around the edges. The spread of the object is also quite significant in this case. Fig. 5.11 (b) shows the image of the real part of the data associated with the minimum $SNR_{\Re}$. This image shows no distinguishable peak and is almost pure noise. Also, it is at a frequency above 8 GHz which is as expected. Fig. 5.11 (c) shows the image of the imaginary part of the data associated with the maximum $SNR_{\Im}$. This image is quite noisy, but shows a distinct peak that is much lower than the mean signal level of the image. This target is also surrounded by a halo which is in the exclusion zone of the measurement and does not affect the calculated SNR. Fig. 5.11 (d) shows the image of the imaginary part of the data associated with the minimum $SNR_{\Im}$. This image shows the target and is not in the expected range of low SNR. This is due to the fact that the signal strength where the target is present is at almost the same value as the feature-free region. The reason the target is detectable is due to the halo, which was excluded from the calculation by the exclusion zone giving the image the lowest SNR. Although this data is now associated with a low SNR value, it still contains information that could be useful to the reconstruction algorithms.

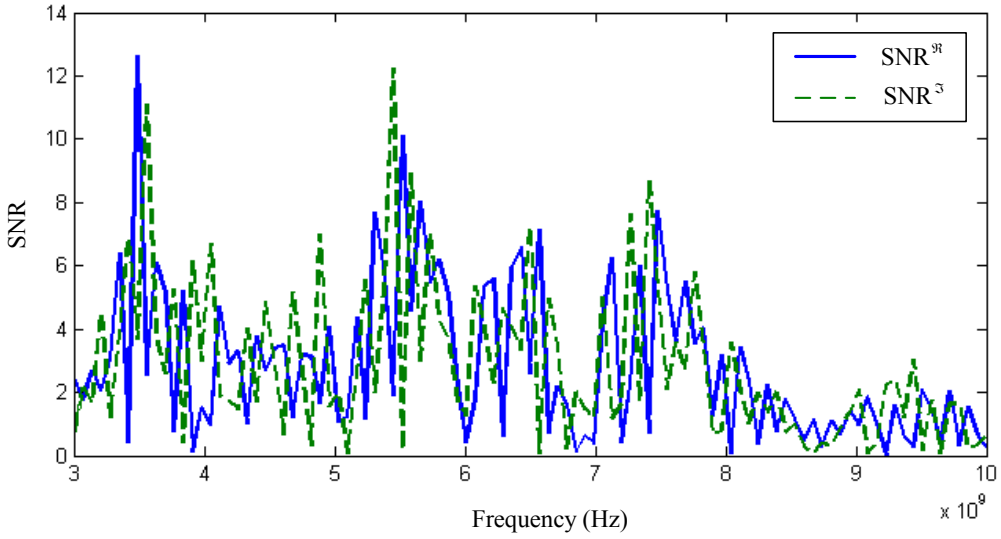

(a)

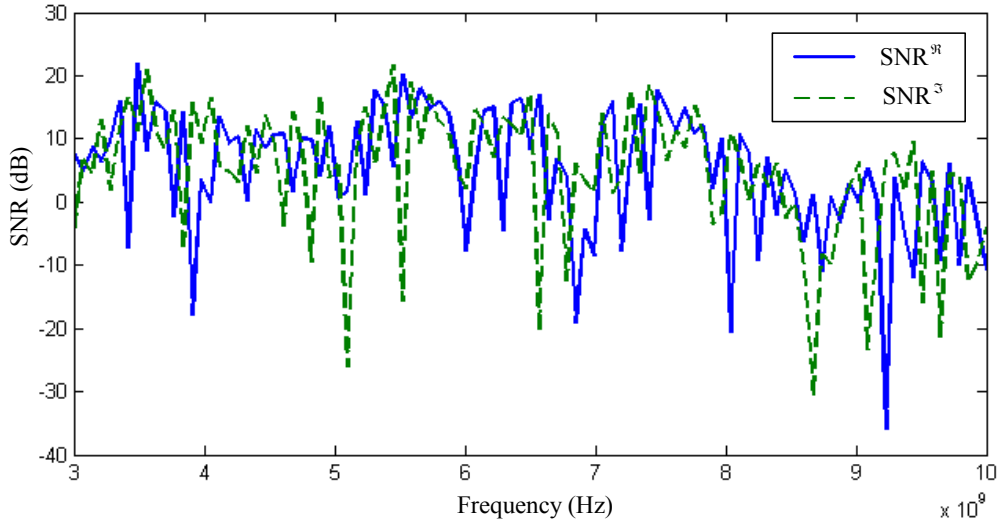

(b)

Fig. 5.10. Real SNR and imaginary SNR processed using (5.11) and (5.12), respectively, in: (a) a linear scale and (b) dB.

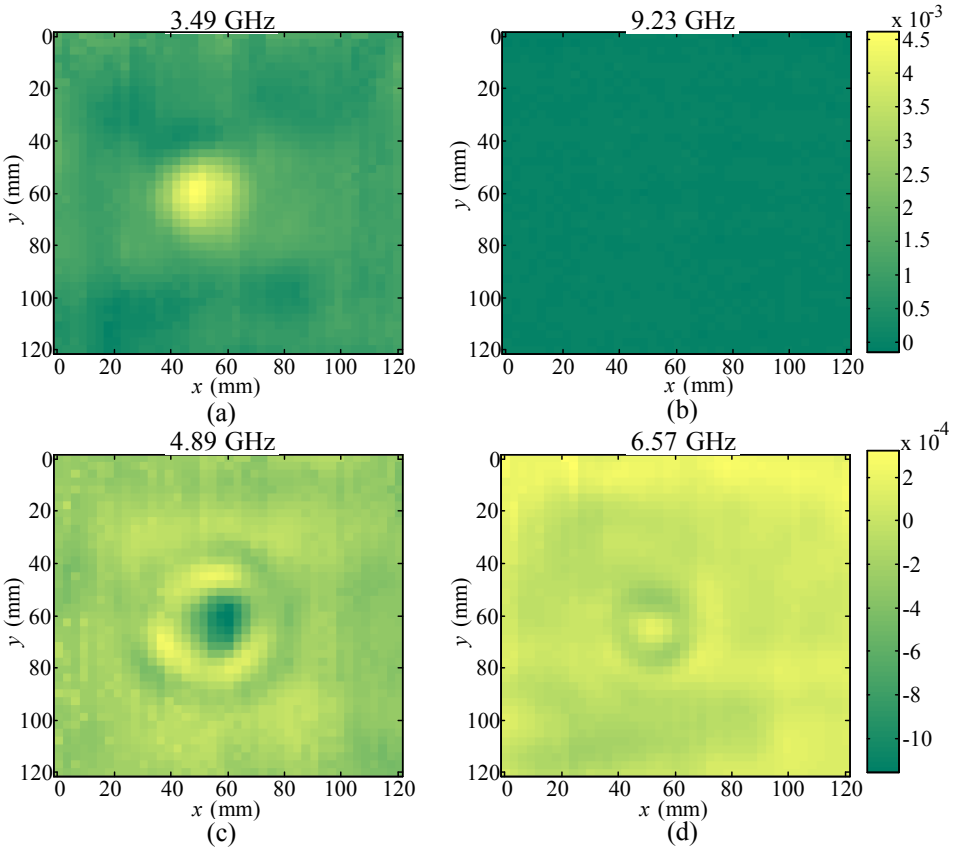

Fig. 5.11. Real *S*-parameter image at the frequency associated with: (a) maximum $\mathrm{SNR}^{\Re}$ and (b) minimum $\mathrm{SNR}^{\Re}$. Imaginary image at the frequency associated with: (c) maximum $\mathrm{SNR}^{\Im}$ and (d) minimum $\mathrm{SNR}^{\Im}$. The standard deviation of the feature free region in the real component at 9.23 GHz is $3.4\text{x}10^{-5}$ and in the imaginary component at 6.57 GHz is $10.1\text{x}10^{-5}$.

5.3.4. Complex-Valued Single Image Formulation

The complex-valued single image formulation reduces to

$$\mathrm{SNR} = \frac{\text{average}(\Delta S(\vec{\mathbf{r}}_{\mathrm{ROI}}))}{\text{std dev}(\Delta S(\vec{\mathbf{r}}_{\mathrm{B}}))}, \tag{5.13}$$

where the average and standard deviation are defined in (5.5) and (5.6), respectively.

The plots in Fig. 5.12 (a) and (b) show the expected trend of having low SNR above 8 GHz. They also have some distinct points that have a lower SNR than the average value below 8 GHz. Fig. 5.13 (a) shows the magnitude image associated with the maximum SNR. This image shows a distinct peak and has relatively low noise in the feature free region. Fig. 5.13 (b) shows the magnitude image associated with the minimum SNR, which shows no targets. Fig. 5.13 (c) shows the phase image associated with the minimum SNR and does have noise; however, this image can still yield good results in the reconstruction. Fig. 5.13 (d) shows the phase image associated with the minimum SNR and is pure noise. Based on these results, it seems that the complex-valued single image formation can produce a good representation of the data quality.

5.3.5. Peak Signal-to-Noise Ratio

The results for the PSNR are shown when applied to the complex-valued approach. The plots in Fig. 5.14 (a) and (b) show that SNR and PSNR have the same trend over frequency. The PSNR has a slightly higher value than SNR which is expected as it utilizes peak signal strength. This demonstrates that both PSNR and SNR can be used when evaluating the quality of an image.

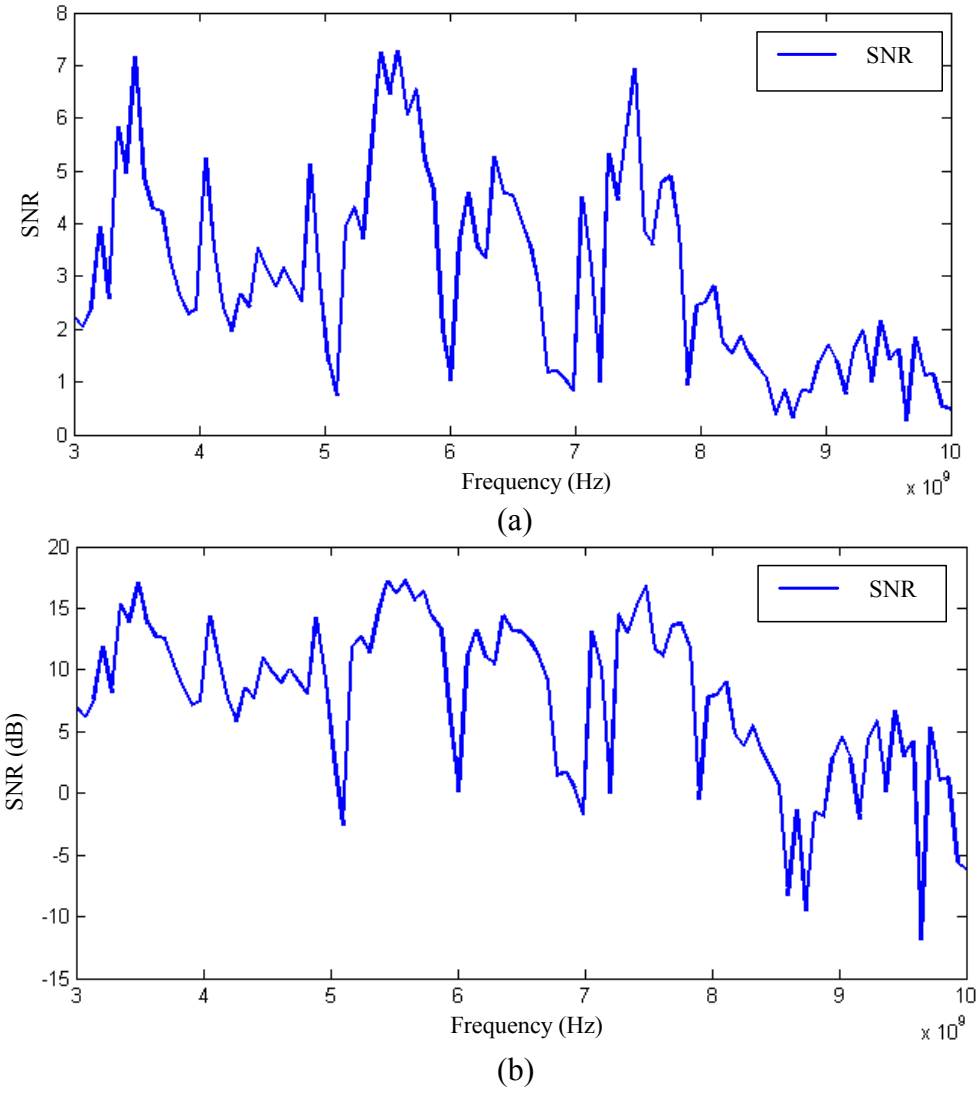

Fig. 5.12. Complex SNR evaluated using (5.13) in: (a) a linear scale and (b) dB.

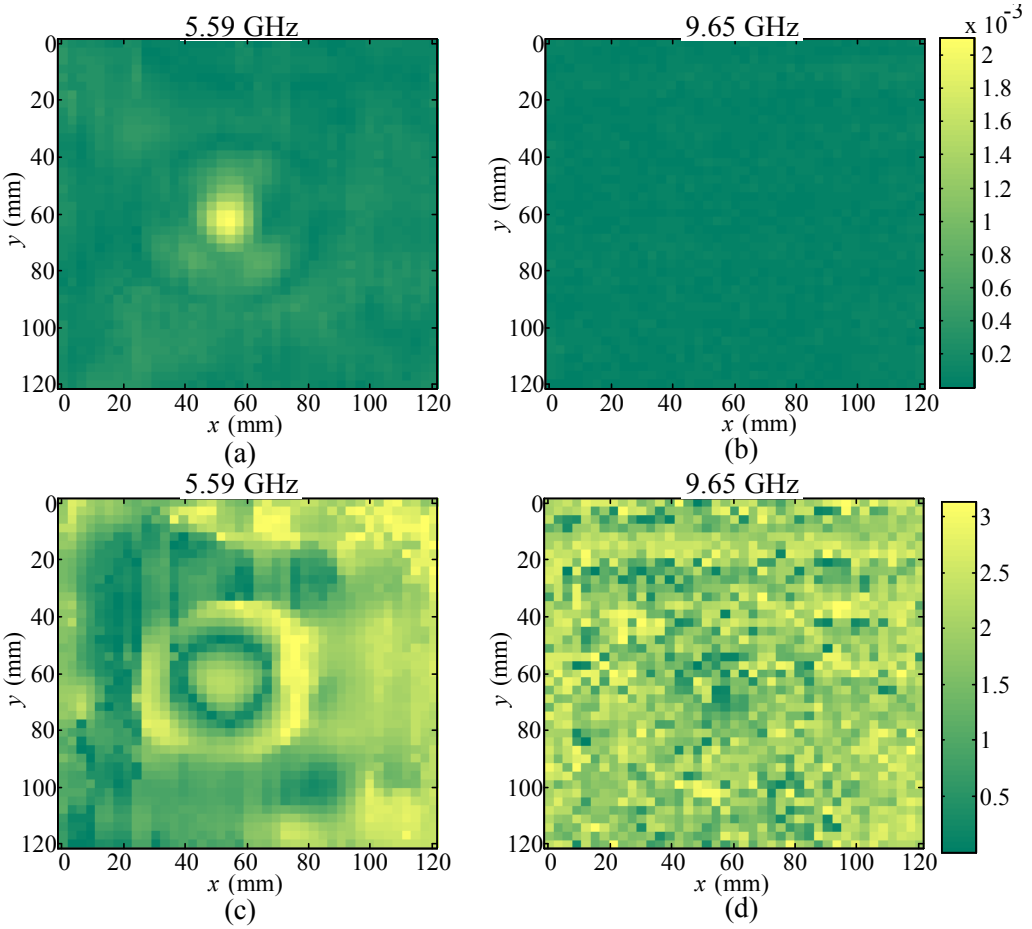

Fig. 5.13. Magnitude *S*-parameter image at the frequency associated with: (a) maximum SNR and (b) minimum SNR. Phase image in radians at the frequency associated with: (c) maximum SNR and (d) minimum SNR. The standard deviation of the feature free region at 9.65 GHz is 4.52×10^{-5}.

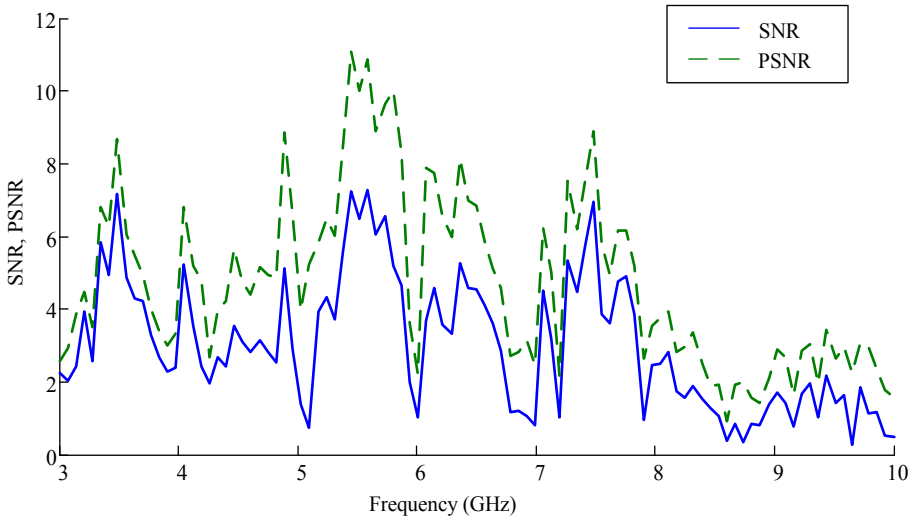

(a)

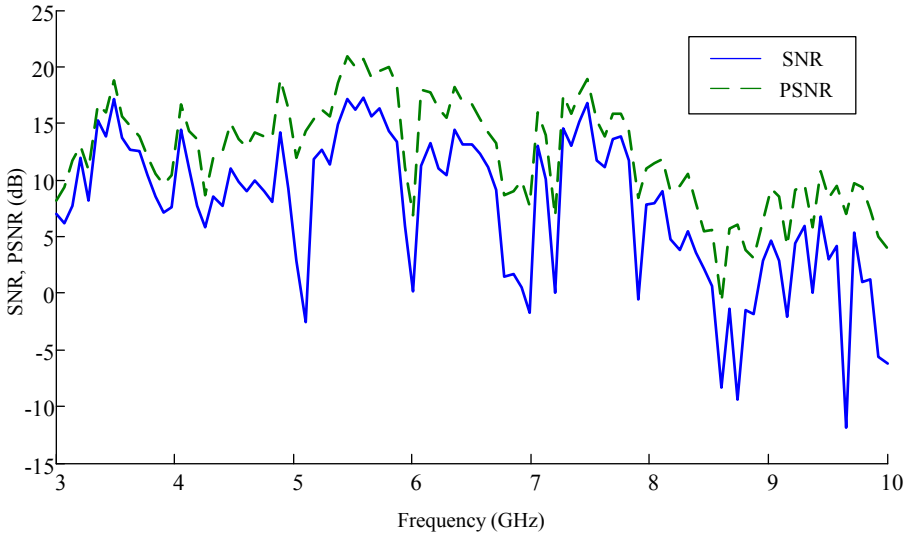

(b)

Fig. 5.14. Plots of SNR (5.13), and PSNR (5.8) in: (a) linear scale and (b) dB.

5.4. MATLAB USER INTERFACE

To facilitate the use of calculating the SNR of the images, it is useful to directly observe where the ROI and exclusion region are set in relation to the images. For this reason, a user interface was developed in MATLAB.

The main window of the user interface is shown in Fig. 5.15. There are three main regions of interest described as follows.

The bottom half of the user interface displays the SNR vs. frequency. There is also a horizontal red line to show the threshold level and a vertical red line to denote the frequency position of the image displayed in the upper left portion.

The upper left portion displays the magnitude image with a black box to denote the ROI and a magenta box to denote the exclusion zone. There is also the option to display the frequency mean image, which can help when selecting the values for the ROI and exclusion zone. Above the plot is the frequency at which the image occurs if the "Show Frequency Mean Image" option is unchecked.

The upper right portion has two drop down menus to select the CO and RO data to be used. Below this there are boxes to enter the extents of the ROI and CO in terms of the image index values. There is a dropdown menu to select the frequency vector, and a slider that is used to scroll through the images at different frequencies. If no frequency vector is selected, the user is prompted to specify which dimension of the CO and RO correspond to the frequency, and the index values are used. There is also a slider with a numeric input box to set the threshold level.

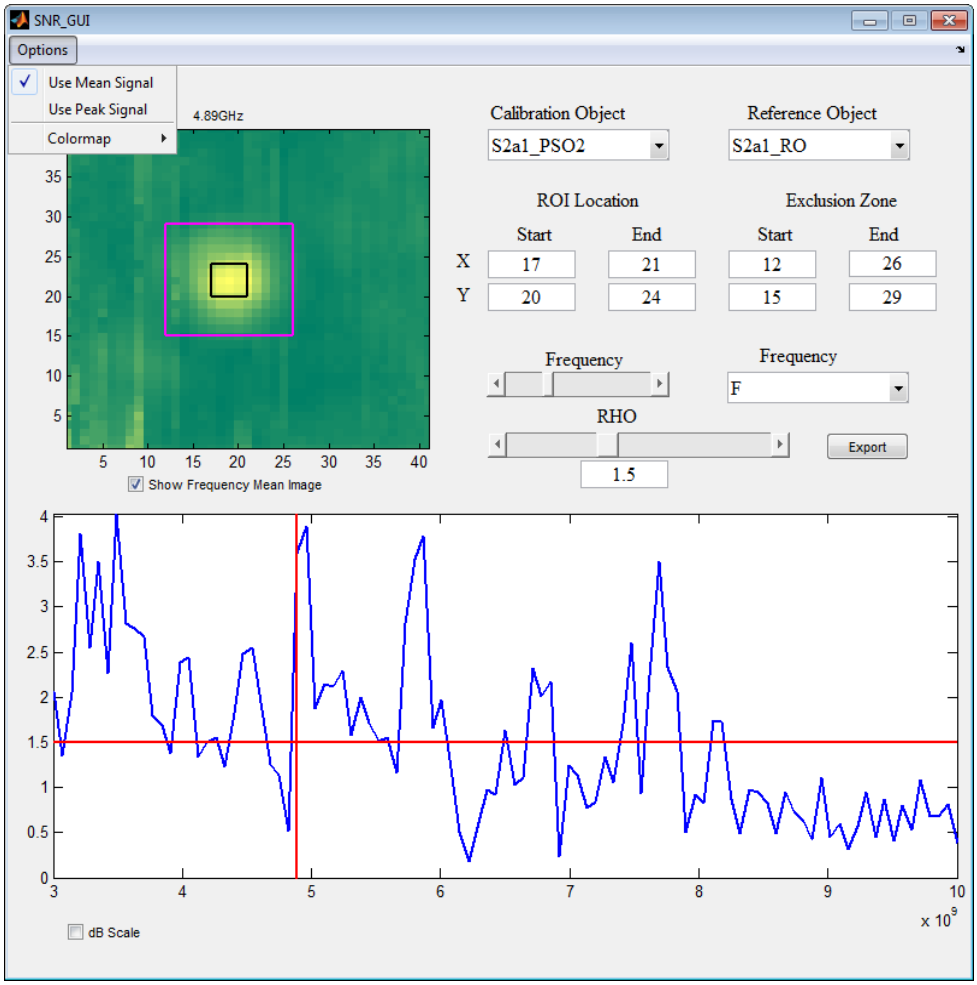

Fig. 5.15. MATLAB user interface for SNR calculation and frequency discrimination.

The export button allows specific data to be sent back to the workspace. The user interface may be called as a function, that outputs the variables of interest when the user interface is closed, for example to return the SNR, index of frequencies above the threshold `Fg_i` and index of frequencies below the threshold `Fb_i` for the CO measurement labelled `S2a1_PSO2` and the RO measurement labeled `S2a1_RO` the user would write:

```
[SNR, Fg_i, Fb_i]=SNR_GUI(S2a1_PSO2,S2a1_RO)
```

The output options are shown in the help file associated with the script.

Last, there is a drop down menu in the top left of the interface that has the option to choose how the signal strength is calculate (mean or peak), and choose the colormap for the image plot.

5.5. CONCLUSIONS

In Section 5.2 multiple method of calculating the signal to noise ration of a microwave imaging system are proposed. These methods differ on the method of extension to complex-valued images. In the author's opinion, the complex-valued formulation is the simplest to work with. However, for other imaging systems or reconstruction techniques, different methods may be better suited.

The SNR evaluation methods were applied to a verification example in Section 5.3. Both the SNR and PSNR methods performed well, and they all gave the same trends, however the values were different.

Section 5.4 introduces a graphical user interface that can be used to easily asses the SNR of *S*-parameter acquisition data. This user interface has options to use any of the formulations discussed in Section 5.2.

REFERENCES

[1] J.T. Case, M.T. Ghasr, and R. Zoughi, "Correcting mutual coupling and poor isolation for real-time 2-D microwave imaging systems," *IEEE Trans. Instrum. Meas.,* vol. 63, no. 5, pp. 1310–1319, Oct. 2013.

[2] S.J. Orfanidis, *Optimum Signal Processing: An Introduction*, 2nd ed. New York, NY, USA: MacMillan, 1985.

[3] L. Kaufman, D.M. Kramer, L.E. Crooks, and D.A. Ortendahl, "Measuring signal-to-noise ratios in MR imaging," *Radiology*, vol. 173, no. 1, pp. 265–267, 1989.

[4] M.J. Firbank, A. Coulthard, R.M. Harrison, and E.D Williams, "A comparison of two methods for measuring the signal to noise ratio on MR images," *Physics in Medicine and Biology*, vol. 44, no. 12, 1999.

[5] M.J. Firbank, R.M Harrison, E.D. Williams, and A. Coulthard, "Quality assurance for MRI: practical experience," *The British Journal of Radiology*, vol. 73, no. 868, pp. 376–383, 2000.

[6] O. Dietrich, J.G. Raya, S.B. Reeder, M.F. Reiser, and S.O. Schoenberg, "Measurement of signal-to-noise ratios in MR images: influence of multichannel coils. Parallel imaging, and reconstruction filters," *Journal of Magnetic Resonance Imaging*, vol. 26, no. 2, pp. 375–385, 2007.

[7] X. Song, B.W. Pogue, S. Jiang, M.M. Doyley, H. Dehghani, R.D. Tosteston, and K.D. Paulsen, "Automated region detection based on the contrast-to-noise ratio in near-infrared tomography, " *Applied Optics*, vol. 43, no. 5, pp. 1053–1062, 2004.

[8] T.G. Savelyev and A.G. Yarovoy, "Fast imaging by 3-D deconvolution in short-range UWB radar for concealed weapon detection," *The 9th European Radar Conference (EuRAD 2012)*, Oct. 2012.

[9] R.K. Amineh, J. McCombe, A. Khalatpour, and N.K. Nikolova, "Microwave holography using measured point-spread functions," *IEEE Trans. Instrum. & Meas.*, accepted.

[10] H. Xu, "Planar raster-scanning system for near-field microwave imaging," M.A.Sc. Thesis, Dept. Elect. and Comput. Eng., McMaster Univ. Hamilton, Ontario, Canada, 2011.

[11] R.K. Amineh, M. Ravan, A. Trehan, and N.K. Nikolova, "Near-field microwave imaging based on aperture raster scanning with TEM horn antennas," *IEEE Trans. Antennas Propag.*, vol. 59, no. 3, pp. 928–940, Mar. 2011.

CHAPTER 6

IMPACT OF NOISE AND UNCERTAINTY ON MICROWAVE HOLOGRAPHIC RECONSTRUCTION

Introduction

Holographic imaging is a three dimensional imaging method. In this chapter, we study the impact of noise and uncertainty in the raw data on the resulting reconstructed images. Methods of reducing the effects of this noise are studied and implemented to obtain high quality images from data acquired in lossy media, such as phantoms emulating breast tissue. This is a critical step in transforming holography into a potential algorithm for detecting tumors in breast tissue.

6.1. SUMMARY OF NEAR-FIELD MICROWAVE HOLOGRAPHY RECONSTRUCTION

Holographic imaging originated in the early 1970's when Farhat *et al.* [1]–[3] extended optical holography, which was developed by Gabor [4], to longer wavelengths. In current implementations of microwave holography, scanned transceivers measure the scattered-field phase and amplitude distributions over a rectangular [5],[6] or cylindrical [6]–[9] aperture. Once this is recorded, the image can be reconstructed using a Fourier-optics reconstruction that, in essence, emulates the hologram-based reconstruction process.

In [10] and [11], Amineh *et al.* extended the 3D holography technique to near-field imaging. In this case, the analytical approximations of the incident field and Green's function prove to be inadequate, prompting the use of numerical models instead, which are more accurate at representing the particular acquisition setup (including the antennas). The method proposed by Amineh in [10], [11] also incorporates forward-scattered signals, along with back-scattered signals that have been traditionally used. Incorporating forward-scattered signals allows for the imaging of very lossy media, where the back scattered signals are of much lower signal-to-noise ratio, compared with the forward-scattered data. However, back-scattered data was shown to be essential for the range resolution in 3D reconstruction [11], [12], when the signals are acquired with the planar scanning of two antennas aligned along boresight. This was remedied by Amineh in [12], by utilizing multiple receivers, offset from the transmitting antenna boresight,

thus restoring the range resolution when utilizing forward-scattered signals only.

In near-field holographic imaging [10]–[12], the incident field and the Green's function are obtained via simulations. In practice, however, the simulation models, although better than analytical approximations, may still be too inaccurate to ensure good image quality. The differences between the simulated models and the real acquisition setup are mostly due to the fabrication tolerances of the antennas and the complexities of near-field imaging (antenna holders, mechanical parts of the scanning systems, etc.). Adding additional complexity to the simulated model by including every connector and part of the scanning system is not practical because it demands prohibitive computational load. The major concern when using simulated models of the near-field system is not numerical errors, which can be reduced at the expense of computational time, but rather the inability to predict all factors that may arise in the practical implementation of the system. The latter errors are commonly referred to as modeling errors.

In [13] Amineh *et al.* proposed a method of acquiring the incident field and the Green function of a given acquisition system via measurements of a known calibration object (CO) is proposed. This method utilizes the concept of a point-spread function (PSF) of a linear imaging system, where the response due to any object is represented as the convolution of the response due to a point object (the measured CO response) with the spatial distribution of the arbitrary object. This

concept has been used in optical, acoustic, and microwave imaging (e.g., see [14], [13]–[19]).

The holographic approach developed by Amineh *et al.*in [13] is usedhere to study the effects of noise. The imaging algorithm Dr. Amineh developed is repeated here for completeness. Consider a setup which consists of two antennas performing a planar scan and an object in between as shown in Fig. 5.3. With proper calibration ($\Delta S^{\mathrm{OUT}} = S^{\mathrm{OUT}} - S^{\mathrm{RO}}$), the acquired signals are representative of the field scattered by the object. Microwave holography is based on the linear Born approximation of the electromagnetic scattering model [10] given in integral form by

$$\mathbf{E}^{\mathrm{sc}}(\mathbf{r}_P) \approx \iiint_{V_Q} \left[k_{\mathrm{s}}^2(\mathbf{r}_Q) - k_{\mathrm{b}}^2 \right] \underline{\underline{\mathbf{G}}}(\mathbf{r}_P, \mathbf{r}_Q) \cdot \mathbf{E}^{\mathrm{inc}}(\mathbf{r}_Q) d\mathbf{r}_Q. \tag{6.1}$$

Here, $\mathbf{E}^{\mathrm{sc}}$ is the scattered field, $\underline{\underline{\mathbf{G}}}$ is Green's dyadic function, $\mathbf{E}^{\mathrm{inc}}$ is the incident field, k_{s} and k_{b} are the wavenumbers of the scatterer and the background medium, respectively, and V_Q is the inspected volume. We assume that k_{b} is known for the imaged volume. The position vectors $\mathbf{r}_P$ and $\mathbf{r}_Q$ give the locations of the observation and scattering points, respectively.

As shown in [13], the scattered field at the frequency ω_l in (6.1) can be written as

$$E^{\mathrm{sc}}(x', y', \omega_l) \approx k_0^2(\omega_l) \int_z \int_y \int_x f(x, y, z) \cdot a(x - x', y - y', z, \omega_l) dx dy dz \,, \tag{6.2}$$

where $k_0(\omega_l)$ is the wavenumber in vacuum, (x', y') is the position of observation (or data acquisition), (x, y, z) is a position in the imaged volume, and

$$f(x, y, z) = \varepsilon_{\mathrm{r,s}}(x, y, z) - \varepsilon_{\mathrm{r,b}}(z), \tag{6.3}$$

$$a(x, y, z, \omega_l) = E^{\mathrm{inc}}(x, y, z, \omega_l) G(x, y, z, \omega_l). \tag{6.4}$$

Here, $\varepsilon_{\mathrm{r,s}}(x, y, z)$ is the complex permittivity distribution of the scatterer, $\varepsilon_{\mathrm{r,b}}(z)$ is the RO permittivity (assumed constant in x and y) and $G(x, y, z, \omega_l)$ is the Green tensor.

Holography aims to reconstruct the contrast function $f(x, y, z)$. If we assume that a sufficiently small CO is located at $(0, 0, z_n)$, the contrast function in (6.3) can be written as:

$$f(x, y, z_n) \approx C\delta(x, y, z - z_n), \tag{6.5}$$

where C is the complex-valued permittivity contrast between the CO and the background, and $\delta(\cdot)$ is the Dirac delta function. Substituting (6.5) into (6.2), the received scattered field of the CO is

$$E^{\mathrm{sc,co}}(x', y', \omega_l; z_n) \approx C \cdot k_0^2(\omega_l) \cdot a(-x', -y', z_n, \omega_l). \tag{6.6}$$

The scattered field in (6.6) represents the measurements of the CO at all N_z desired range locations (or layers) of interest z_n, $n = 1, \ldots, N_z$. This is in effect the PSF of the acquisition system at the respective range distances. From (6.2) and (6.6), the scattered field for any unknown object, which must be larger than the CO, can be expressed as

$$E^{\mathrm{sc}}(x',y',\omega_l) \approx \frac{1}{C}\sum_{n=1}^{N_z}\Delta z_n \iint_{xy} f(x,y,z_n)\cdot E^{\mathrm{sc,co}}(x'-x,y'-y,\omega_l;z_n)dydx\,, \quad (6.7)$$

where Δz_n is the distance between the range planes. Here, the integral over *x* and *y* can be interpreted as a 2D convolution. Thus, the 2D Fourier Transform (FT) of $E^{\mathrm{sc}}(x',y',\omega_l)$ is

$$\tilde{E}^{\mathrm{sc}}(k_x,k_y,\omega_l) \approx \frac{1}{C}\sum_{n=1}^{N_z}\Delta z_n \tilde{F}(k_x,k_y,z_n)\cdot \tilde{E}^{\mathrm{sc,co}}(k_x,k_y,\omega_l;z_n), \quad (6.8)$$

where $\tilde{F}(k_x,k_y,z_n)$ and $\tilde{E}^{\mathrm{sc,co}}(k_x,k_y,\omega_l;z_n)$ are the 2D FTs of $f(x,y,z_n)$ and $E^{\mathrm{sc,co}}(x,y,\omega_l;z_n),$ respectively; and k_x and k_y are the respective Fourier variables, i.e., the spatial frequencies. $\tilde{E}^{\mathrm{sc}}(k_x,k_y,\omega_l)$ is the 2D FT of the measured (calibrated) *S*-parameters of the unknown object.

In order to reconstruct the contrast function, (6.8) is applied at all frequencies ω_l $(l=1,\ldots,N_\omega)$ to obtain a linear system of equations at each spatial frequency pair $\boldsymbol{\kappa} = (k_x, k_y)$:

$$\begin{bmatrix} \tilde{E}^{\mathrm{sc}}(\boldsymbol{\kappa},\omega_1) \\ \vdots \\ \tilde{E}^{\mathrm{sc}}(\boldsymbol{\kappa},\omega_{N_\omega}) \end{bmatrix} \approx \frac{1}{C}\begin{bmatrix} \tilde{E}^{\mathrm{sc,co}}(\boldsymbol{\kappa},\omega_1;z_1)\Delta z_1 & \cdots & \tilde{E}^{\mathrm{sc,co}}(\boldsymbol{\kappa},\omega_1;z_{N_z})\Delta z_{N_z} \\ \vdots & & \vdots \\ \tilde{E}^{\mathrm{sc,co}}(\boldsymbol{\kappa},\omega_{N_\omega};z_1)\Delta z_1 & \cdots & \tilde{E}^{\mathrm{sc,co}}(\boldsymbol{\kappa},\omega_{N_\omega};z_{N_z})\Delta z_{N_z} \end{bmatrix}\begin{bmatrix} \tilde{F}(\boldsymbol{\kappa},z_1) \\ \vdots \\ \tilde{F}(\boldsymbol{\kappa},z_{N_z}) \end{bmatrix}. \quad (6.9)$$

The system in (6.9) is solved in a least squares sense at each $\boldsymbol{\kappa}$. Once all of the systems of equations for all $\boldsymbol{\kappa}$ are solved, the inverse 2D FT of $\tilde{F}(k_x,k_y,z_n)$, $n=1,2,\ldots,N_z$, is taken to reconstruct a 2D slice of the function $f(x,y,z_n)$ at each $z=z_n$ plane. The modulus of $f(x,y,z_n)$ is normalized by the maximum of

$|f(x,y,z_n)|$ over all z_n and it is plotted versus the spatial coordinates x and y to obtain 2D images of the object at all N_z planes.

This is extended to the case of multiple receivers by creating the system shown in (6.9) for each receiver. Then these systems are stacked together and solved in a least squares sense at each spatial frequency pair $\boldsymbol{\kappa}$. Assuming there are N_{r} receiving antennas, we can write

$$\underline{\tilde{\boldsymbol{E}}}^{\mathrm{sc}} = \underline{\underline{\tilde{\boldsymbol{D}}}}\,\underline{\tilde{\boldsymbol{F}}}\,, \tag{6.10}$$

where

$$\underline{\tilde{\boldsymbol{E}}}^{\mathrm{sc}} = \begin{bmatrix} \underline{\tilde{\boldsymbol{E}}}_1^{\mathrm{sc}} \\ \vdots \\ \underline{\tilde{\boldsymbol{E}}}_{N_r}^{\mathrm{sc}} \end{bmatrix},\ \underline{\underline{\tilde{\boldsymbol{D}}}} = \begin{bmatrix} \underline{\underline{\tilde{\boldsymbol{D}}}}_1 \\ \vdots \\ \underline{\underline{\tilde{\boldsymbol{D}}}}_{N_r} \end{bmatrix},\ \underline{\tilde{\boldsymbol{F}}} = \begin{bmatrix} \tilde{F}(\boldsymbol{\kappa}, z_1) \\ \vdots \\ \tilde{F}(\boldsymbol{\kappa}, z_{N_z}) \end{bmatrix},$$

$$\underline{\tilde{\boldsymbol{E}}}_r^{\mathrm{sc}} = \begin{bmatrix} \tilde{E}_r^{\mathrm{sc}}(\boldsymbol{\kappa}, \omega_1) \\ \vdots \\ \tilde{E}_r^{\mathrm{sc}}(\boldsymbol{\kappa}, \omega_{N_\omega}) \end{bmatrix},\ r = 1, \ldots, N_{\mathrm{r}},$$

$$\underline{\underline{\tilde{\boldsymbol{D}}}}_r = \frac{1}{C} \begin{bmatrix} \tilde{E}_r^{\mathrm{sc,co}}(\boldsymbol{\kappa}, \omega_1; z_1)\Delta z_1 & \cdots & \tilde{E}_r^{\mathrm{sc,co}}(\boldsymbol{\kappa}, \omega_1; z_{N_z})\Delta z_{N_z} \\ \vdots & \vdots & \vdots \\ \tilde{E}_r^{\mathrm{sc,co}}(\boldsymbol{\kappa}, \omega_{N_\omega}; z_1)\Delta z_1 & \cdots & \tilde{E}_r^{\mathrm{sc,co}}(\boldsymbol{\kappa}, \omega_{N_\omega}; z_{N_z})\Delta z_{N_z} \end{bmatrix}.$$

This builds an over-determined system with $N_\omega \cdot N_r$ equations in N_z unknowns. This allows for excluding the frequency points where the data has low SNR on a per-receiver basis. Thus, data of good SNR for one receiver is included, but can be excluded for a different receiver, if the data has low SNR.

6.2. MEASUREMENT DESCRIPTION

The measurement results shown here are from the same measurement described in Section 5.3.2. Three CO measurements are taken corresponding to z=20 mm, z=30 mm, and z=40 mm. The Object Under Test (OUT) consists of three dielectric targets in different range and cross-range positions. The first target is at (x=10 mm, y=-5 mm, z=20 mm), and its properties are $\varepsilon_r = 45$ and $\tan\delta \approx 0.001$. The second target is located at (x=20 mm, y=-15 mm, z=20 mm) with the same properties. The third target is located at (x=0 mm, y=0 mm, z=40 mm) and has properties of $\varepsilon_r = 50$ and $\tan\delta \approx 0.001$. All targets are cylinders with a diameter of 10 mm and a height of 10 mm. The z coordinate of the cylinder corresponds to the center of the cylinder; for example, the first target at z=20 mm extends from z=15 mm to z=25 mm.

A reconstruction error (RE) is calculated based on our prior knowledge of the OUT. The reconstruction error is defined in the same way in [13] as

$$\mathrm{RE}(z_n) = \frac{1}{N_x N_y} \sum_{i=1}^{N_x} \sum_{j=1}^{N_y} \left\| \, | f(x_i, y_j, z_n) | / M - \overline{I}(x_i, y_j, z_n) \right\|, \qquad (6.11)$$

where $\|\cdot\|$ is the $L1$ norm, N_x and N_y are the number of samples along the x and y directions, respectively, $|f(x_i, y_j, z_n)|$ is a slice of the image at z_n and M is the maximum contrast value found in the entire set of slices $|f(x_i, y_j, z_n)|$, $n = 1, 2, \ldots, N_z$. The function $I(x_i, y_j, z_n)$ represents the true magnitude of target's contrast normalized to its maximum value. It is between 0 and 1 inside the target

(depending on the contrast of the target) and 0 elsewhere. To have an overall estimate of the reconstruction error, the parameter RE^{t} is defined as

$$\mathrm{RE}^{\mathrm{t}} = \frac{1}{N_z}\sum_{n=1}^{N_z}\mathrm{RE}(z_n)\,. \tag{6.12}$$

6.3. IMPACT OF SPECTRAL FILTERING

The analytical limits on k_x and k_y are related to the sampling step in x and y according to the Nyquist-Shannon sampling theorem, which states:

$$f_{\max} \le \frac{f_s}{2}, \tag{6.13}$$

where $f_{\max}$ is the maximum detectable frequency without aliasing and f_s is the sampling frequency. Converting this in terms of spatial frequency, we obtain

$$k_x^{\max} \le \frac{\pi}{\Delta x},\ k_y^{\max} \le \frac{\pi}{\Delta y}, \tag{6.14}$$

which states that the phase variation must be less than π over the sampling step. For the current measurement, the sampling step is 3 mm in x and y. This in turn implies that $k_x^{\max}, k_y^{\max} \le \pi/3$ rad/mm, or approximately 1.047 rad/mm.

When using a CO, the object is assumed to be a point scatterer so that its contrast function can be written in the form (6.5). This implies that the size of the CO determines the smallest sized voxel that can accurately be reconstructed. Therefore, for a CO of diameter 10 mm, the largest k_x (or k_y) needed for accurate reconstruction is $\pi/10$ rad/mm, or approximately 0.314 rad/mm. Therefore, all data above this level is mostly noise. Filtering is not necessary when the CO size

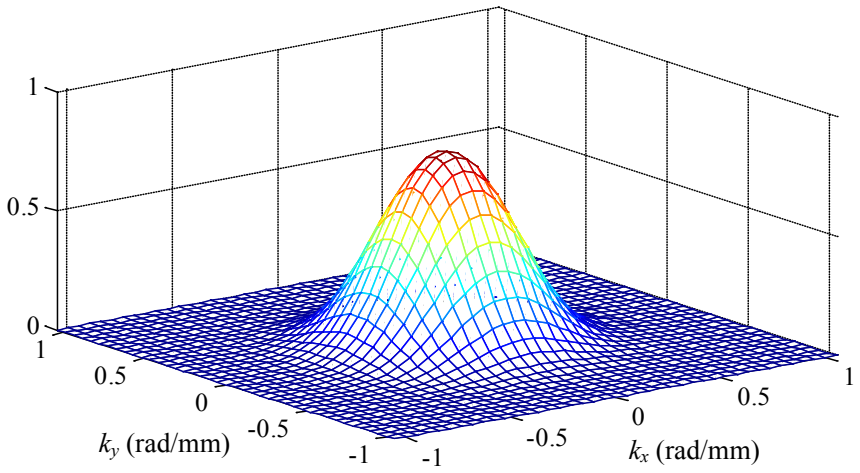

Fig. 6.1. Plot of the Gaussian window used to suppress the contributions of noise during image reconstruction.

is less than or equal to the spatial step of the scan. In the authors experience filtering is not as essential when working with simulation data as the noise levels are lower than in the experimental data.

In order to remove these effects, a Gaussian filter is applied to the data before the inverse Fourier Transform is applied. Here, a Gaussian filter with $\sigma = 2$ is created using the MATLAB function `fspecial`. A second thresholding window is created that is zero for all k_x , k_y above $\pi/10$ rad/mm and one elsewhere. This final window is created using the function `fwind2`, which generated a time-domain window. However, as we require the window in *k*-space, we use the function `freqz2` to transform the window into *k*-space. This window is applied to the magnitude of the spectrum only. The final window is shown in Fig. 6.1.

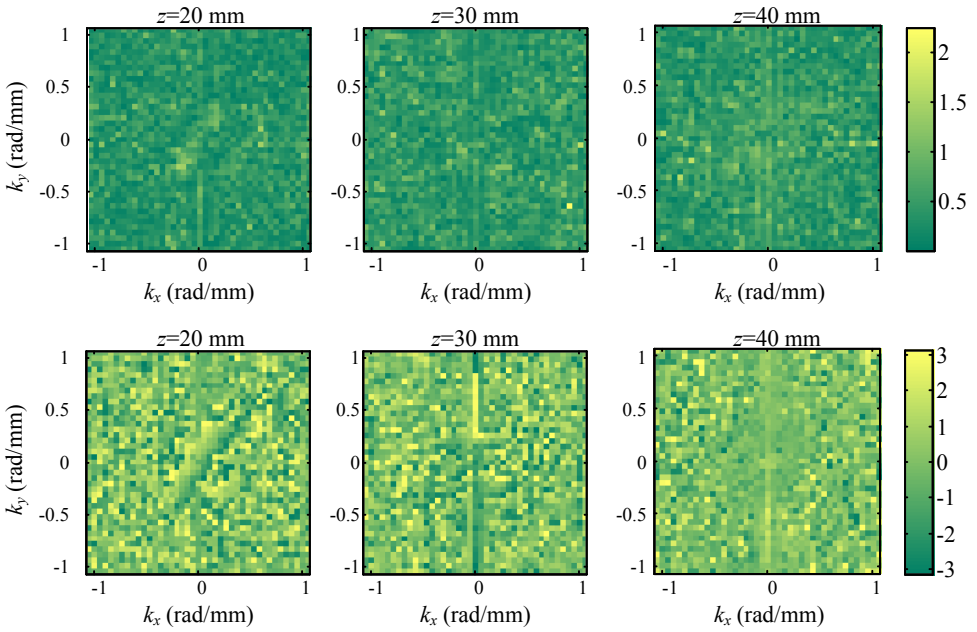

Fig. 6.2. Images of $\underline{\tilde{\mathbf{F}}}$ in (6.10), representing the spectrum of the final images before windowing. The images in the upper row correspond to the magnitude of the spectrum, and the images in the lower row correspond to the phase at the three separate range locations. The images are noisy.

This windowing step is essential when utilizing low-quality data, as is the case in tissue imaging where the losses are high. To illustrate this point, Fig. 6.2 and Fig. 6.3 show the resulting spectrum before and after filtering, respectively. Fig. 6.4 shows the reconstructed images in real space with and without filtering. For comparison, Fig. 6.5 shows the spectrum of the free-space measurement from [13] where the losses are negligible, the SNR is relatively good, and filtering is not necessary.

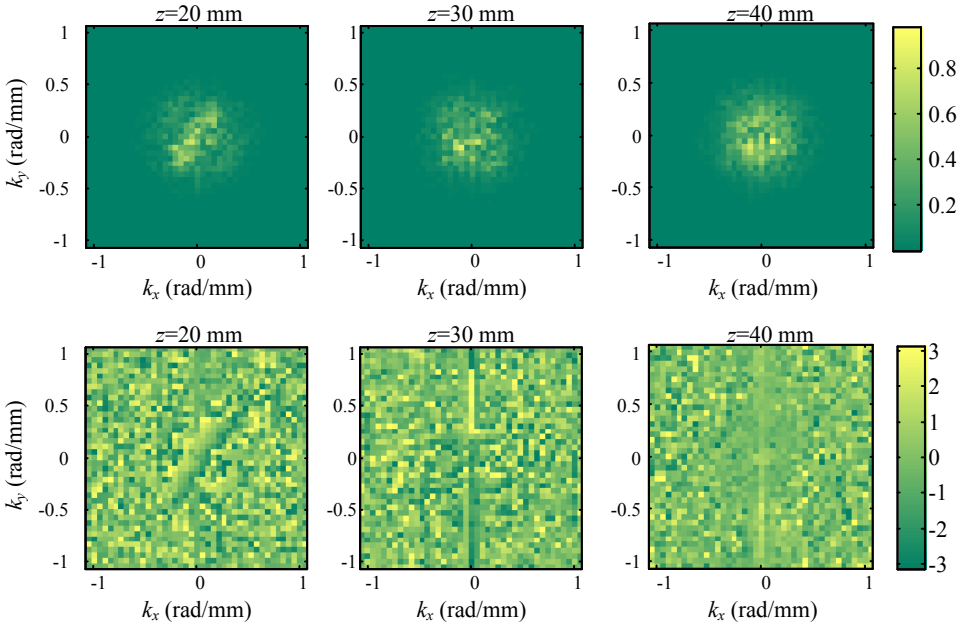

Fig. 6.3. Images of $\underline{\tilde{\mathbf{F}}}$ in (6.10), represent the spectrum of the final images after windowing. The images in the upper row correspond to the magnitude of the spectrum, and the images in the lower row correspond to the phase at the three separate range locations. The filtering reduces the noise significantly

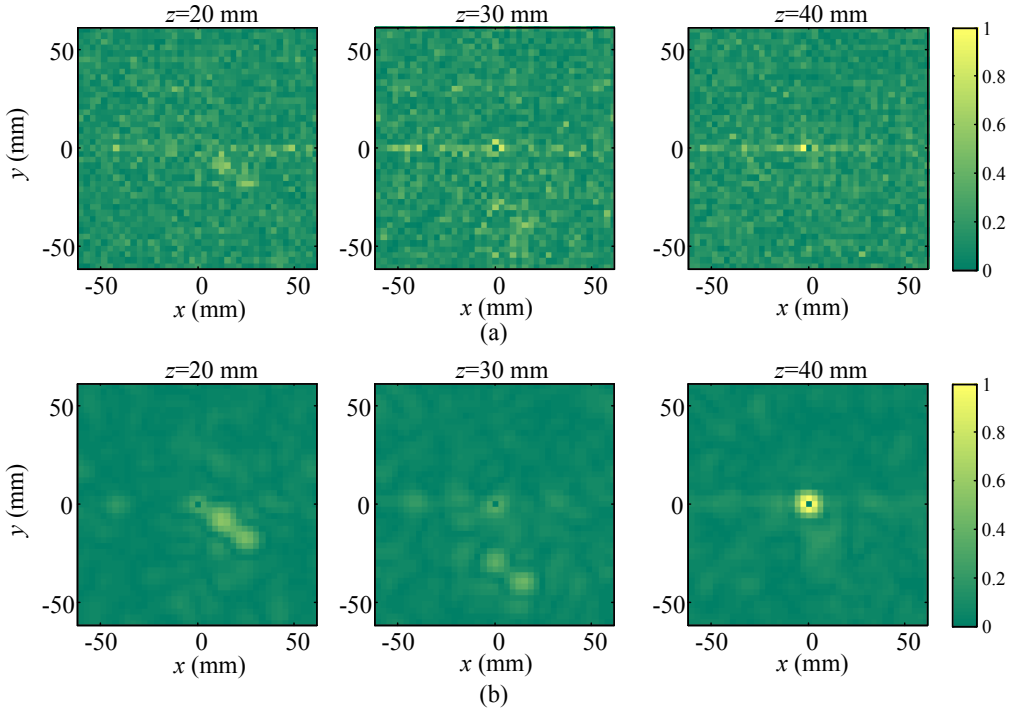

Fig. 6.4. Final images reconstructed using: (a) the unfiltered spectrum from Fig. 6.2, (b) the filtered spectrum from Fig. 6.3.

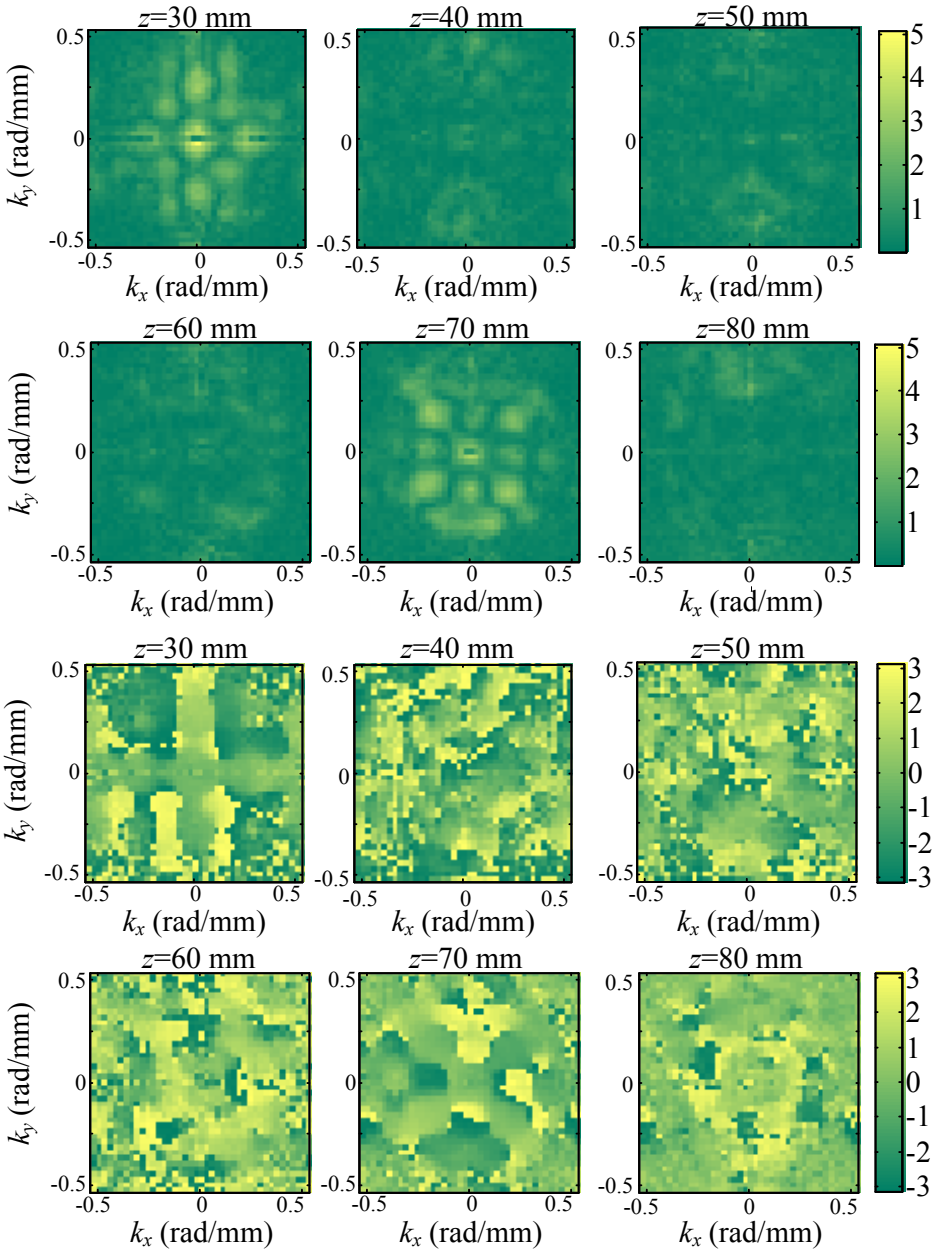

Fig. 6.5. Images of $\underline{\tilde{\mathbf{F}}}$ in (6.10), representing the spectrum of the final images from the free-space measurement with two metallic crosses at the z=30 mm and z=70 mm planes from [13]. The images in the upper two rows correspond to the magnitude of the spectrum, and the images in the lower two rows correspond to the phase at the six separate range locations.

6.4. ARTIFACT REDUCTION USING INTERPOLATED CO

The system matrix $\underline{\underline{\tilde{\mathbf{D}}}}$ in the over-determined system of equations (6.10) has a size of $N_\omega \cdot N_r \times N_z$. Typically, $N_\omega \cdot N_r$ is on the order of hundreds while N_z is less than 10. This yields a very tall matrix, which can cause some artifacts in the reconstructed images as it can be harder to solve. Therefore, it may be advantageous to artificially add additional unknowns to make the system slightly more square. This can be accomplished by interpolating the CO data along *z*. For example, if we measure a CO at *z* = [20, 30, 40] mm, we can interpolate between these points and solve our system at *z* = [20, 25, 30, 35, 40] mm. However, the method of interpolation will affect the solution. For example, using a linear interpolation, we are adding linearly dependent columns to the system, which will increase the condition number of the system.

Fig. 6.6 shows the holographic imaging results when interpolating using a linear interpolation method. None of the artifacts have been suppressed due to the fact that the added equations are linearly dependent. When using a cubic spline, however, this linear dependence is supressed and the artifacts are reduced significantly by adding two additional reconstruction planes; see Fig. 6.7 Interpolating to Δz=2.5 mm further reduces these artifacts.

TABLE 6.1 shows the reconstruction error for the images shown in Fig. 6.6 and Fig. 6.7 These reconstruction errors confirm that no improvement is seen when using a linear interpolation. However when using a cubic spline with Δz=5

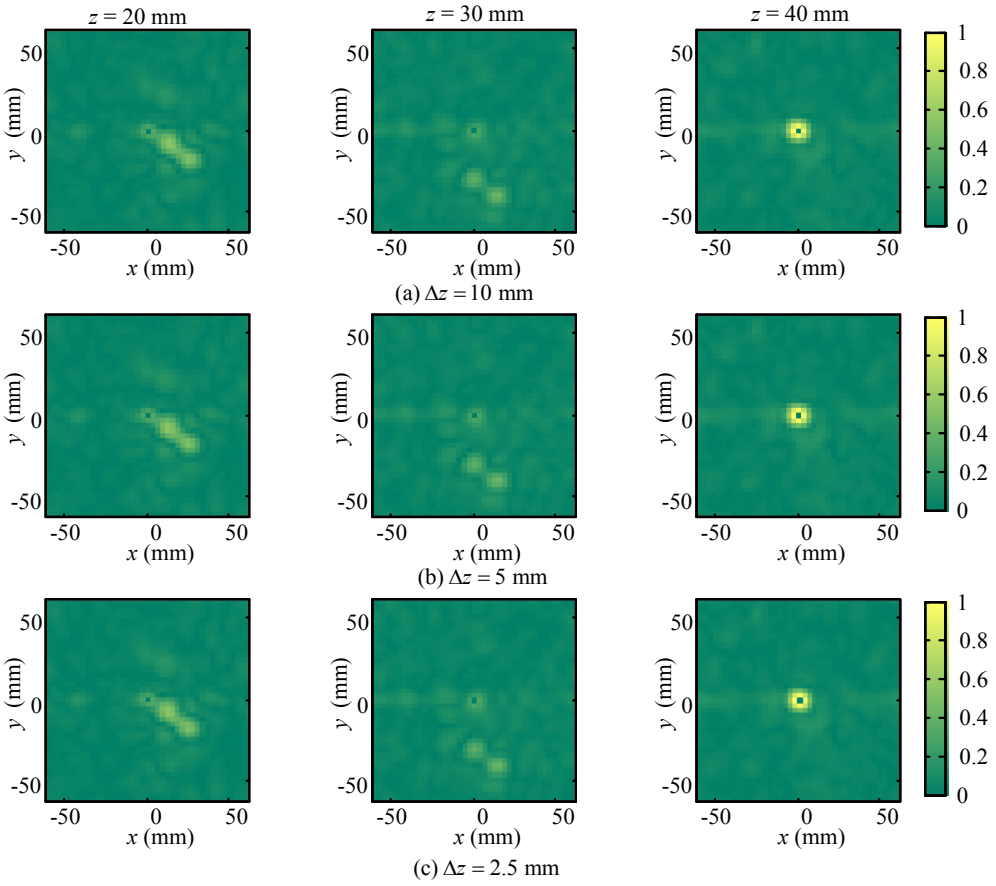

Fig. 6.6. Holographic imaging results for: (a) no interpolation, (b) interpolation by reducing the range z sampling rate to Δz=5 mm, and (c) interpolation where Δz =2.5 mm. All interpolation is linear. No improvement is seen.

mm, the error is reduced in the z = 30 mm plane. Note that this comes at the expense of the reconstruction error in the other planes and the total error is acctually increased to 0.0548. When interpolating with Δz=2.5 mm, the reconstruction error improves for the z = 30 mm and remains the same in the z = 20 mm plane, but the z = 40 mm plane is worse than before. On the other hand, the total reconstruction error improves to 0.0478. Regardless of the reconstruction error, the images have improved greatly when interpolating the CO measurements

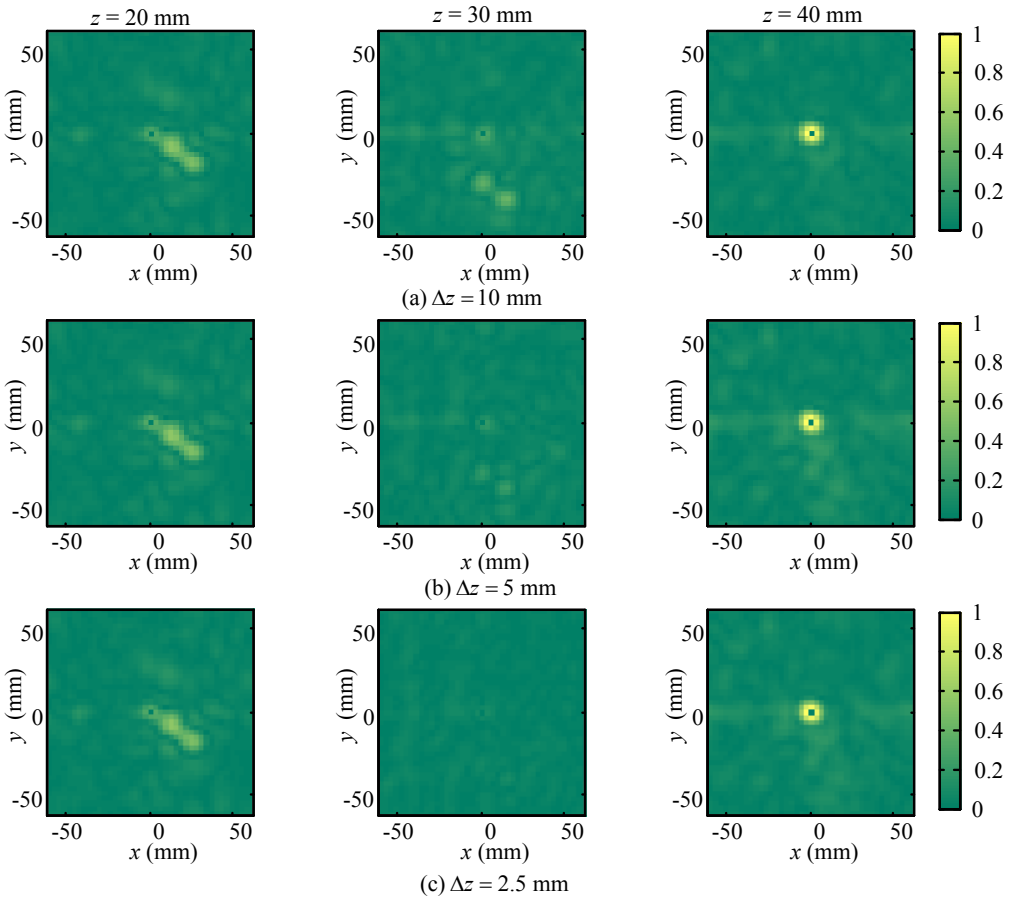

Fig. 6.7. Holographic imaging results for: (a) no interpolation, (b) interpolation with Δz =5 mm, and (c) interpolation with Δz =2.5 mm. All interpolation is cubic spline. Artifact reduction is seen in the z = 30 mm plane.

using a cubic spline, which seems to model the dependence of the CO scattered signals in the range direction adequately. This dependence is expected to be strongly non-linear due to the rapid attenuation of the field in the direction of propagation.

TABLE 6.1: RECONSTRUCTION ERRORS USING INTERPOLATION TECHNIQUES

		RE	RE^t
No Interpolation	z=20 mm	0.0515	0.0529
	z=30 mm	0.0563	
	z=40 mm	0.0511	
Linear interpolation Δz =5 mm	z=20 mm	0.0515	0.0529
	z=30 mm	0.0563	
	z=40 mm	0.0511	
Linear interpolation Δz =2.5 mm	z=20 mm	0.0515	0.0529
	z=30 mm	0.0563	
	z=40 mm	0.0511	
Cubic Spline interpolation Δz =5 mm	z=20 mm	0.0531	0.0548
	z=30 mm	0.0457	
	z=40 mm	0.0655	
Cubic Spline interpolation Δz =2.5 mm	z=20 mm	0.0515	0.0478
	z=30 mm	0.0305	
	z=40 mm	0.0613	

6.5. DATA FREQUENCY SELECTION FOR IMAGE IMPROVEMENT

Since the contrast function $f(x, y, z_n)$ is assumed frequency independent, we have as many equations as we have frequency points in (6.9), to solve for one vector. This yields an over-determined system that is solved in the least squares sense. As such, some noise in the data is suppressed by the least squares solution. However, to ensure that the solution is as accurate as possible, it is best to remove any frequency points that have a large level of noise, as this corrupts the solution. This may help to reduce artifacts in the reconstructed images.

In this study, the five co-polarized bowties will be used for reconstruction. The base images are reconstructed using all 101 frequency points. This yields a 505×3 system matrix $\underline{\underline{\tilde{\mathbf{D}}}}$ to be solved at each spatial frequency pair $\boldsymbol{\kappa}$.

In order to illustrate and quantify the improvement, the following is reported: (i) the reconstructed images, (ii) the condition number of $\underline{\underline{\tilde{\mathbf{D}}}}$ in (6.10) plotted against k_x and k_y, (iii) reconstruction error, are shown for the cases of:

1. no frequency removal,
2. only using frequency points that are good for all receivers,
3. only using frequency points that are bad for all receivers,
4. discriminating frequency points on a per-receiver basis.

This shows how the frequency discrimination affects the conditioning of the system as well as the final images. All results shown are without the use of regularization in the least squares solution.

6.5.1. Holographic Results

Fig. 6.8 shows the return loss of the transmitting and receiving antenna as well as the SNR of: (a) receiver #1 and (b) receiver #2. Images of the raw data magnitude corresponding to the maximum and minimum SNR are shown along with the images that are nearest to, but above, and nearest to, but below, the threshold. The threshold is shown in the same plot as the SNR and the vertical lines are shown in the SNR and return loss plots to indicate at which frequency the four scenarios occur. The threshold was set by comparing images that fall above and below it, as well as utilizing the prior knowledge of poor SNR above 8 GHz. The SNR is analyzed on one CO measurement where the CO is at the z=20 mm plane. Based on these SNR results, the reconstruction results are shown next for the four cases described above.

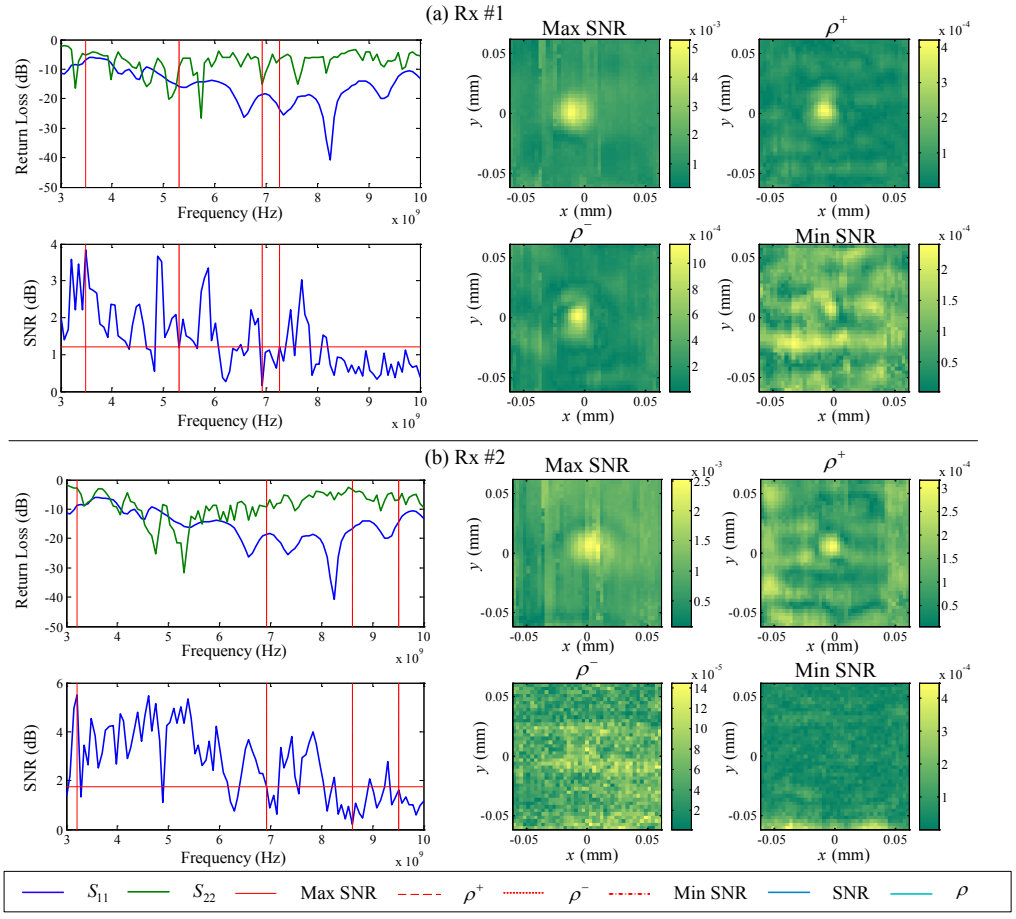

Fig. 6.8. Sample SNR plots for :(a) Receiver #1, and (b) Receiver #2. The upper left plot shows the return loss of the bowtie receiver (green) and the transmitting antenna (blue). The lower left plot shows the SNR calculated according to (5.21) along with the threshold ρ (horizontal line). The raw *S*-parameter magnitude images corresponding to the frequency with the best SNR (top left), SNR slightly above the threshold (ρ^+, top right), SNR slightly below the threshold (ρ^-, bottom left), and the worst SNR (bottom right). Vertical lines that match these frequency selections are placed in the SNR and return loss plots.

With reference to the return loss and the SNR plots in Fig. 6.8, there is correlation between the two, i.e., many of the dips in the SNR occur when the return loss peaks. This shows that the return loss of the antenna does affect the SNR of the system, which is expected. In Fig. 6.8 (a), the raw-data image with the

maximum SNR shows a strong target signature. Near the threshold, the raw-data images still show strong target signature but the signal levels are weaker. The raw-data image with minimum SNR is pure noise, as expected. In Fig. 6.8 (b), the raw-data image with the maximum SNR shows a clear peak at the target location and the signal values are quite large. However, there is some noise in the image. This is most likely due to the weaker signals received as this antenna is shifted off the boresight of the transmitter. Slightly above the threshold (at ρ^+) the raw-data image still has a distinct peak, but the noise has increased. Below the threshold (at ρ^-) the image is pure noise. This is also the case for the raw-data image with the minimum SNR.

After the data discrimination and selection based on the evaluated SNR of each receiver, the images are reconstructed utilizing microwave holography. Fig. 6.9 shows the results of the holographic reconstruction for each of the four discrimination scenarios. When reconstructing the images using all frequency points (Fig. 6.9(a)), the target at the z=40 mm plane is distinct and very strong. The two targets at the z=20 mm plane are visible and relatively strong compared with the background. These two targets are also separable. There is an artifact at the center of this plane due to the target at z=40 mm. When the data at the frequencies where the SNR is below the threshold (calculated using the CO at z=20 mm) are excluded and only reconstructing with the frequencies that are above the SNR threshold in all receivers, there is a slight improvement in the strength of the targets in the z=20 mm plane, as shown in Fig. 6.9(b). When

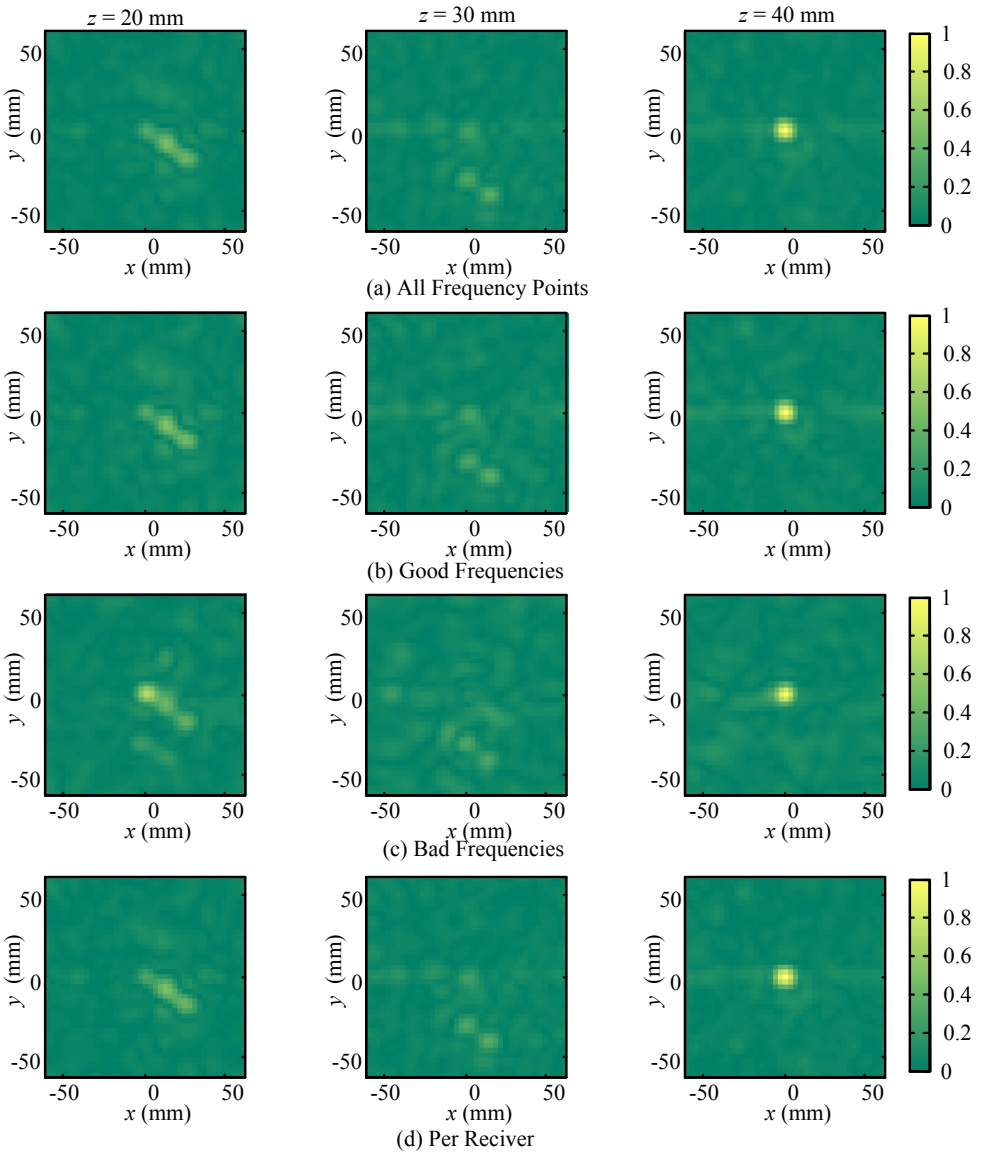

Fig. 6.9. Holographic imaging results for: (a) no frequency removal, (b) using only frequency points that are good for each receiver, (c) using only frequency points that are bad for each receiver, and (d) discriminating on a per-receiver basis. The discrimination is done based on the SNR's for the CO at z=20 mm.

reconstructing using only the frequency points below the SNR threshold, Fig. 6.9(c), we see that the artifact in the z=20 mm plane becomes very strong. This shows that the signals with poor SNR do cause inaccurate results during

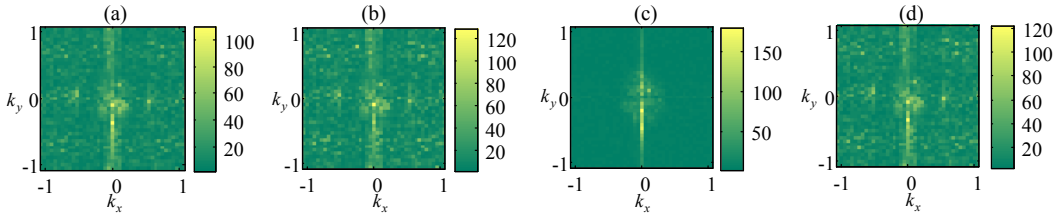

Fig. 6.10. 2D colour plots of the condition number of the system matrix $\underline{\underline{\tilde{\mathbf{D}}}}$ in (6.10) over k_x and k_y (in rad/mm): (a) no frequency removal, (b) using only frequency points that are good for each receiver, (c) using only frequency points that are bad for each receiver, and (d) discriminating on a per-receiver basis.

reconstruction. When discriminating the frequencies on a per-receiver basis, Fig. 6.9(d) , we again see some improvement compared to using all frequency points, but there is still an artifact in the z=20 mm plane.

Fig. 6.10 shows the 2D color plots of the condition numbers of the system matrix versus k_x and k_y. Comparing the condition numbers between the case of using all frequency points (Fig. 6.10 (a)) and the case of using only good frequency points in all receivers (Fig. 6.10 (b)), we do not see any improvement. In fact, at some (k_x ,k_y) pairs, the condition number increases. The same conclusion holds for the per-receiver case (Fig. 6.10 (d)). We also see a larger difference in the condition number when using only bad data (Fig. 6.10 (c)). However, the condition number does not become excessively large. We emphasize that good condition numbers do not imply good reconstructed images.

TABLE 6.2 shows the noise analysis for each of the four cases. As we can see the reconstruction error becomes worse when using the frequency points that are good in all receivers. As expected, it is reduced when using the frequency points that are bad in all receivers. When discriminating on a per receiver bases,

TABLE 6.2: RECONSTRUCTION ERROR & RUN TIME AFTER FREQUENCY DISCRIMINATION BASED ON A CO AT z=20 MM

		RE	RE^t	Run Time (s)
No Removal	z=20 mm	0.0453	0.0470	1.98
	z=30 mm	0.0504		
	z=40 mm	0.0454		
Good in All Receivers	z=20 mm	0.0537	0.0539	1.01
	z=30 mm	0.0565		
	z=40 mm	0.0514		
Bad in All Receivers	z=20 mm	0.0586	0.0607	0.945
	z=30 mm	0.0637		
	z=40 mm	0.0598		
Per-Receiver	z=20 mm	0.0472	0.0488	1.792
	z=30 mm	0.0523		
	z=40 mm	0.0469		

the reconstruction is almost identical to that when using all data points. This demonstrates that microwave holography, in its current form, is robust against noise due to its least squares solution that effectively disregards low quality data. However, by first performing the SNR analysis, the size of the system matrix in (6.10) is reduced from 505×3 when using all frequencies to 95×3 when using only good frequencies, or 210×3 when using the per- receiver approach. This reduction in system size allows for faster reconstruction.

For further examination, the SNR is evaluated for each CO. Then, the frequency discrimination results are combined across the CO measurements for each receiver. The reconstruction results for the cases of per-receiver and for all common good frequency points between the receivers are shown in Fig. 6.11. The reconstruction using all frequency points is show in Fig. 6.11(a) for comparative purposes. Comparing Fig. 6.11 (a) and Fig. 6.11 (b), it becomes obvious that when using frequency points that are good for all receivers the quality of the

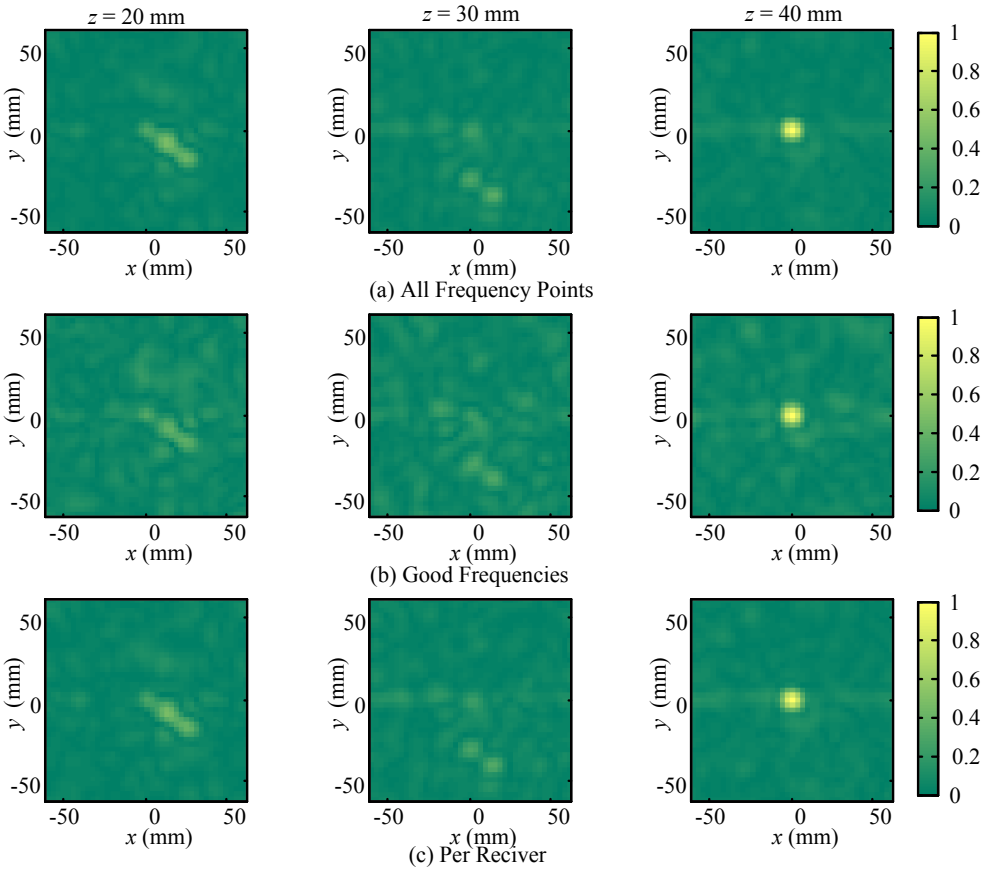

Fig. 6.11. Holographic imaging results for: (a) no frequency removal, (b) using only frequency points that are good for all receivers, and (c) discriminating on a per-receiver basis using a combination of the SNR results from each CO.

image in the z=20 mm plane decreases. However, some slight improvement is observed when using the per-receiver discrimination, Fig. 6.11 (c). These results are somewhat reflected in the images of the system condition number, Fig. 6.12. The condition number increases at some (k_x, k_y) pairs when using common frequency points between the receivers. When using the per-receiver approach, the condition number is slightly increased, but the reconstructed results are still good.

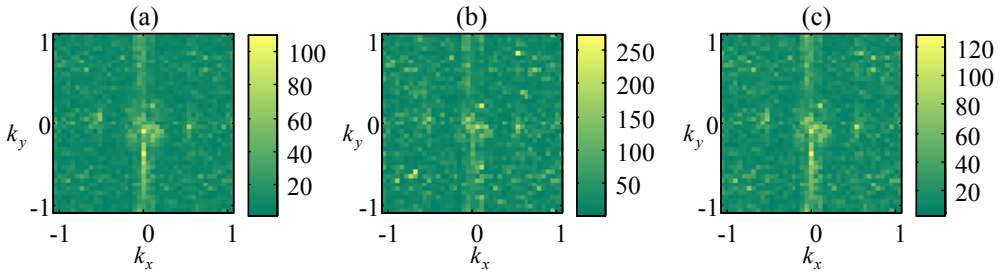

Fig. 6.12. 2D colour plots of the condition number of the system matrix $\underline{\underline{\tilde{\mathbf{D}}}}$ in (6.10) over k_x and k_y (in rad/mm): (a) no frequency removal, (b) using only frequency points that are good for each receiver, and (c) discriminating on a per-receiver basis.

TABLE 6.3: RECONSTRUCTION ERROR & RUN TIME AFTER FREQUENCY DISCRIMINATION BASED ON COMBINED CO SNR'S

		RE	RE^t	Run Time (s)
No Removal	z=20 mm	0.0453	0.0470	1.98
	z=30 mm	0.0504		
	z=40 mm	0.0454		
Good in all receivers	z=20 mm	0.0702	0.0696	0.966
	z=30 mm	0.0718		
	z=40 mm	0.0668		
Per-Receiver	z=20 mm	0.0479	0.0501	1.65
	z=30 mm	0.0537		
	z=40 mm	0.0486		

TABLE 6.3 shows the error analysis for the images in Fig. 6.11. It demonstrates that the reconstruction error increases in both discrimination methods. However, as stated previously, the per-receiver method provides good RE with a smaller system matrix of 210×3.

6.6. CONCLUSIONS

In Section 6.3, a method to de-noise the holographic reconstructed images is proposed based on filtering the spectrum of the least squares solution. This filter is set to a cut-off frequency that corresponds to the maximum spectral

component determined by the size of the calibration object used in the system characterization. As this object sets the resolution of the final images, all spectral components above this are assumed to be due to noise.

In Section 6.4, interpolation between the CO *z* planes is used to reduce the level of artifacts in the images. When using a cubic spline interpolation, this method improves the image quality by suppressing artifacts. Further investigation into the effects of the interpolation is needed especially when there are objects in each imagining plane.

Finally, in Section 6.5, we have applied the complex-valued single image SNR technique for the purpose of selecting frequency points that are submitted for reconstruction. Due to the least squares solution in holography, only a small improvement is achieved. The only significant benefit is in the drastic reduction of the size of the system matrices of the least square systems of equations (see (6.10)), which reduces the CPU time of the reconstruction.

REFERENCES

[1] N.H. Farhat and W.R. Guard, "Millimeter wave holographic imaging of concealed weapons," *Proc. IEEE (Lett.)*, vol. 59, no. 9, pp. 1383 –1384, 1971.

[2] N.H. Farhat, "Microwave holography and its applications in modern aviation," in *Proc. SPIE Eng. Applicat. Holography Symp.*, 1972, pp. 295–314.

[3] G. Tricoles and N.H. Farhat, "Microwave holography: Applications and techniques," *Proc. IEEE*, vol. 65, no. 1, pp. 108–121, Jan. 1977.

[4] D. Gabor, "A new microscope principle," *Nature*, vol. 161, May 1948.

[5] D.M. Sheen, D.L. McMakin, and T. E. Hall, "Three- dimensional millimeter-wave imaging for concealed weapon detection," *IEEE Trans. Microwave Theory Tech.*, vol. 49, no. 9, pp. 1581–1592, Sep. 2001.

[6] D.M. Sheen, D.L. McMakin, and T. E. Hall, "Near-field three-dimensional radar imaging techniques and applications," *Applied Optics*, vol. 49, no. 19, pp. E83–E93, Jun. 2010.

[7] J. T. Case, M. Tayeb Ghasr, and R. Zoughi. "Nonuniform manual scanning for rapid microwave nondestructive evaluation imaging," *IEEE Trans. Instrument. and Meas.*, vol. 62, no. 5, pp. 1250–1258, May 2013.

[8] A. Dallinger, S. Schelkshorn, and J. Detlefsen, "Efficient ω–k-algorithm for circular SAR and cylindrical reconstruction areas," *Adv. Radio Sci.*, vol. 4, pp. 85–91, 2006.

[9] W.X. Tan, W. Hong, Y.P. Wang, and Y.R. Wu, "A novel spherical-wave three-dimensional imaging algorithm for microwave cylindrical scanning geometries," *Progress in Electromagnetics Research (PIER)*, vol. 111, pp. 43–70, 2011.

[10] R.K. Amineh, M. Ravan, A. Khalatpour, and N.K. Nikolova, "Three-dimensional near-field microwave holography using reflected and transmitted signals," *IEEE Trans. Antennas Propag.*, vol. 59, no. 12, pp. 4777−4789, Dec. 2011.

[11] R.K. Amineh, A. Khalatpour, H. Xu, Y. Baskharoun, and N. Nikolova, "Three-dimensional near-field microwave holography for tissue imaging," *Int. J. Biomed. Imaging,* Special Issue on Microwave Imaging and Emerging Applications*,* vol. 2012, Article ID 291494, 2012.

[12] R.K. Amineh, M. Ravan, J. McCombe, and N.K. Nikolova, "Three-dimensional microwave holographic imaging employing forward-scattered waves only," *Int. J. of Antennas and Propagation*, special issue on Inverse

Scattering and Microwave Tomography in Safety, Security, and Health, Vol. 2013, Article ID 897287, http://dx.doi.org/10.1155/2013/897287.

[13] R.K. Amineh, J. McCombe, A. Khalatpour, and N.K. Nikolova, "Microwave holography using measured point-spread functions," *IEEE Trans. Instrum. &Meas.*, accepted.

[14] T.G. Savelyev and A.G. Yarovoy "Fast imaging by 3-D deconvolution in short-range UWB radar for concealed weapon detection," *The 9th European Radar Conference (EuRAD 2012)*, Oct. 2012.

[15] J.W. Goodman, *Introduction to Fourier Optics* (McGraw-Hill, 1996).

[16] A. Schatzberg and A.J. Devaney, "Super-resolution in diffraction tomography," *Inverse Problems*, vol. 8, pp. 149−164, 1992.

[17] L. Diener, "Microwave near-field imaging with open-ended waveguide comparison with other techniques of nondestructive testing," *Res. Nondestr. Eval.*, vol. 7, pp. 137–152 ,1995.

[18] R. Zoughi, *Microwave nondestructive testing and evaluation*. Kluwer Academic Publishers, The Netherlands, 2000.

[19] M. Bertero, M. Miyakawa, P. Boccacci, F. Conte, K. Orikasa, and M. Furutani, "Image restoration in chirp-pulse microwave CT (CP-MCT)," *IEEE Trans. Biomed. Engineering*, vol. 47, no. 5, pp.690-699, May 2000.

CHAPTER 7

CONCLUSION AND FUTURE WORK

7.1. Concealed Weapon Detection Conclusions

In Chapter 1, the theory underlying the detection of concealed weapons with microwaves was outlined. Its implementation was developed for operation in a cluttered environment. This was verified in Chapters 2 and 3 with both a frequency-sweep system and a time-domain system. The frequency-sweep system is based on a VNA and achieves a sensitivity and specificity of up to 97%. The time-domain system achieves a sensitivity of 91% and a specificity of 66%. These values are expected to improve when utilizing a larger training set. Chapter 2 also discusses the effectiveness of deploying the system in an environment that is different from that in which it was classified. This work has led to a promising system, which is able to detect concealed weapons at a high speed and with the real possibility of being low-cost, compared to existing systems. However, it should be kept in mind that the classification step of the algorithm is performed in a "black box" approach. Further work is necessary form the classification side of the algorithm to ensure robust and proper operation.

7.2. Recommended Future Work in Concealed Weapon Detection

Although the results presented here are promising, there is still much work to be done to build a functional and practical system. One aspect that needs to be addressed is the classification stage of the algorithm. Further investigation should go into finding methods of performing classification directly on the extracted complex resonances rather than only the magnitude of the frequency domain

signal. Another area of interest in the classification stage is the use of a single-class classifier that will only require the signatures of weapons for training and will provide a positive/negative outcome on whether a weapon exists. Alternatively, a single-class classifier could be trained with measurements of people only, and the training set could be constantly updated as it is expected that there will be more people without weapons passing by the system than those with weapons. However, this poses a challenge in being able to detect weapons with a high degree of sensitivity and specificity.

There is also future work in designing a complete time domain prototype of a transmitter module, a receiver module, and a signal processing module. The transmitter module should generate a differentiated Gaussian pulse, possibly via step-recovery diode, amplifies it as needed, and deliver it to the transmitting antenna via a RF switch. The receiving module could have two channels, one for each polarization of the receiving antenna, or it could have a single channel that is switched. The channel would consist of a limiter, possibly a low noise amplifier, a balun to create a differential signal and one or more high speed analog to digital converters (ADC's) to directly sample the time-domain waveform. A differential signal is typically fed into the ADC as it provides a lower signal-to-noise ratio over a typical signal. The output of the ADC's would be fed into a field-programmable gate array (FPGA) to be stored in memory until processed by the signal processing module. A FPGA is typically used due to the extremely high

data rate from the high speed ADC. The signal processing stage would then utilize the stored waveforms and process them according to this algorithm.

The final work that could be done is the generation of a large training dataset. This would involve utilizing the system to measure many volunteers to effectively characterize the radar return from a single person without a weapon as well as multiple measurements of a variety of weapons. This could be performed in an anechoic environment, as discussed in previous chapters.

7.3. MICROWAVE IMAGING CONCLUSIONS

In Chapter 5, a method for evaluating the signal-to-noise ratio (SNR) in a raw *S*-parameter data set has been investigated. A method of calculating a single real-valued SNR to represent the complex *S*-parameter data set has been proposed and validated. The method works with a single image of the data acquired with a known calibration object (CO) when characterizing a typical microwave imaging measurement system. A user interface has been developed to offer a simple and fast method of computing the SNR to be used in image reconstruction.

In Chapter 6, a method for de-noising the holographic images has been proposed based on spectral windowing. Additionally, the use of interpolated CO data was investigated for the improvement of artifacts in the range direction. This study found that applying some interpolation (e.g., cubic splines) can reduce the number of artifacts in the reconstructed images. The complex-valued SNR technique for frequency discrimination was applied to holography. While excluding frequency points did not improve the overall quality of the images, it

did offer a reduction in the processing time of the algorithm, which is useful in developing a real-time system.

7.4. Recommended Future Work in Microwave Imaging

As a follow up on the work done during this research, future work in imaging can be focused in two areas: 1) raw data and 2) microwave holography.

Future work in raw data processing is very much needed to properly remove the background from the measurement of an object under test (OUT).The current method of simple subtraction of the background measurement from that of the OUT is inefficient and incapable of suppressing noise and uncertainty in the measurement. A more elegant and efficient method may be achieved by modeling the measurement using signal flow graph and then calibrating in a method similar to a VNA, similarly to what was is proposed in [1]. Additionally, an investigation into the possible use of a correlation canceller [2][3] should be completed.

There is also future work needed to analyze how different components of the scanning system affect the overall system SNR; for example, the choice of antennas, amplifiers, or the VNA. This will help to identify which components contribute the most significant uncertainty to the system output.

A method to analyze the image quality with respect to artifacts would be a good complement to the SNR evaluation. The standard deviation of the feature free region will not increase greatly if there is a single strong peak. This means that the current SNR evaluation method does not necessarily account for artifacts in the raw data. However, artifacts in the raw data could have a large impact on

the reconstructed images. Therefore, it would be beneficial to have a metric to quantify the amount of artifacts in the raw data.

Future work in holography should include an investigation of solvers used when computing the least squares solution from (6.10). Rather than using the mathematical solution of $\boldsymbol{x} = (\boldsymbol{A}^{\mathrm{T}}\boldsymbol{A})^{-1}\boldsymbol{A}^{\mathrm{T}}\boldsymbol{b}$ to solve the system $\boldsymbol{Ax} = \boldsymbol{b}$ in k-space, the use of an iterative solver should be investigated. The use of such a solver may allow for constraints to be placed on the solution which could yield better results. Additionally, the use of an L1 norm solver should be investigated. Such a solver minimizes the sum of the errors $\boldsymbol{Ax} - \boldsymbol{b}$ rather than the sum of the squared errors. This allows for a few of the equations to have a relatively large error, while the other equations will have a low error, i.e., some equations are effectively removed from the solution. The use of such a solver has been successful in many data fitting problems and may be successful in holography.

Future work is also needed to determine the best possible methods of filtering to ensure high quality reconstructed images. Additionally, work into updating holography into a quantitative method is necessary.

REFERENCES

[1] P.G. Bartley Jr. and S.B. Begley, "Improved free-space S-parameter calibration," *Instrumentation and Measurement Technology Conference (IMTC 2005)* Ottawa, Canada, May 2005

[2] J.T. Case, M.T. Ghasr, and R. Zoughi, "Correcting mutual coupling and poor isolation for real-time 2-D microwave imaging systems," *IEEE Trans. Instrum. Meas.,* vol. 63, no. 5, pp. 1310-1319, Oct. 2013.

[3] S.J. Orfanidis, *Optimum Signal Processing: An Introduction*, 2nd ed. New York, NY, USA: MacMillan, 1985.

BIBLIOGRAPHY

Advantest R3770 Network Analyzer (300 kHz – 20 GHz).

R.S. Adve, O.M. Pereira-Filho, T.K. Sarkar, and S.M. Rao, "Extrapolation of time domain responses from three dimensional objects utilizing the matrix pencil technique*," IEEE Trans. Antennas Propag.*, vol. 45, pp. 147–156, Jan. 1997.

Agilent E83638 PNA network analyzer (10 MHz – 40 GHz).

A. Agurto, Y. Li, G. Y. Tian, N. Bowring, and S. Lockwood, "A review of concealed weapon detection and research in perspective," *Proc. of the 2007 IEEE Int. Conf. on Networking, Sensing and Control*, Apr. 2007, pp. 443–448.

AKELA, "Demonstration of a concealed weapons detection system using electromagnetic resonances, final report", US Dept. of Justice, 2001, on line: http://www.ncjrs.gov/pdffiles1/nij/grants/190134.pdf

G.K. Allu, "Estimating the parameters of exponentially damped sinusoids in noise," Technical Report, University of Rhode Island, Kingston, Rhode Island, 02881, April 2003.

R.K. Amineh, A. Khalatpour, H. Xu, Y. Baskharoun, and N. Nikolova, "Three-dimensional near-field microwave holography for tissue imaging," *Int. J. Biomed. Imaging, Special Issue on Microwave Imaging and Emerging Applications*, vol. 2012, Article ID 291494, 2012.

R.K. Amineh, J. McCombe, A. Khalatpour, and N.K. Nikolova, "Microwave holography using measured point-spread functions," *IEEE Trans. Instrum. & Meas.*, accepted July 2014.

R.K. Amineh, J. McCombe, and N.K. Nikolova, "Microwave holographic imaging using the antenna phaseless radiation pattern," *IEEE Antennas Wireless Propagat. Lett.*,vol. 11 pp.1529–1532, Dec. 2012.

R.K. Amineh, M. Ravan, A. Khalatpour, and N.K. Nikolova, "Three-dimensional near-field microwave holography using reflected and transmitted signals," *IEEE Trans. Antennas Propag.*, vol. 59, no. 12, pp. 4777−4789, Dec. 2011.

R.K. Amineh, M. Ravan, A. Trehan, and N.K. Nikolova, "Near-field microwave imaging based on aperture raster scanning with TEM horn antennas," *IEEE Trans. Antennas Propag.*, vol. 59, no. 3, pp. 928–940, Mar. 2011.

R.K. Amineh, M. Ravan, J. McCombe, and N.K. Nikolova, "Three-dimensional microwave holographic imaging employing forward-scattered waves only," *Int. J. of Antennas and Propagation, special issue on Inverse Scattering and Microwave Tomography in Safety, Security, and Health*, Vol. 2013, Article ID 897287, http://dx.doi.org/10.1155/2013/897287.

R.K. Amineh, M. Ravan, J.J. McCombe, and N.K. Nikolova, "Range resolution in microwave imaging with forward-scattered waves only," *IEEE MTT-S Int. Microwave Symp.*, June 2013.

P.G. Bartley Jr. and S.B. Begley, "Improved free-space S-parameter calibration," *Instrumentation and Measurement Technology Conference (IMTC 2005)* Ottawa, Canada, May 2005.

M. Bertero, M. Miyakawa, P. Boccacci, F. Conte, K. Orikasa, and M. Furutani, "Image restoration in chirp-pulse microwave CT (CP-MCT)," *IEEE Trans. Biomed. Engineering*, vol. 47, no. 5, pp.690-699, May 2000.

C.M. Bishop, *Pattern Recognition and Machine Learning*. New York, NY: Springer, 2006.

R. Carrier and R.L. Moses, "High resolution radar target modeling using a modified Prony estimator," *IEEE Trans. Antennas and Propagation*, vol. 40, no. 1, pp. 13–18, Jan 1992.

J. T. Case, M. Tayeb Ghasr, and R. Zoughi. "Nonuniform manual scanning for rapid microwave nondestructive evaluation imaging," *IEEE Trans. Instrument. and Meas.*, vol. 62, no. 5, pp. 1250–1258, May 2013.

J.T. Case, M.T. Ghasr, and R. Zoughi, "Correcting mutual coupling and poor isolation for real-time 2-D microwave imaging systems," *IEEE Trans. Instrum. Meas.*, vol. 63, no. 5, pp. 1310–1319, Oct. 2013.

H.-M. Chen, S. Lee, R. M. Rao, M. A. Slamani, and P. K. Varshney, "Imaging for concealed weapon detection," *IEEE Signal Processing Mag*., Mar. 2005, pp. 52–61.

A. Dallinger, S. Schelkshorn, and J. Detlefsen, "Efficient ω–k-algorithm for circular SAR and cylindrical reconstruction areas," *Adv. Radio Sci.*, vol. 4, pp. 85–91, 2006.

L. Diener, "Microwave near-field imaging with open-ended waveguide comparison with other techniques of nondestructive testing," *Res. Nondestr. Eval.*, vol. 7, pp. 137–152 ,1995.

O. Dietrich, J.G. Raya, S.B. Reeder, M.F. Reiser, and S.O. Schoenberg, "Measurement of signal-to-noise ratios in MR images: influence of multichannel coils. Parallel imaging, and reconstruction filters," *Journal of Magnetic Resonance Imaging*, vol. 26, no. 2, pp. 375–385, 2007.

G. Dougherty, "Nonparametric Learning," *in Pattern Recognition and Classification: An Introduction.* New York, NY: Springer, 2013, ch. 6, pp. 104–117.

G. Dougherty, "Statistical Pattern Recognition," *in Pattern Recognition and Classification: An Introduction*. New York, NY: Springer, 2013, ch.4, pp. 43–54.

R.O. Duda, P.E. Hart, and D.G. Stork, "Multilayer Neural Networks," *in Pattern Classification*. 2nd ed. New York, NY: Weily, 2001, ch. 6, pp. 282-333.

N.H. Farhat and W.R. Guard, "Millimeter wave holographic imaging of concealed weapons," *Proc. IEEE (Lett.)*, vol. 59, no. 9, pp. 1383 –1384, 1971.

N.H. Farhat, "Microwave holography and its applications in modern aviation," *in Proc. SPIE Eng. Applicat. Holography Symp.*, 1972, pp. 295–314.

T. Fawcett, "An introduction to ROC analysis," *Pattern Recognition Letters*, vol. 27, no. 8, pp. 861–874, June 2006.

M.J. Firbank, A. Coulthard, R.M. Harrison, and E.D Williams, "A comparison of two methods for measuring the signal to noise ratio on MR images," *Physics in Medicine and Biology*, vol. 44, no. 12, 1999.

M.J. Firbank, R.M Harrison, E.D. Williams, and A. Coulthard, "Quality assurance for MRI: practical experience," *The British Journal of Radiology*, vol. 73, no. 868, pp. 376–383, 2000.

S.E. Fotinea, I. Dologlou, and G. Carayannis, "On the use of decimation for efficient spectral estimation", *International Journal of Computer Mathematics and its Applications*, vol. 8, Oct. 2006.

FT-RF Quad Ridge Horn Antenna HR-03M06G08-NF. http://www.taiwan-antenna.com/front/bin/ptdetail.phtml?Part=400MHz-6GHz-Dual-Polarization-Broadband-Horn-Antenna-N-Female-type008&Category=368755

D. Gabor, "A new microscope principle," *Nature*, vol. 161, May 1948.

M. Gashinova, M. Cherniakov, and A. Vasalos, "UWB signature analysis for detection of body-worn weapons," *in International Conference on Radar*, Shanghai, 2006.

General Microwave model 1699 0.1-20 GHz.

M. Georgiev and N.K. Nikolova, "Ultrawideband (UWB) high-resolution noise radar for concealed weapon detection," Technical Report to DRDC–Ottawa, Hamilton ON, April 2012.

J.W. Goodman, *Introduction to Fourier Optics* (McGraw-Hill, 1996).

S.W. Harmer, D.A. Andrews, N.D. Rezgui, and N.J. Bowring, "Detection of handguns by their complex natural resonant frequencies", *IET Microwave, Antennas & Propagation*, vol. 4, no. 9 , pp. 1182–1190, Sept. 2010.

F.J. Harris, "On the use of windows for harmonic analysis with the discrete Fourier transform," *Proc. IEEE*, vol. 66, no. 1, pp. 51–83, Jan. 1978.

J. Hausner and N. West, "Radar based concealed threat detector," *IEEE MTT-S Int. Microwave Symp.*, June 2007, pp. 765–768.

J. Hausner and N. West, "Radar based concealed threat detector*," IEEE Int. Conference on Microwaves, Communications, Antennas and Electronic Systems*, 2008 (COMCAS 2008), pp. 1–8.

F. Hu, "The band-pass matrix pencil method for parameter estimation of exponentially damped/undamped sinusoidal signals in noise," Ph.D. Thesis, Syracuse Univ., 1990.

Y. Hua and T.K. Sarkar, "Matrix pencil method for estimating parameters of exponentially damped/undamped sinusoids in noise," *IEEE Trans. Acoustics, Speech, and Signal Processing*, vol. 38, no. 5, pp. 814–824, May 1990.

A. R. Hunt, R. D. Hogg, and W. Foreman, "Concealed weapons detection using electro-magnetic resonances*," SPIE Conference on Enforcement and Security Technologies*, Boston, MA, Nov. 1998, pp. 62–67.

A. R. Hunt and R. D. Hogg, "A stepped-frequency CW radar for concealed weapon detection and through the wall surveillance," *in SPIE Proc. on Sensors and Command, Control, Communications and Intelligence (C3I) Technologies for Homeland Defense and Law Enforcement*, SPIE Proc. vol. 4708, 2002, pp. 99–105.

S. Ibrahim, K.R. Liu, D. Novak, and R.B. Waterhouse, "A subspace signal processing technique for concealed weapons detection," *IEEE International Conference on Acoustics, Speech and Signal Processing,* Honolulu, HI, 2007.

L. Kaufman, D.M. Kramer, L.E. Crooks, and D.A. Ortendahl, "Measuring signal-to-noise ratios in MR imaging," *Radiology*, vol. 173, no. 1, pp. 265–267, 1989.

P. E. Keller, D. L. McMakin, D. M. Sheen, A. D. McKinnon, and J. W. Summet, "Privacy algorithm for cylindrical holographic weapons surveillance system," *IEEE AES Systems Mag.*, Feb. 2000, pp. 17–23.

R. Kumaresan and D.W. Tufts, "Estimating the parameters of exponentially damped sinusoids and pole-zero modeling in noise," *IEEE Trans. Acoustics, Speech, and Signal Processing*, vol. 30, no. 6, pp. 833–840, 1982.

C. A. Martin, S. E. Clark, J. A. Lovberg, and J. A. Galliano, "Real-time wide-field-of-view passive millimetre-wave imaging," *Proc. SPIE*, vol. 4719, 2002, pp. 341–349.

MathWorks, "Neural Network Toolbox R2012b," [Online]. Available: http://www.mathworks.com/help/nnet/index.html

MathWorks, "Statistics Toolbox R2012b," [Online]. Available: http://www.mathworks.com/products/datasheets/pdf/statistics-toolbox.pdf

J. McCombe, "Microwave imaging raw signal-to-noise ratio analysis," Computational Electromagnetics Laboratory Technical Report *CEM-R-68*, Hamilton, ON, Nov. 2013.

J. McCombe, "Signal processing algorithms for resonance based concealed weapons detection," Computational Electromagnetics Laboratory Technical Report *CEM-R-63*, Hamilton, ON, Nov. 2012 .

J.J. McCombe, and N.K. Nikolova, "SNR assessment of microwave imaging systems," *IEEE AP-S/URSI Int. Symp. Antennas and Propagation*, July 2014.

J.J. McCombe, M.S. Georgiev, T. Thayaparan, and N.K. Nikolova, "Clutter removal in the automatic target detection with late time responses," *European Radar Conference 2013 (EuRAD 2013),* Oct. 2013.

D. L. McMakin, D. M. Sheen, and H. D. Collins, "Remote concealed weapons and explosive detection on people using millimeter-wave holography," *30th Annual 1996 Int. Carnahan Conference on Security Technology*, Oct. 1996, pp. 19–25.

K. Moussakhani, J.J. McCombe, and N.K. Nikolova, "Sensitivity evaluation of microwave imaging systems employing scattering-parameter measurements," *IEEE AP-S/URSI Int. Symp. on Antennas and Propagation*, July 2014.

K. Moussakhani, J.J. McCombe, and N.K. Nikolova, "Sensitivity of microwave imaging systems employing scattering-parameter measurements," *IEEE Trans. Microwave Theory Tech.*, accepted July 2014.

K. St. J. Murphy, R. Appleby, G. Sinclair, A. McClumpha, K. Tatlock, R. Doney, and I. Hutcheson, "Millimetre wave aviation security scanner," *IEEE 36th Annual Int. Conf. on Security Technology*, 2002, pp. 162–166.

N.K. Nikolova, "Microwave imaging for breast cancer," *IEEE Microw. Mag.,* vol. 12, no. 7, pp. 78 – 94, Dec. 2011.

N. K. Nikolova, "Ultrawideband (UWB) high-resolution noise radar for concealed weapon detection," Technical Report to DRDC–Ottawa, Hamilton, ON, June 30, 2009.

N. K. Nikolova, "Ultrawideband (UWB) high-resolution noise radar for concealed weapon detection," Technical Report to DRDC–Ottawa, Hamilton, ON, July 23, 2010.

N.K. Nikolova, J. McCombe, and T. Thayaparan, "Signal processing algorithms for resonance based concealed weapons detection with microwave radar," Computational Electromagnetics Laboratory Technical Report *CEM-R-64*, Hamilton, ON, March 2013.

D. Notel, J. Huck, S. Neubert, S. Wirtz, and A. Tessman, "A compact mmW imaging radiometer for concealed weapon detection," in *Proc. Infrared Millimeter Waves Conf.*, Cardiff, U.K., 2007, pp. 269–270.

D. O'Reilly, N. Bowring, and S. Harmer, "Signal processing techniques for concealed weapon detection by use of neural networks," *IEEE 27th Convention of Electrical & Electronics Engineers in Israel (IEEEI)*, Eilat, Israel, 2012.

S.J. Orfanidis, *Optimum Signal Processing: An Introduction*, 2nd ed. New York, NY, USA: MacMillan, 1985.

N. G. Paulter, "Guide to the technologies of concealed weapon imaging and detection," NIJ Guide 602-00, 2001, on line:
http://www.ncjrs.gov/pdffiles1/nij/184432.pdf.

A. Pergande and L. Anderson, "Video rate millimetre-wave camera for concealed weapon detection," *Proc. SPIE*, vol. 4373, 2001, pp. 35–39.

R. Prony, "Essai experimental et analytique sur les lois de la dilatabilite de fluides elastiques et sur celles del la force expansive de la vapeur de l'alkool a differentes temperatures," *Paris J. I'Ecole Polytech.*, vol. 1, pp. 24–76, 1795.

J.P. Reilly. ECE 712. Lecture 8, Topic: "The pseudo-inverse". Department of Electrical and Computer Engineering, McMaster University, Hamilton, ON, Nov. 2012, Available: http://www.ece.mcmaster.ca/~reilly/ece712/course_notes.htm

E. Rothwell, D.P. Nyquist, K.M. Chen, and B. Drachman, "Radar target discrimination using the extinction-pulse technique," *IEEE Trans. Antennas Propag*., vol. 33, no. 9, pp. 929–937, Sept. 1985.

T.G. Savelyev and A.G. Yarovoy "Fast imaging by 3-D deconvolution in short-range UWB radar for concealed weapon detection," *The 9th European Radar Conference (EuRAD 2012),* Oct. 2012.

A. Schatzberg and A.J. Devaney, "Super-resolution in diffraction tomography," *Inverse Problems*, vol. 8, pp. 149−164, 1992.

D.M. Sheen, D.L. McMakin, and T. E. Hall, "Near-field three-dimensional radar imaging techniques and applications," *Applied Optics*, vol. 49, no. 19, pp. E83–E93, Jun. 2010.

D.M. Sheen, D.L. McMakin, and T. E. Hall, "Three- dimensional millimeter-wave imaging for concealed weapon detection," *IEEE Trans. Microwave Theory Tech.*, vol. 49, no. 9, pp. 1581–1592, Sep. 2001.

D. M. Sheen, D. L. McMakin, and T. E. Hall, "Near field imaging at microwave and millimeter wave frequencies," *IEEE MTT-S Int. Microwave Symp.*, June 2007, pp. 1693–1696

SHF 100BP 30kHz-25GHz. https://www.shf.de/fileadmin/download/100bp.pdf

N. Shuley and D. Longstaff, "Role of polarization in automatic target recognition using resonance descriptions," *Electronic Lett.*, vol. 40, no. 4, Feb. 2004.

J.Y. Siddiqui, Y.M.M. Antar, A.P. Freundorfer, E.C. Smith, G.A. Morin, and T. Thayaparan, "Design of an ultrawideband antipodal tapered slot antenna using elliptical strip conductors," *IEEE Antennas Wireless Propag. Letters*, vol. 10, pp. 251–254, March 2011.

G. Sinclair, R. N. Anderton, and R. Appleby, "Outdoor passive millimetre wave security screening," *IEEE 35th Carnahan Conf. on Security Technologies*, 2001, pp. 172–179.

X. Song, B.W. Pogue, S. Jiang, M.M. Doyley, H. Dehghani, R.D. Tosteston, and K.D. Paulsen, "Automated region detection based on the contrast-to-noise ratio in near-infrared tomography, " *Applied Optics*, vol. 43, no. 5, pp. 1053–1062, 2004.

W.X. Tan, W. Hong, Y.P. Wang, and Y.R. Wu, "A novel spherical-wave three-dimensional imaging algorithm for microwave cylindrical scanning geometries," *Progress in Electromagnetics Research (PIER)*, vol. 111, pp. 43–70, 2011.

Tektronix AWG7102 10GS/s. http://www.tek.com/datasheet/awg7000-series

Tektronix DSA72004B 50GS/s. http://www.tek.com/oscilloscope/dpo70000-mso70000

G. Tricoles and N.H. Farhat, "Microwave holography: Applications and techniques," *Proc. IEEE*, vol. 65, no. 1, pp. 108–121, Jan. 1977.

S. Tu, J.J. McCombe, N.K.Nikolova, "Fast quantitative microwave imaging with resolvent kernel extracted from measurements," *Inverse Problems* (submitted Jun. 26, 2014).

S. Tu, J.J. McCombe, Y. Zhang, and N.K. Nikolova, "Sensitivity-based imaging of tissue using measurements of calibration objects," *European Microwave Conference (EuMC) 2014*, Oct. 2014, accepted.

A. Vasalos, I. Vasalos, H. Ryu, and S. Fotinea, "Fast concealed weapon detection via LTR analysis," *in IEEE Radar Conference*, Kansas City, MO, 2011.

A. Vasalos, I. Vasalos, H. Ryu, and S. Fotinea, "LTR analysis and signal processing for concealed explosive detection," *in German Microwave Conference*, Berlin, 2010.

A. Vasalos, I. Vasalos, H. Ryu, and S. Fotinea, "LTR analysis for fast concealed weapon detection," *in German Microwave Conference*, Darmstadt, 2011.

A. Vasalos, N. Uzunoglu, H. Ryu, and I. Vasalos, "Neural network target classification for concealed weapon radar detection", *in International Conference on Digital Signal Processing*, Fira, Greece, 2013.

H. Xu, "Planar raster-scanning system for near-field microwave imaging," M.A.Sc. Thesis, Dept. Elect. and Comput. Eng., McMaster Univ. Hamilton, Ontario, Canada, 2011.

L. Yujiri, M. Shoucri, and P. Moffa, "Passive millimeter-wave imaging," *IEEE Microwave Mag*., Sep. 2003, pp. 39–50.

R. Zoughi, *Microwave nondestructive testing and evaluation*. Kluwer Academic Publishers, The Netherlands, 2000.